

# RELATIVISTIC RUNAWAY ELECTRONS ABOVE THUNDERSTORMS

A DISSERTATION  
SUBMITTED TO THE DEPARTMENT OF PHYSICS  
AND THE COMMITTEE ON GRADUATE STUDIES  
OF STANFORD UNIVERSITY  
IN PARTIAL FULFILLMENT OF THE REQUIREMENTS  
FOR THE DEGREE OF  
DOCTOR OF PHILOSOPHY

Nikolai G. Lehtinen

March 2000

Copyright by Nikolai G. Lehtinen 2000

All Rights Reserved

I certify that I have read this dissertation and that in my opinion it is fully adequate, in scope and quality, as a dissertation for the degree of Doctor of Philosophy.

---

Umran S. Inan  
(Electrical Engineering Department)  
(Principal Adviser)

I certify that I have read this dissertation and that in my opinion it is fully adequate, in scope and quality, as a dissertation for the degree of Doctor of Philosophy.

---

Roger Romani

I certify that I have read this dissertation and that in my opinion it is fully adequate, in scope and quality, as a dissertation for the degree of Doctor of Philosophy.

---

Timothy F. Bell  
(Electrical Engineering Department)

Approved for the University Committee on Graduate Studies:

# Abstract

A three-dimensional Monte Carlo model of the uniform relativistic runaway electron breakdown in air in the presence of static electric and magnetic fields is developed and used to calculate electron distribution functions, avalanche rates and the direction and velocity of avalanche propagation. We also derive the conditions required for an electron with a given momentum to start an avalanche in the absence of a magnetic field. The results are compared to previously developed kinetic and analytical models and our own analytical estimates, leading to the conclusion that the avalanche rates used in many early models are overestimated by a factor of  $\sim 10$ .

The Monte Carlo simulation results are used in a fluid model of a runaway electron beam in the middle atmosphere accelerated by quasi-electrostatic fields following a positive lightning stroke. We consider the case of lightning discharges which drain positive charge from remote regions of a laterally extensive ( $>100$  km) thundercloud, using a cartesian (translationally symmetric in a horizontal direction) two-dimensional model. Unlike the cylindrically-symmetric model, this model can be applied to a case of a geomagnetic field with arbitrary direction. In particular, we consider the case of a thunderstorm located at  $\sim 45^\circ$  geomagnetic latitude. We also consider a cylindrically symmetric model with a vertical axis of symmetry, constrained to a vertical geomagnetic field.

In both models, the optical emission intensities produced by the runaway electrons or secondaries produced by them are found to be negligible compared to the emissions produced by thermal electrons heated in the conventional type of breakdown. The calculated  $\gamma$ -ray flux is of the same order as the terrestrial  $\gamma$ -ray flashes observed by the BATSE detector on the Compton Gamma Ray Observatory.

The energetic electrons leaving the atmosphere undergo intense interactions with the background magnetospheric plasma, leading to rapid nonlinear growth of Langmuir waves. Based on the energy and pitch angle distribution of the runaway electron beam determined as a function of the intensity of the parent lightning and the geomagnetic latitude, the pitch-angle scattering of the electrons due to beam-plasma interaction during their propagation along the geomagnetic field line is estimated. The beam electrons are strongly scattered by the waves in both pitch angle and energy, leading to the formation of an isotropic thermal distribution with a typical energy of  $\sim 1$  MeV within one interhemispheric traverse along the Earth's magnetic field lines. While those electrons within the loss cone precipitate out, most of the electrons execute bounce and drift motions, forming detectable trapped curtains of energetic electrons surrounding the Earth.

Electrons with pitch angles below the loss cone encounter the Earth's atmosphere at the conjugate point, are scattered and produce light, ionization and  $\gamma$ -ray emissions, much like a beam of precipitating auroral electrons. A Monte Carlo approach is used to model the interaction of the downcoming electrons with the conjugate atmosphere, including the backscattering of electrons as well as the production of optical emissions, enhanced secondary ionization and  $\gamma$ -ray emissions. Results indicate that these conjugate ionospheric effects are detectable and may be used to quantify the runaway electron mechanism.

# Acknowledgements

I would like to thank my principal adviser, Umran S. Inan for supervising this research. Although studying and doing research was hard work, it was also very pleasant because I felt Umran's respect and belief in me as a future scientist. I appreciate very much his openness to students. I am really amazed with his energy and enthusiasm and I really tried to learn to be like him. I would like to thank my co-adviser Timothy F. Bell for many ideas and suggestions he made with respect to the research constituting this dissertation, and for his devotion to teaching and doing research together with the students.

I would like to thank Professor Roger Romani and Professor Vahe Petrosian for being on the reading committee and scrupulous reading of this dissertation, and Professor David Leith for being the committee chairman.

I would like to express special gratitude to Dr. Victor Pasko for many extremely useful discussions and guiding suggestions related to this research. He also helped me many times not only as a scientist, but as a friend by showing me around in the U.S.A.

I would like to thank Michael Johnson for running the Long-Wave Propagation Capability computer program which contributed to the material of Chapter 6.

I thank Professor Martin Walt for help with the physics of energetic electrons and

emissions. I am grateful also to Prof. Helliwell and Prof. Carpenter for discussions and help on various topics. During the work in the VLF group I gained a lot of friends in persons of the present and former students: Prof. Steve Reising, Prof. Steve Cummer, Dr. David Lauben, Dr. Mehmet Demirkol, Chris Barrington-Leigh, Jacob Bortnik, Mike and Tim Chevalier, Elizabeth Gerken, Sean Lev-Tov, Maria Salvati, Georgios Veronis and Troy Wood.

My special thanks to the administrative staff, who greatly helped me in my work and studies at Stanford. I would like specially to thank Marcia Keating, who was a graduate student officer first at the Physics Department, where I was a student, and then at the Electrical Engineering Department, where I was doing my research. Her help really made my life as a student easier. I would like to thank the STAR Lab and VLF Group secretary ShaoLan Min for all her very hard work. I thank the current Physics graduate student officer Dawn Hyde and the Physics Administration staff.

Above all, I would like to thank my wife, Lidiya Polukhina, for coming with me to the U.S.A. and being by my side during all joys and troubles and my mother Nina N. Lehtinen who brought me up with love for science.

NIKOLAI G. LEHTINEN

*Stanford, California*

*March 7, 2000*

This research was supported in part by the National Aeronautics and Space Administration under grant NAGW4738, and in part by National Science Foundation under grant ATM-9522816 to Stanford University.

# Contents

<b>Abstract</b>	<b>iv</b>
<b>Acknowledgements</b>	<b>vi</b>
<b>1 Introduction</b>	<b>1</b>
1.1 Motivation . . . . .	1
1.1.1 Red Sprites . . . . .	2
1.1.2 Terrestrial $\gamma$ -Ray Flashes (TGFs) . . . . .	3
1.2 Other Evidence for Runaway Breakdown . . . . .	6
1.2.1 Conjugate Effects . . . . .	6
1.2.2 Laboratory Observations . . . . .	7
1.2.3 Other Observations in the Earth's Atmosphere . . . . .	7
1.3 Scientific Contributions . . . . .	8
<b>2 Monte Carlo Model</b>	<b>10</b>
2.1 Model Description . . . . .	12
2.1.1 Dynamic Friction Function (Stopping Power) . . . . .	13
2.1.2 Angular Diffusion . . . . .	15
2.1.3 Production of New Electrons via Ionization . . . . .	18



2.1.4	Dimensionless Variables . . . . .	20
2.2	Runaway Breakdown Results . . . . .	21
2.2.1	Avalanche Rates and Distribution Functions . . . . .	22
2.2.2	Analysis of Avalanche Rates . . . . .	25
2.2.3	Discussion . . . . .	32
2.2.4	Direction and Velocity of Avalanche . . . . .	36
<b>3</b>	<b>Optical and <math>\gamma</math>-Ray Emissions</b>	<b>37</b>
3.1	Optical Emissions . . . . .	38
3.2	Gamma-Ray Emissions . . . . .	45
3.2.1	Gamma Photon Production . . . . .	45
3.2.2	$\gamma$ -photon Propagation in the Atmosphere . . . . .	49
<b>4</b>	<b>Runaway Electrons in the Middle Atmosphere</b>	<b>54</b>
4.1	Cartesian Model . . . . .	55
4.2	Cylindrical Model . . . . .	66
4.3	Runaway Electron Beam Density . . . . .	70
<b>5</b>	<b>Interhemispheric Transport and Curtains</b>	<b>76</b>
5.1	Growth Rate of the Beam-Plasma Instability . . . . .	78
5.2	Nonlinear Growth . . . . .	81
5.3	Formation of Trapped Electron Curtains . . . . .	83
<b>6</b>	<b>Conjugate Hemisphere Effects</b>	<b>86</b>
6.1	Energetic Electron Precipitation . . . . .	87
6.2	Optical Emissions . . . . .	91
6.3	Secondary Ionization . . . . .	92

6.4	$\gamma$ -ray Emissions . . . . .	96
<b>7</b>	<b>Conclusions and Future Work</b>	<b>99</b>
7.1	Conclusions . . . . .	99
7.2	Suggestions for Future Work . . . . .	102
<b>A</b>	<b>Monte Carlo Model Details</b>	<b>104</b>
A.1	Dimensionless Units . . . . .	104
A.2	Diffusion: Choice of Angle . . . . .	105
A.3	Choice of $\Delta t$ . . . . .	107
A.4	Magnetic Mirror Effect . . . . .	108
A.5	Implementation of the Particle Set . . . . .	110
A.5.1	Null-Collision Method . . . . .	110
A.5.2	Stacked-Particle Method . . . . .	111
A.5.3	Optimized Null-Collision Method . . . . .	112
A.6	Photon Monte Carlo Calculations . . . . .	112
A.6.1	Calculation of the Time of the Next Collision . . . . .	112
A.6.2	Compton Scattering . . . . .	113
A.6.3	Photon Energy Deposition . . . . .	114
<b>B</b>	<b>Kinetic Equation</b>	<b>115</b>
	<b>Bibliography</b>	<b>118</b>

# List of Tables

2.1	Monte Carlo results for runaway avalanche rates . . . . .	23
2.2	Comparison of Monte Carlo results with analytical estimates . . . . .	33

# List of Figures

1.1	Mesospheric phenomena caused by lightning discharges . . . . .	2
1.2	Red sprites and elves . . . . .	4
1.3	Terrestrial gamma-ray flashes . . . . .	5
2.1	Dynamic friction function . . . . .	14
2.2	Temporal growth of the number of particles . . . . .	22
2.3	Runaway avalanche growth rates . . . . .	23
2.4	Electron 3D distributions . . . . .	24
2.5	Electron angular and energy distributions . . . . .	24
2.6	Runaway region boundary . . . . .	26
2.7	Comparison of different runaway avalanche models . . . . .	32
3.1	Bremsstrahlung cross-sections . . . . .	49
4.1	Schematics of the runaway mechanism . . . . .	55
4.2	Cartesian model results . . . . .	63
4.3	Calculated terrestrial gamma-ray flashes . . . . .	65
4.4	Cylindrical model results . . . . .	67
4.5	Optical emissions in the cylindrical model . . . . .	68
4.6	The minimum radius of a disk charge . . . . .	74

4.7	Electron flux entering the ionosphere . . . . .	74
5.1	Schematics of interhemispheric transport . . . . .	77
5.2	Momentum distribution of the escaping runaway electrons . . . . .	79
5.3	Runaway electron curtains . . . . .	84
6.1	Optical emissions in the conjugate region . . . . .	91
6.2	Conjugate ionization and conductivity enhancement . . . . .	93
6.3	Time evolution of ionization and conductivity . . . . .	94
6.4	Gamma rays emitted by precipitating electrons . . . . .	98

# Chapter 1

## Introduction

### 1.1 Motivation

This dissertation concerns the investigation of the mechanisms and resultant effects of runaway acceleration of relativistic electrons above thunderstorms. The motivation for this study was the recent discoveries of (i) lightning-associated luminous high altitude glows in the mesosphere, dubbed “Red Sprites” by *Sentman et al.* [1995], and (ii) terrestrial  $\gamma$ -ray flashes (TGF) observed on the Compton Gamma Ray Observatory satellite (CGRO) [*Fishman et al.*, 1994]. Although these two phenomena were scientifically first documented within the last decade, they were both predicted, and the significance of the role of accelerating relativistic electrons above a thundercloud in these phenomena was proposed as long ago as 1925. *Wilson* [1925] observed that “while electric force due to thundercloud falls off rapidly as [the altitude] increases, the electric force required to cause sparking (which for a given composition of air is proportional to its density) falls off still more rapidly”, and “there will be a height above which the electric force due to the cloud exceeds the sparking limit”, thereby

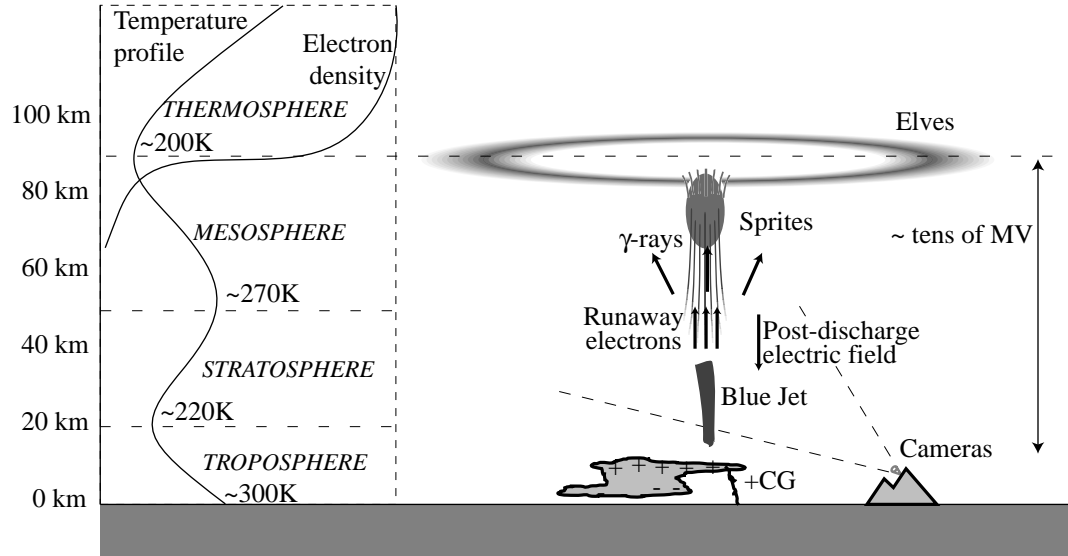


Figure 1.1: **Mesospheric phenomena caused by lightning discharges.**

causing what is now called Red Sprites, the giant discharges between the cloud and ionosphere. He also noted that above a certain energy, “the faster the  $\beta$ -particle moves the smaller is the rate at which it loses energy in collisions”, becoming a so-called *run-away electron*, and “a particle may thus acquire energy corresponding to the greater part of the whole potential difference between the poles of the thundercloud”. The resulting energetic  $\beta$ -particle radiation “may excite ...  $\gamma$  radiation” [Wilson, 1925]. The phenomena cause by lightning-mesosphere electrodynamic coupling are depicted in Figure 1.1.

### 1.1.1 Red Sprites

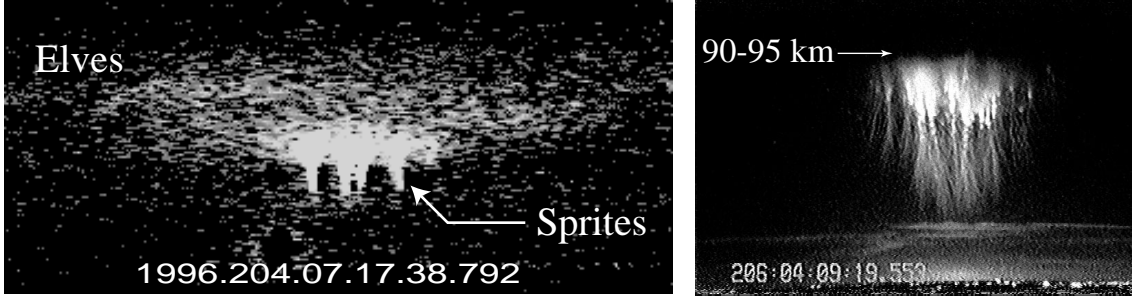
*Red sprites* [Sentman et al., 1995] (see Figure 1.2) are large-scale luminous glows occurring above thunderstorms at altitudes 50–90 km, exhibiting predominantly red color. They have a lateral extent of tens of kilometers, occur several milliseconds

after a large cloud-to-ground (CG) discharge and last up to several tens of milliseconds. They are believed to be caused by the heating of the ambient electrons by quasi-electrostatic post-discharge electric field [e.g., *Pasko et al.*, 1997]. Other luminous phenomena, which are not investigated in this dissertation are *blue jets* and *elves*. Blue jets [e.g., *Wescott et al.*, 1998a] occur at lower altitudes than sprites (Figure 1.1), exhibit blue color, and are also believed to be caused by the quasi-electrostatic field [*Pasko et al.*, 1996]. Elves are highly transient phenomena ( $\lesssim 1$  ms duration), believed to be caused by the electromagnetic pulse (EMP) from lightning [*Inan et al.*, 1997]. Several authors suggested that sprites and blue jets were produced solely by relativistic runaway electrons [e.g., *Roussel-Dupré et al.*, 1998]. In our work (Chapter 4 and [*Lehtinen et al.*, 1999]) we find that the optical emissions produced by the runaway electrons are much less intense than the luminosities observed in sprites. The fact that runaway electrons do not play an important role in red sprites is also suggested by (i) the observation of a sprite following a negative discharge [*Barrington-Leigh et al.*, 1999], which creates an upward-directed electric field unable to cause the runaway electron avalanche; (ii) the columniform sprites [*Wescott et al.*, 1998b], i.e., a type of narrow sprites at high ( $\sim 75$ – $90$  km) altitudes, are vertically oriented, while the runaway electron theory (see Chapter 4) predicts structures to be aligned with the magnetic field [*Lehtinen et al.*, 1999].

### 1.1.2 Terrestrial $\gamma$ -Ray Flashes (TGFs)

The  $\gamma$ -ray detectors of the Burst and Transient Source Experiment (BATSE) on the Compton Gamma Ray Observatory (CGRO) have detected transient  $\gamma$ -ray bursts originating below the satellite [*Fishman et al.*, 1994]. The CGRO satellite orbit is at  $\sim 500$  km altitude and  $28.5^\circ$  inclination. The BATSE instrument consists of 8 large



Figure 1.2: **Red sprites and elves.**

area detectors of  $2000 \text{ cm}^2$  each, which detect photons in four energy channels of 20 to 50 keV, 50 to 100 keV, 100 to 300 keV and  $>300 \text{ keV}$ . The angular resolution of the instrument for TGF is  $10^\circ$  to  $20^\circ$ , and the efficiency is  $\gtrsim 30\%$ . The detected terrestrial  $\gamma$ -ray flashes (TGF) have time duration of the order of 1 ms (Figure 1.3), consist of photons with energies of 20 keV to 2 MeV, and exhibit a hard spectrum consistent with bremsstrahlung [Nemiroff *et al.*, 1997]. Since these bursts are associated with thunderstorm centers and have been associated with individual lightning flashes [Inan *et al.*, 1996b], they may be caused by the relativistic electrons accelerated by thunderstorm-related electric fields. The fact that the  $\gamma$ -photons produced at low altitudes ( $<30 \text{ km}$ ) experience strong Compton scattering and attenuation due to the photoeffect before leaving the atmosphere suggests that the  $\gamma$ -ray production occurs above the cloud (Figure 1.1).

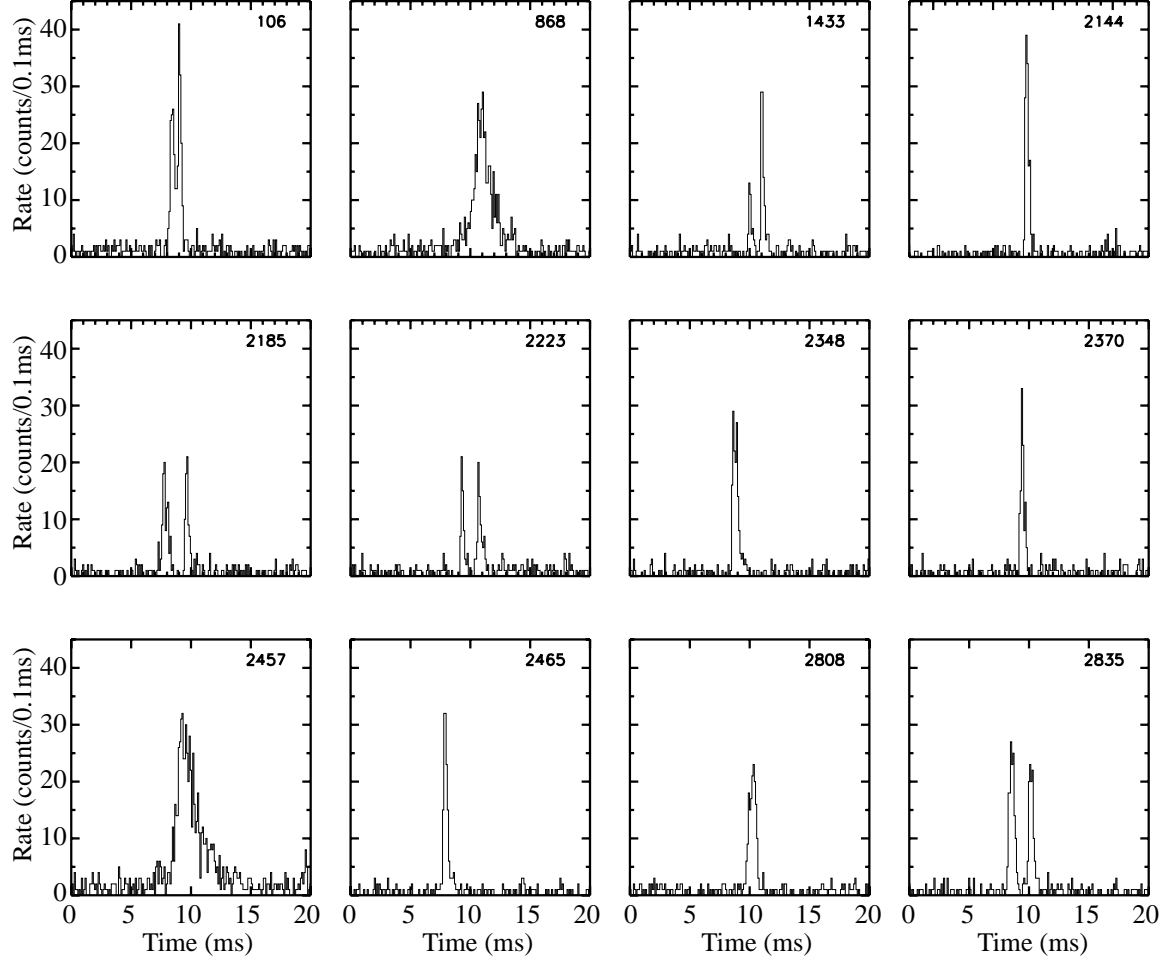


Figure 1.3: **Terrestrial gamma-ray flashes.** Examples reported by *Fishman et al.* [1994], showing BATSE photon counts in  $\gtrsim 20$  keV energy range, identified with trigger numbers given in the upper right corner.

## 1.2 Other Evidence for Runaway Breakdown

### 1.2.1 Conjugate Effects

The effects of runaway electrons which leave the atmosphere and precipitate at the geomagnetically conjugate location include light emissions,  $\gamma$ -ray emissions and ionization enhancements [Lehtinen *et al.*, 2000b] and are considered in Chapter 6. The experimentally documented terrestrial  $\gamma$ -ray flashes [Fishman *et al.*, 1994] may be caused by either the runaway electrons in the hemisphere of the lightning discharge or by the precipitating electrons in the conjugate hemisphere. Such precipitation would also produce relatively intense but brief optical emissions (see Chapter 6). An interesting example of optical emissions with properties similar to those expected are the so-called *fast atmospheric pulsations* (FAPs) [Ögelman, 1973]. The events observed by Ögelman [1973] have a typical timescale of 1 ms, have emissions within 4300 to 6300 Å spectral range, sometimes ( $\lesssim 5\%$  cases) have a horizontal extent of up to 175 km, but they are never so broad as to be caused by astrophysical phenomena. Some such events are associated with lightning [Winckler *et al.*, 1993] and can be interpreted as red sprites and elves (see above, also Figures 1.1 and 1.2). However, other similar events are not associated with lightning [Nemzek and Winckler, 1989], suggesting that they may be caused by precipitation of electrons of  $\sim 2$  MeV energy [LaBelle, 1988]. The source considered by LaBelle [1988] was the radiation-belt electrons scattered by lightning-induced waves in the magnetosphere and was criticized by Vampola [1988] on the basis of the fact that the energetic electron flux in the inner belt was too low to cause the observed optical emissions. This critique does not apply to the precipitating runaway electrons in the hemisphere conjugate to lightning since they are supplied by an external source. At the same time, Ögelman [1973] observed

a clear 10 kHz modulation in most events, which is not inherent in any aspect of the runaway electron beam processes discussed here. It thus remains to be seen whether FAPs are indeed conjugate signatures of the runaway breakdown.

### 1.2.2 Laboratory Observations

There have been many observations of runaway electron breakdown and associated x-ray emissions in tokamaks [e.g., *Kurzan et al.*, 1995; *Kuznetsov et al.*, 1999]. The conditions of a tokamak, however, have very little in common with the Earth's atmosphere (high temperature and ionization, different constituents). An experimental setup of conditions closest to those of the Earth's atmosphere were implemented by *Gurevich et al.* [1999a]. In the experimental setup, the breakdown occurred in magnetic field which ensured the cyclotron resonance of accelerating electrons with the applied electric field. Optical, x-ray and radio emissions were measured. The experiment clearly showed the presence of relativistic electrons. However, some results of the experiment cannot be completely understood in terms of the runaway electron avalanche theory at present time [*Gurevich et al.*, 1992]. For example, the relativistic breakdown was observed only when the electric field was  $\sim 20$  times higher than that predicted to be necessary.

### 1.2.3 Other Observations in the Earth's Atmosphere

Other observations of runaway electron acceleration in the Earth's atmosphere include x-rays inside thunderclouds and satellite observations of upward moving energetic electrons. X-rays inside a thundercloud were observed in a series of balloon experiments [*McCarthy and Parks*, 1985; 1992; *Eack et al.*, 1996a;b]. The most evident mechanism for the x-ray generation is the bremsstrahlung process which occurs

during an energetic runaway electron avalanche due to large electric fields inside the thundercloud. This process is not necessarily related to the lightning discharge processes [Eack *et al.*, 1996b; Gurevich *et al.*, 1997; Gurevich and Milikh, 1999b].

The observations of upward moving energetic nonrelativistic ( $\sim 1$  keV) electrons were made by the DE 2 satellite above a hurricane [Burke *et al.*, 1992]. As a possible hypothesis, Burke *et al.* [1992] suggest a mechanism of runaway electron acceleration by an electric pulse from a lightning flash which penetrates into ionosphere.

### 1.3 Scientific Contributions

Despite the ingenious prediction by Wilson [1925] of acceleration of runaway electrons above thundercloud, the possibility of their avalanche was overlooked. The first analytical study of the avalanche process involving  $\sim$ MeV electrons suggestion that accelerating electrons will create more energetic electrons was made by Gurevich *et al.* [1992]. After this analytical quantitative description of the avalanche process, other calculations were made [Roussel-Dupré *et al.*, 1994; Gurevich *et al.*, 1996; Symbalisty *et al.*, 1998; Babich *et al.*, 1998]. However, as it was pointed out [Babich *et al.*, 1998], the models by different authors gave conflicting results. This motivated us to create our own model [Lehtinen *et al.*, 1999]. A number of papers analyzed connection of high-energy (20 keV to 10 MeV) runaway electrons produced above thunderstorms and driven upward by the thundercloud electric field to the red sprites [Bell *et al.*, 1995; Lehtinen *et al.*, 1997; Roussel-Dupré *et al.*, 1998; Yuhimuk *et al.*, 1998; Yuhimuk *et al.*, 1999; Lehtinen *et al.*, 1999; Kutsyk and Babich, 1999] and terrestrial gamma ray flashes [Lehtinen *et al.*, 1996; Roussel-Dupré and Gurevich, 1996; Lehtinen *et al.*, 1999]. The results of Lehtinen *et al.* [1999] are presented in

this dissertation. The runaway electron escape from ionosphere, their propagation in magnetosphere and precipitation at the geomagnetically conjugate point was also studied [Lehtinen *et al.*, 2000a;b].

The specific scientific contributions of this work are:

1. The formulation of a 3D Monte Carlo model of runaway electron avalanche in applied electric and magnetic fields and the determination of avalanche rates and runaway electron distribution functions (Chapter 2).
2. The formulation of a fluid model of runaway breakdown in the middle atmosphere in 2D in Cartesian and cylindrical coordinates, taking into account the effects of the geomagnetic field (Chapter 4).
3. The calculation of optical and  $\gamma$ -ray emissions due to runaway electrons in the middle atmosphere (Chapter 3).
4. The assessment of the interaction of runaway electron beams with the cold magnetospheric plasma during its interhemispheric traverse and the formation of energetic electron curtains (Chapter 5).
5. The determination of the effects of the runaway electrons at the geomagnetically conjugate point, namely the optical and  $\gamma$ -ray emissions as well as the ionization enhancements (Chapter 6).

## Chapter 2

# Monte Carlo Model

The relativistic runaway electron breakdown process was previously studied not only in relation to non-ionized air but also in relation to high-energy plasmas, such as in tokamaks and astrophysical plasmas. Analytical studies considered uniform breakdown [Sizykh, 1993; Gurevich *et al.*, 1992], spatial propagation and diffusion of a runaway beam [Gurevich *et al.*, 1994], breakdown in the presence of a magnetic field [Gurevich *et al.*, 1996], and the runaway process in a high-energy plasma [Bulanov *et al.*, 1997]. The numerical solution of the kinetic equation describing the relativistic runaway breakdown in the absence of a magnetic field was obtained in air [Roussel-Dupré *et al.*, 1994; Symbalisty *et al.*, 1998] and in high-energy helium [Babich and Kutsyk, 1995]. One-dimensional (1-D) Monte Carlo models of thermal runaway with strong fields  $E/N > 3 \times 10^{-19}$  V-m<sup>2</sup> were applied to nitrogen [Kunhardt *et al.*, 1986] and neon [Shveigert, 1988].

In an earlier study of the relativistic runaway electron process [Lehtinen *et al.*, 1997], the avalanche rates were taken from a nonmagnetic kinetic model [Roussel-Dupré *et al.*, 1994], and the direction of avalanche propagation was calculated from

the equation of motion of an individual electron [Gurevich *et al.*, 1996].

It has since been shown [Symbalisty *et al.*, 1997] that the avalanche rates as reported by Roussel-Dupré *et al.* [1994] were not accurate, both because of numerical problems in the computations and owing to the fact that the effects of the magnetic field were neglected.

In this Chapter we use a Monte Carlo technique in order to model runaway avalanche in the presence of a magnetic field. This more general method also allows us to address existing discrepancies between the results of different models of this phenomenon. Avalanche rates and the direction and velocity of avalanche propagation are accurately determined from our Monte Carlo model and used in Chapter 4 in two-dimensional Cartesian and cylindrically-symmetric models of the runaway process in the middle atmosphere. The Monte Carlo model considered here allows an arbitrary direction of the geomagnetic field.

We use the following notation and variables throughout this work:

**E, B** external electric and magnetic fields, assumed constant and uniform in the Monte Carlo calculations;

**p,  $\mathcal{E}$ , v** electron momentum, kinetic energy and velocity, respectively;

$\gamma = (1 - v^2/c^2)^{-1/2} = 1 + \frac{\mathcal{E}}{mc^2}$  electron relativistic factor;

$N_m$  altitude-dependent molecular density of air;

$Z_m \simeq 14.5$  average molecular nuclear charge for air;

$q_e \simeq -1.602 \times 10^{-19}$  C electron charge;

$m \simeq 9.109 \times 10^{-31}$  kg electron mass;

$c \simeq 2.998 \times 10^8$  m-s<sup>-1</sup> speed of light;

$r_0 = q_e^2/(4\pi\epsilon_0 mc^2) \simeq 2.818 \times 10^{-15}$  m classical electron radius.



## 2.1 Model Description

The Monte Carlo model of runaway breakdown makes use of a set of test electrons, for which phase space coordinate information is stored. The motion of energetic electrons is described by the Langevin equation, which includes the electric and magnetic forces and a stochastic force  $\mathbf{\Gamma}(t)$ , which describes the elastic and inelastic collisional scattering of electrons:

$$\frac{d\mathbf{p}}{dt} = q_e \mathbf{E} + \frac{q_e}{m\gamma} \mathbf{p} \times \mathbf{B} + \mathbf{\Gamma}(t). \quad (2.1)$$

The model is based on solving equation (2.1) numerically for each electron in the set, with a time step  $\Delta t$ . The collision term  $\mathbf{\Gamma}$  is divided into two parts, one involving the processes of electron energy loss and described in terms of a *dynamic friction function* and the other involving *angular diffusion* (direction of momentum change) determined on a statistical basis. The latter includes the finite probability that some of the collisions lead to the generation of new energetic electrons by ionization, which must be added to the existing set of test electrons.

Typically, there are many more electrons at lower energies than at higher energies due to the  $(\mathcal{E}')^{-2}$  dependence of the ionization probability for production of a secondary electron of energy  $\mathcal{E}'$ , as is shown later. For simplicity, we only consider electrons with  $\mathcal{E} > \mathcal{E}_{\min}$  and choose  $\mathcal{E}_{\min} = 2$  keV. Any electrons for which the kinetic energy decreases below  $\mathcal{E}_{\min}$  are dropped from the set. For an ionizing collision leading to the production of a secondary electron with energy  $\mathcal{E}' > \mathcal{E}_{\min}$ , momentum vectors of both electrons after the ionizing collision are calculated on the basis of the ionization cross section. For  $\mathcal{E}' < \mathcal{E}_{\min}$ , the processes of energy loss and velocity direction change for the primary electron are described in terms of the dynamic friction

function and angular diffusion, respectively.

### 2.1.1 Dynamic Friction Function (Stopping Power)

The energy losses for energetic electron motion in a collisional gas are due to excitation and ionization processes and can be described in terms of a dynamic friction force  $F_D(\mathcal{E})$  [Bethe and Ashkin, 1953, p. 254], effectively acting in the direction opposite to the electron motion:

$$F_D(\mathcal{E}) = N_m Z_m \kappa \left\{ \log \left[ \frac{mv^2 \mathcal{E}}{\mathcal{E}_{\text{ion}}^2 (1 - v^2/c^2)} \right] - \left( 1 + \frac{2}{\gamma} - \frac{1}{\gamma^2} \right) \log 2 + \frac{(\gamma - 1)^2}{8\gamma^2} + \frac{1}{\gamma^2} \right\}, \quad (2.2)$$

where  $\log[\cdot]$  indicates the natural logarithm throughout this dissertation and

$$\kappa = 2\pi r_0^2 m c^2 (c/v)^2 \quad (2.3)$$

and  $\mathcal{E}_{\text{ion}}$  is the average ionization energy, being  $\mathcal{E}_{\text{ion}} \simeq 80.5$  eV for air [Roussel-Dupré *et al.*, 1994]. This force has a minimum (Figure 2.1) at electron kinetic energy  $\mathcal{E} \simeq 2.39mc^2 \simeq 1.22$  MeV, which is equal to the electric force due to the *runaway threshold field*  $E_t$ , determined by

$$\frac{E_t}{N_m} \simeq 21.7 \times 2\pi Z_m r_0^2 m c^2 e^{-1} \simeq 8.05 \times 10^{-21} \text{ V}\cdot\text{m}^2 = 8.05 \text{ Td}, \quad (2.4)$$

where Td is a “townsend”, a convenient unit of  $E/N$ .

Because the ionization with creation of electrons with energy  $\mathcal{E}' > \mathcal{E}_{\text{min}}$  is included explicitly in our model, we must exclude the energy losses associated with it from the dynamic friction:

$$F_D^{\text{excl}}(\mathcal{E}) = F_D(\mathcal{E}) - F_D^{\text{ion}}(\mathcal{E}), \quad (2.5)$$

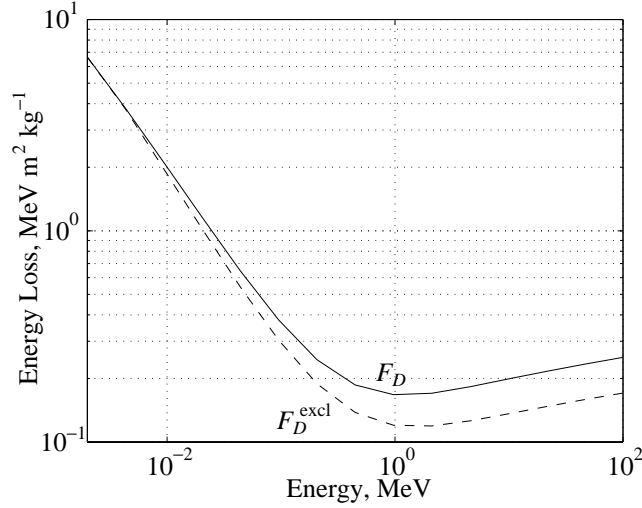


Figure 2.1: **Dynamic friction function.** Solid line represents the full dynamic friction function  $F_D$  given in equation (2.2), while the dashed line is the dynamic friction  $F_D^{\text{excl}}$  with ionization excluded given in equation (2.8).

where  $F_D^{\text{excl}}(\mathcal{E})$  is now the dynamic friction term that is used as the first part of the stochastic force  $\mathbf{\Gamma}(t)$  in (2.1). If we neglect the ionization energy  $\mathcal{E}_{\text{ion}} \ll \mathcal{E}_{\text{min}}$  the ionization loss is given by

$$F_D^{\text{ion}}(\mathcal{E}) = N_m Z_m \int_{\mathcal{E}_{\text{min}}}^{\mathcal{E}/2} \mathcal{E}' \frac{d\sigma_{\text{ion}}}{d\mathcal{E}'} d\mathcal{E}', \quad (2.6)$$

where the differential ionization cross section  $d\sigma_{\text{ion}}/d\mathcal{E}'$  is given by the Møller formula [Bethe and Ashkin, 1953, p. 277; also expression (2.14) below] and is a function of both  $\mathcal{E}$  and  $\mathcal{E}'$ . Electrons emerging from a collision are indistinguishable, and we label the one with the lower energy as the secondary electron. Therefore, the maximum energy that can be lost in a collision is  $\mathcal{E}/2$ .

Substituting the Møller cross section we find

$$F_D^{\text{ion}}(\mathcal{E}) = N_m Z_m \kappa \left\{ \log \left[ \frac{\mathcal{E}}{2\mathcal{E}_{\min}} \right] + \frac{(\gamma - 1)^2}{8\gamma^2} - \frac{\mathcal{E}_{\min}^2}{2(mc^2 + \mathcal{E})^2} - \left( 1 + \frac{2}{\gamma} - \frac{1}{\gamma^2} \right) \log \left[ \frac{2(\mathcal{E} - \mathcal{E}_{\min})}{\mathcal{E}} \right] + 1 - \frac{\mathcal{E}_{\min}}{\mathcal{E} - \mathcal{E}_{\min}} \right\}, \quad (2.7)$$

$$F_D^{\text{excl}}(\mathcal{E}) = N_m Z_m \kappa \left\{ \log \left[ \frac{2\mathcal{E}_{\min} m v^2}{\mathcal{E}_{\text{ion}}^2 (1 - v^2/c^2)} \right] - \left( 1 + \frac{2}{\gamma} - \frac{1}{\gamma^2} \right) \log \left[ \frac{\mathcal{E}}{\mathcal{E} - \mathcal{E}_{\min}} \right] + \frac{\mathcal{E}_{\min}}{\mathcal{E} - \mathcal{E}_{\min}} - \frac{v^2}{c^2} + \frac{\mathcal{E}_{\min}^2}{2(mc^2 + \mathcal{E})^2} \right\} \quad (2.8)$$

Note that equation (2.6) is meaningful only for  $\mathcal{E} \geq 2\mathcal{E}_{\min}$ , and therefore for  $\mathcal{E}_{\min} < \mathcal{E} < 2\mathcal{E}_{\min}$  we still use expression (2.2) instead of equation (2.8). Both  $F_D(\mathcal{E})$  and  $F_D^{\text{excl}}(\mathcal{E})$  are plotted in Figure 2.1 as functions of  $\mathcal{E}$ .

For the electron energies of interest in the mesosphere ( $< 100$  MeV, as limited by the total electric potential difference between the thundercloud and the ionosphere), the radiative losses due to bremsstrahlung are negligible [Jackson, 1975, p. 718] and are not accounted for in our model.

### 2.1.2 Angular Diffusion

The angular scattering of electrons is mostly due to their elastic collisions with nuclei. The contribution of this process is greater by a factor of atomic charge  $Z_a = Z_m/2$  than the contribution of collisions with electrons.

Although the elastic collisions are frequent, the average angle of scattering is small, and we can choose our time step  $\Delta t$  much greater than the time between collisions. We incorporate small-angle collisions into the Monte Carlo model as random changes of the direction of  $\mathbf{p}$  by an angle  $\Delta\Theta$ .

To find  $\Delta\Theta$  for given  $\Delta t$ , we calculate a random variable  $\mu = \cos(\Delta\Theta)$ , which has a probability distribution  $f(\mu, t = \Delta t)$ . This distribution is normalized to unity, i.e.,

$$\int_{-1}^1 f(\mu, t) d\mu = 1$$

and satisfies an initial condition such that  $f \neq 0$  only at  $\Delta\Theta = 0$  (the direction of an electron is fixed):

$$f(\mu, t = 0) = \delta(\mu - 1_-)$$

where by  $1_-$  we mean that the delta function is fully included when integrated with upper limit 1. For energetic electrons undergoing elastic collisions with nuclei, the probability distribution function  $f(\mu, t)$  satisfies the diffusion equation, derived in Appendix B [*Roussel-Dupré et al.*, 1994]:

$$\frac{\partial f}{\partial t} = D \frac{\partial}{\partial \mu} \left[ (1 - \mu^2) \frac{\partial f}{\partial \mu} \right]$$

where the angular diffusion coefficient  $D$  is related to the time rate of change of the mean (ensemble average) square angle, an explicit expression for which is given in (2.12)

$$D(p) = \frac{1}{4} \frac{d\langle \Theta^2 \rangle}{dt}$$

This relation follows from the general theory of the Langevin and Fokker-Planck equations [e.g., *Risken*, 1989, pp. 35–36]. The solution to the diffusion equation is

$$f(\mu, \Delta t) = \sum_{n=0}^{\infty} \left( n + \frac{1}{2} \right) P_n(\mu) e^{-Dn(n+1)\Delta t} \quad (2.9)$$

where  $P_n$  are the Legendre polynomials. For  $D\Delta t \gtrsim 1$ , in calculations we take into account only the terms  $n=0$  and 1 in equation (2.9). For small  $D\Delta t$  we can approximate equation (2.9) as (see Section A.2)

$$f(\mu, \Delta t) \simeq \frac{1}{2D\Delta t} \exp\left(-\frac{1-\mu}{2D\Delta t}\right) \quad (2.10)$$

For extremely small scattering angles  $\Delta\Theta$ , equation (2.10) is not well suited for computation as explained in Appendix A. In such cases we take a fixed  $\Delta\Theta$  [Riskin, 1989, p. 60]:

$$\Delta\Theta \equiv \sqrt{\langle\Theta^2\rangle} = \sqrt{\frac{d\langle\Theta^2\rangle}{dt}\Delta t}. \quad (2.11)$$

Equation (2.11) is valid for multiple scattering for distributions of the random single-scattering angle with finite variance, as is the case here because the singularity of the Rutherford formula for the scattering cross section at small angles [Bethe and Ashkin, 1953, p. 273] is absent due to screening (see below).

The time rate change of the mean square angle for electrons, scattered by neutral atoms is [Jackson, 1975, p. 649]:

$$\frac{d\langle\Theta^2\rangle}{dt} = v \frac{d\langle\Theta^2\rangle}{ds} = 2\pi N_a v \left(\frac{2Z_a r_0 c^2}{\gamma v^2}\right)^2 \log\left[\frac{\theta_{\max}}{\theta_{\min}}\right], \quad (2.12)$$

where  $N_a = 2N_m$  is the number density of atoms. The angle  $\theta_{\min}$  is the minimum angle of scattering, below which the scattered angular distribution falls substantially below the Rutherford formulas for a Coulomb potential. This minimum angle is determined by Fermi-Thomas screening of the nucleus by bound electrons. The angle  $\theta_{\max}$  for electrons is  $\sim 1$  radian for electrons in air with energy less than  $\sim 50$  MeV, so that the size of the nucleus is not important [Jackson, 1975, p. 646]. The minimum

angle is  $\theta_{\min} = Z_a^{1/3}(mc/p)/\xi$ , where  $\xi = 192$  [Jackson, 1975, p. 645], or  $\xi = 65.3$  [Mott and Massey, 1965, p. 469]. In our calculations we choose [C. L. Longmire and H. J. Longley, unpublished report, 1973]  $\theta_{\max} = 2$  radians and  $\theta_{\min} = Z_a^{1/3}(mc/p)/65.3$  from [Mott and Massey, 1965]. Upon substitution, we find

$$\frac{d\langle\Theta^2\rangle}{dt} = \frac{4\pi N_m Z_m^2 r_0^2 c^4}{v^3 \gamma^2} \log \left( \frac{164.7}{Z_m^{1/3}} \frac{p}{mc} \right). \quad (2.13)$$

### 2.1.3 Production of New Electrons via Ionization

Production of secondary electrons in ionizing collisions is described by the Møller formula [Bethe and Ashkin, 1953, p. 277] for relativistic scattering of two free electrons, one of them being initially at rest. In this way, we neglect the ionization energy  $I \ll \mathcal{E}_{\min}$ . The differential ionization cross section per unit secondary electron energy interval is [Bethe and Ashkin, 1953, p. 277]

$$\frac{d\sigma_{\text{ion}}}{d\mathcal{E}'} = \kappa \left\{ \frac{1}{\mathcal{E}'^2} - \frac{1}{(\mathcal{E} - \mathcal{E}')\mathcal{E}'} \frac{(2\mathcal{E} + mc^2)mc^2}{(\mathcal{E} + mc^2)^2} + \frac{1}{(\mathcal{E} - \mathcal{E}')^2} + \frac{1}{(\mathcal{E} + mc^2)^2} \right\} \quad (2.14)$$

where  $\kappa$  is defined in equation (2.3),  $\mathcal{E}$  is the initial kinetic energy, and  $\mathcal{E}'$  is the kinetic energy of the secondary electron after collision.

The total ionization cross section for all secondary electron energies  $\mathcal{E}' > \mathcal{E}_{\min}$  and up to the maximum energy of  $\mathcal{E}/2$  is

$$\begin{aligned} \sigma_{\text{tot}}(\mathcal{E}) &= \int_{\mathcal{E}_{\min}}^{\mathcal{E}/2} \frac{d\sigma_{\text{ion}}}{d\mathcal{E}'} d\mathcal{E}' \\ &= \kappa \left\{ \frac{1}{\mathcal{E}_{\min}} - \frac{1}{\mathcal{E} - \mathcal{E}_{\min}} + \frac{\mathcal{E} - 2\mathcal{E}_{\min}}{2(mc^2 + \mathcal{E})^2} + \frac{mc^2(mc^2 + 2\mathcal{E})}{\mathcal{E}(mc^2 + \mathcal{E})^2} \log \left[ \frac{\mathcal{E}_{\min}}{\mathcal{E} - \mathcal{E}_{\min}} \right] \right\} \end{aligned} \quad (2.15)$$

The probability of ionization during time step  $\Delta t$  by an electron is then

$$P = N_m Z_m v \sigma_{\text{tot}}(\mathcal{E}) \Delta t \quad (2.16)$$

The random secondary electron energy  $\mathcal{E}_{\text{sec}}$  in the Monte Carlo code is found on the basis of the random variable

$$X(\mathcal{E}_{\text{sec}}) = \frac{1}{\sigma_{\text{tot}}(\mathcal{E})} \int_{\mathcal{E}_{\text{min}}}^{\mathcal{E}_{\text{sec}}} \frac{\partial \sigma_{\text{ion}}}{\partial \mathcal{E}'} d\mathcal{E}' \quad (2.17)$$

uniformly distributed in the interval  $[0, 1]$ . Inversion of (2.17) to find  $\mathcal{E}_{\text{sec}}$  is approximated by using only the first term in (2.14):

$$\begin{aligned} \frac{\partial \sigma_{\text{ion}}}{\partial \mathcal{E}'}(\mathcal{E}, \mathcal{E}') &\simeq \frac{\kappa}{\mathcal{E}'^2} \\ \int_{\mathcal{E}_{\text{min}}}^{\mathcal{E}_{\text{sec}}} \frac{\partial \sigma_{\text{ion}}}{\partial \mathcal{E}'}(\mathcal{E}, \mathcal{E}') d\mathcal{E}' &\simeq \kappa \left( \frac{1}{\mathcal{E}_{\text{min}}} - \frac{1}{\mathcal{E}_{\text{sec}}} \right) \\ \sigma_{\text{tot}}(\mathcal{E}) &\simeq \int_{\mathcal{E}_{\text{min}}}^{\mathcal{E}/2} \frac{\kappa}{\mathcal{E}'^2} d\mathcal{E}' = \kappa \left( \frac{1}{\mathcal{E}_{\text{min}}} - \frac{2}{\mathcal{E}} \right), \end{aligned}$$

so that

$$\mathcal{E}_{\text{sec}} \simeq \frac{\mathcal{E} \mathcal{E}_{\text{min}}}{\mathcal{E} - X(\mathcal{E} - 2\mathcal{E}_{\text{min}})}. \quad (2.18)$$

Numerical inversion of  $X(\mathcal{E}_{\text{sec}})$  using the exact expression (2.17) can be realized using Newton's method, but does not give significantly increased precision compared to (2.18). In fact, the error in  $\mathcal{E}_{\text{sec}}$  as determined with (2.18) does not exceed  $\sim 5\%$ .

The components of the electron momenta after the collision are determined from the conservation of energy and momentum. The angles are most efficiently found from scalar products of energy-momentum four vectors [*Jackson*, 1975, p. 531] of electrons before and after a collision. For example, if  $\mathbf{p}_0$ ,  $\mathbf{p}_{\text{rest}}$  and  $\mathbf{p}_1$ ,  $\mathbf{p}_2$  are respectively the



energy-momentum four vectors of the moving and resting electrons before and after a collision, then  $\mathbf{p}_0 = \{mc\gamma_0, \mathbf{p}_0\}$ ,  $\mathbf{p}_{\text{rest}} = \{mc, \mathbf{0}\}$ ,  $\mathbf{p}_1 = \{mc\gamma_1, \mathbf{p}_1\}$ ,  $\mathbf{p}_2 = \{mc\gamma_2, \mathbf{p}_2\}$ , and  $\mathbf{p}_{\text{rest}} + \mathbf{p}_0 = \mathbf{p}_1 + \mathbf{p}_2$ . Using the fact that  $\mathbf{p}^2 = \mathbf{p} \cdot \mathbf{p} \equiv m^2c^2\gamma^2 - |\mathbf{p}|^2 = m^2c^2$  for any electron state, from  $(\mathbf{p}_0 - \mathbf{p}_1)^2 = (\mathbf{p}_2 - \mathbf{p}_{\text{rest}})^2$  we promptly find  $\mathbf{p}_0 \cdot \mathbf{p}_1 = m^2c^2(\gamma_0\gamma_1 - \gamma_2)$  and

$$\cos(\widehat{\mathbf{p}_0, \mathbf{p}_1}) = \sqrt{\frac{\mathcal{E}_1(\mathcal{E}_0 + 2mc^2)}{\mathcal{E}_0(\mathcal{E}_1 + 2mc^2)}}, \quad (2.19a)$$

$$\sin(\widehat{\mathbf{p}_0, \mathbf{p}_1}) = \sqrt{\frac{mc^2(\mathcal{E}_0 - \mathcal{E}_1)}{\mathcal{E}_0(\mathcal{E}_1 + 2mc^2)}}, \quad (2.19b)$$

where  $\widehat{\mathbf{p}_0, \mathbf{p}_1}$  refers to the angle between the momentum vectors  $\mathbf{p}_0$  and  $\mathbf{p}_1$ ,  $\mathcal{E}_{0,1} = mc^2(\gamma_{0,1} - 1)$  are the kinetic energies of corresponding electrons and where we have used  $|\mathbf{p}| = mc\sqrt{\gamma^2 - 1}$  for each state and  $\gamma_2 = \gamma_0 + 1 - \gamma_1$ . The direction of the momentum of the other electron is found by interchanging the indices  $1 \rightarrow 2$ . The angles for the electron directions were also given in previous works on the runaway breakdown process [e.g., *Roussel-Dupré et al.*, 1994].

#### 2.1.4 Dimensionless Variables

To simplify numerical coefficients in the equations describing collisional processes in the program, we use dimensionless values of electron momentum, energy and velocity, and time:

$$\bar{\mathcal{E}} = \frac{\mathcal{E}}{mc^2}; \quad \bar{\mathbf{p}} = \frac{\mathbf{p}}{mc}; \quad \bar{\mathbf{v}} \equiv \boldsymbol{\beta} = \frac{\mathbf{v}}{c}; \quad \bar{t} = \frac{t}{\tau} \quad (2.20)$$

where

$$\tau = (2\pi N_m Z_m r_0^2 c)^{-1} \quad (2.21)$$

is the characteristic time scale of the process. With this choice,  $N_m Z_m \kappa / (mc\tau) = \beta^{-2}$  and the equation of motion (2.1) does not depend on  $N_m$  and therefore on the altitude at which the process occurs. The sea level value of  $N_m \simeq 2.688 \times 10^{25} \text{ m}^{-3}$  corresponds to  $\tau \simeq 172 \text{ ns}$ .

We calculate avalanche rates and average velocities as a function of electric and magnetic fields and the angle between them and use the following dimensionless substitutes for these parameters:

$$\delta_0 = \frac{|\mathbf{E}|}{E_t}; \quad \eta_0 = \frac{c|\mathbf{B}|}{E_t}; \quad \mu_0 = \cos(\widehat{\mathbf{E}, \mathbf{B}}) \quad (2.22)$$

where  $\widehat{\mathbf{E}, \mathbf{B}}$  denotes the angle between the two vectors.

## 2.2 Runaway Breakdown Results

If a strong enough uniform electric field  $\mathbf{E}$  (such that  $E = |\mathbf{E}| \gtrsim E_t$ ) is applied to a uniform volume of air with a certain number of seed energetic electrons present, then the number of energetic runaway electrons grows due to impact ionization via the collisions between energetic electrons and neutrals, and a *runaway breakdown*, or *avalanche* occurs. The temporal growth rate of the number  $N_R$  of energetic electrons depends nonlinearly on both magnitude and direction of  $\mathbf{E}$  with respect to the magnetic field  $\mathbf{B}$ . In this Section, we use the Monte Carlo method to determine the temporal growth of the runaway electron number density, as well as the electron distribution functions.

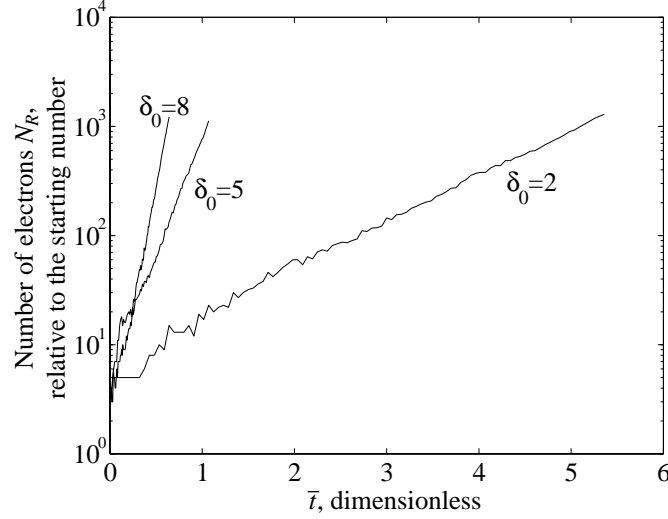


Figure 2.2: **Temporal growth of the number of particles.** Shown are the results of Monte Carlo calculations for different values of  $\delta_0$  for the case  $\mathbf{B} = 0$ .

### 2.2.1 Avalanche Rates and Distribution Functions

We choose  $\mathbf{E} = E_x \hat{\mathbf{x}} + E_z \hat{\mathbf{z}}$  and  $\mathbf{B} = B_z \hat{\mathbf{z}}$  and store momentum components  $p_x$ ,  $p_y$ ,  $p_z$  and coordinates  $x$ ,  $y$ ,  $z$  for each electron in the set. The calculation is started by introducing a few electrons of energy 1 MeV in the direction opposite to  $\mathbf{E}$ . In the absence of a magnetic field the number of electrons grows as shown in Figure 2.2 for three different values of normalized electric field  $\delta_0$ . One can see from Figure 2.2 that the growth is exponential. Assuming the time dependence of the energetic electron number  $N_R(t)$  to be proportional to  $e^{\gamma_R t}$ , we can find the avalanche rate  $\gamma_R$ . Figure 2.3 shows the calculated avalanche rates expressed in a dimensionless form for different  $\delta_0$  as a function of normalized magnetic field  $\eta_0$  for  $\mathbf{B} \perp \mathbf{E}$ . The data for this plot are given also in Table 2.1. The statistical error in  $\gamma_R$  is calculated using the fact that the error in the number of particles is  $\sqrt{N_R}$ .

Calculated rate values  $\gamma_R$  at  $\eta_0 = 0$  are  $\sim 10$  times less than those of *Roussel-Dupré*

$\eta_0 \backslash \delta_0$	2	5	8	15	30
0	$0.955 \pm 0.053$	$4.94 \pm 0.27$	$10.3 \pm 0.6$	$22.5 \pm 1.3$	$60.4 \pm 3.6$
1	$0.867 \pm 0.051$	$5.08 \pm 0.29$	$9.68 \pm 0.57$	$22.9 \pm 1.3$	$56.9 \pm 3.4$
2	...	$4.93 \pm 0.29$	$10.4 \pm 0.6$	$23.2 \pm 1.4$	$59.8 \pm 3.5$
5	...	$4.05 \pm 0.24$	$9.68 \pm 0.55$	$23.2 \pm 1.4$	$59.4 \pm 3.7$
8	...	$0.151 \pm 0.009$	$8.12 \pm 0.47$	$22.7 \pm 1.3$	$57.0 \pm 3.3$
15	...	...	$0.741 \pm 0.041$	$20.9 \pm 1.2$	$57.8 \pm 3.6$
30	...	...	...	$9.87 \pm 0.58$	$56.9 \pm 3.4$

Table 2.1: **Monte Carlo results for runaway avalanche rates.** Dimensionless avalanche rate  $\bar{\gamma}_R = \gamma_R \tau$  for different parameters  $\delta_0 = E/E_t$  and  $\eta_0 = cB/E_t$  for  $\mathbf{E} \perp \mathbf{B}$ . Three dots correspond to a situation without an avalanche. All results were derived for 1500 test particles.

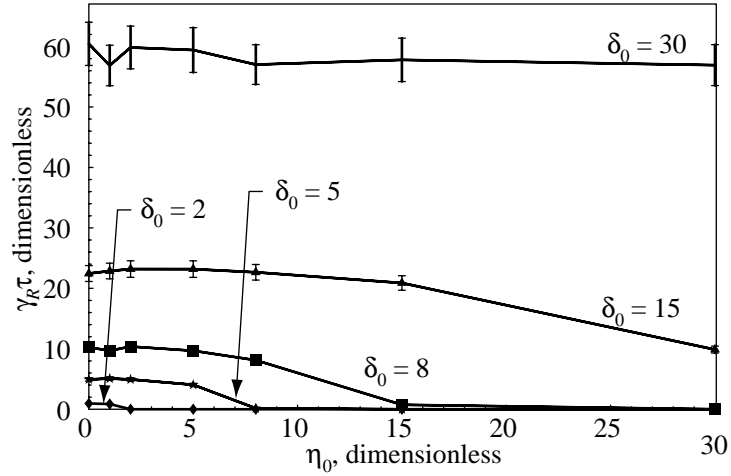


Figure 2.3: **Runaway avalanche growth rates.** Runaway avalanche growth rate  $\gamma_R$  multiplied by the characteristic time  $\tau$  defined in equation (2.21) constitutes a dimensionless indicator of the growth rate. Plotted are the magnetic field dependence of the dimensionless avalanche rate for different values of electric field for  $\mathbf{E} \perp \mathbf{B}$ .

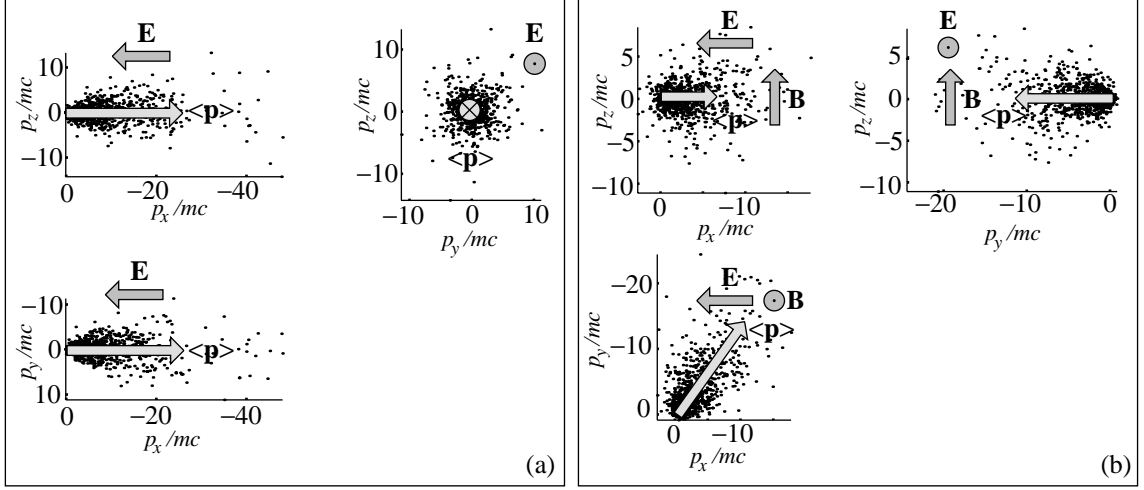


Figure 2.4: **Electron 3D distributions.** Electrons in momentum space for orthogonal  $\mathbf{E}$  and  $\mathbf{B}$ , with  $\delta_0 = 5$ : (a)  $\eta_0 = 0$  and (b)  $\eta_0 = \delta_0$ . The average momenta  $\langle \mathbf{p} \rangle$  are also shown. No avalanche occurs for  $\eta_0 = 2\delta_0$ .

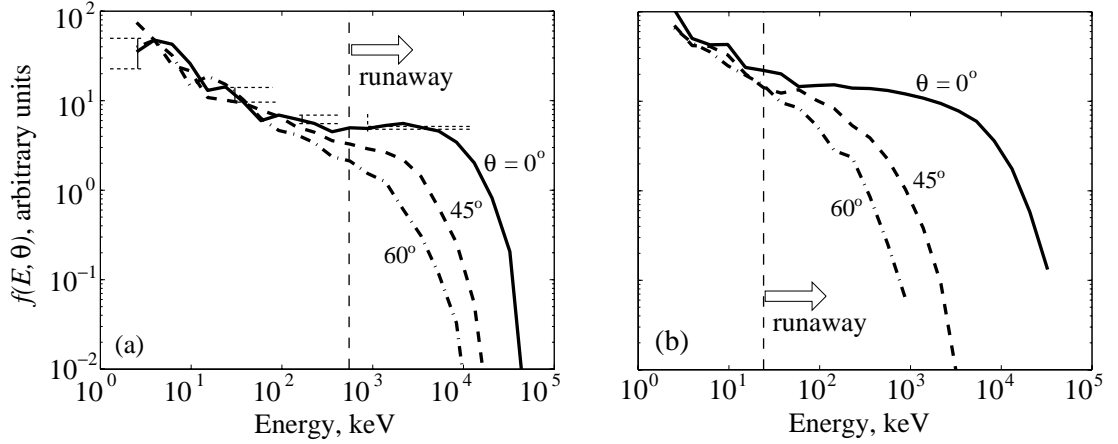


Figure 2.5: **Electron angular and energy distributions.** Shown for two different electric field values in the absence of a magnetic field: (a)  $\delta_0 = 2$ , (b)  $\delta_0 = 15$ . Also shown is the runaway region of electron energies, calculation of which is discussed later in the text (Section 2.2.2). The horizontal dashed lines show an estimate of the statistical error for  $\theta = 0$ .

*et al.* [1994], which were used in our previous calculations [Lehtinen *et al.*, 1997], and which were apparently inaccurate [Symbalisty *et al.*, 1997] as discussed in Section 1.1. With the lower values of  $\gamma_R$ , larger electric fields or longer avalanche distances are required in order to produce a significant number of runaway electrons in the middle atmosphere (see Chapter 4). Figure 2.4 shows the distribution of particles in the momentum space for different values of  $\eta_0$ , for  $\mathbf{B} \perp \mathbf{E}$ . Results indicate a significant  $\mathbf{E} \times \mathbf{B}$  drift in addition to the motion in the plane of  $\mathbf{E}$  and  $\mathbf{B}$ . Figure 2.5 shows the *self-similar* electron momentum distributions which grow uniformly with time at the same rate at all momenta. They were obtained in the absence of a magnetic field for two different values of  $\delta_0$ . The electron momentum distributions were calculated using a total of  $2 \times 10^4$  Monte Carlo particles, by counting the number of particles in each bin of  $\Delta(\log \mathcal{E}) \simeq 0.22$ ,  $\Delta(\cos \theta) = 0.2$ . The statistical error estimate for the  $\theta = 0$  curve is shown with horizontal dashed lines. In form, the distribution functions resemble those obtained by kinetic calculations [Roussel-Dupré *et al.*, 1994].

### 2.2.2 Analysis of Avalanche Rates

We now consider the case without a magnetic field, i.e.,  $\mathbf{B} = 0$ . The motion of electrons is then axially symmetric with the axis of symmetry being along the electric field. We choose without the loss of generality  $\mathbf{E} = -E\hat{\mathbf{z}}$ . An electron whose initial momentum  $\mathbf{p}_0 = p_0\hat{\mathbf{z}}$  is directed opposite to  $\mathbf{E}$  can become a runaway electron or start an avalanche, or can gradually lose energy in collisions and thermalize. Its “fate” is determined by the rate of frictional energy loss (dynamic friction function) and by the rate of parallel momentum loss (redirection to perpendicular components due to angular diffusion) due to elastic collisions.

The collisions of electrons with neutrals is a stochastic process; therefore we can

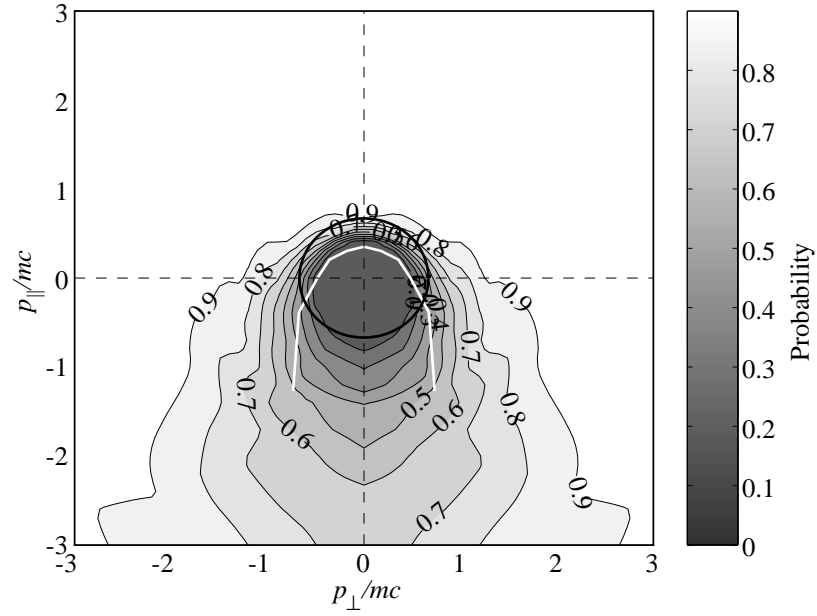


Figure 2.6: **Runaway region boundary.** The probability for an electron with a given momentum to become a runaway for  $\delta_0 = 5$  and no magnetic field ( $\eta_0 = 0$ ). The direction of  $\mathbf{E}$  is downward (electrons accelerate upward). The white line is the boundary of runaway region if the motion of an electron is deterministic. The circle has radius  $p_s$  and represents the actual boundary of the runaway region when the stochastic angular diffusion effects are included (see text).

only assign a probability for an electron to become a runaway or start a runaway avalanche. Using the Monte Carlo technique, we can estimate this probability by running the simulation many times and approximating the probability with the fraction of runs in which the electron eventually gains energy  $\gtrsim 50 mc^2$ . In Figure 2.6, we plot the probability for an electron with given initial momentum vector to become a runaway, calculated in this way. The electric force  $q_e \mathbf{E}$  on the electron is upward. The probability for an electron to start an avalanche (i.e., create several new electrons) was also calculated and turned out to be almost the same, within statistical error. The white line is a separatrix of the runaway region calculated from the deterministic equation of motion (2.1) with  $\mathbf{\Gamma} = -\hat{\mathbf{p}}F_D$ , which neglects stochastic scattering [Gurevich et al., 1992; Roussel-Dupré et al., 1994]. For higher momentum values outside the separatrix, in the absence of angular diffusion, electrons are in the runaway region, whereas inside it, they are gradually slowed down. As expected, since the motion of the electrons is stochastic, our Monte Carlo results indicate that this boundary is in fact diffuse. There is a finite probability for an electron with a small energy (less than the minimum energy given by the white line) to become a runaway, if it by chance experiences less energy losses than average. On the other hand, there is a possibility for electrons with higher energy to lose all of their energy in collisions and thermalize. The boundary of the runaway region, as calculated using Monte Carlo calculations, lies at a higher value of  $p$  than predicted by the deterministic separatrix, due to elastic scattering. This value is estimated analytically as explained below and is represented in Figure 2.6 by the black circle.

We now confirm the results of our Monte Carlo computation by finding the avalanche rates analytically from the Fokker-Planck equation [Roussel-Dupré et al., 1994] for the momentum distribution function  $f(\mathbf{p}, t) = f(p, \mu, t)$ , where  $\mu = \cos \theta$ ,  $\theta$



being the angle between the electron momentum and electric force  $q_e \mathbf{E}$ . This equation can be written in the form (see Appendix B):

$$\frac{\partial f}{\partial t} = \frac{1}{p^2} \frac{\partial}{\partial p} \{p^2 (F_D - q_e E \mu) f\} + \frac{\partial}{\partial \mu} \left\{ (1 - \mu^2) \left( -\frac{q_e E}{p} f + D \frac{\partial f}{\partial \mu} \right) \right\} + S_i(\mathbf{p}) \quad (2.23)$$

where  $F_D$  is the dynamic friction force,  $D$  is the angular diffusion coefficient due to small-angle collisions,  $S_i(\mathbf{p})$  is the ionization integral depending on the electron momentum space distribution  $f$ :

$$S_i(\mathbf{p}) = S_i(p, \mu) = \int N_m Z_m v' \left. \frac{d\sigma_{\text{ion}}}{d^3 \mathbf{p}} \right|_{\mathbf{p}'} f(\mathbf{p}') d^3 \mathbf{p}'. \quad (2.24)$$

Note that here the primed variable  $\mathbf{p}'$  is the momentum of the primary electron and  $\mathbf{p}$  of the secondary electron, contrary to the convention of (2.14) and equations following it. In equation (2.23), the derivative terms in the right-hand side can be interpreted as follows. The derivative  $\partial/\partial p$  describes changes in  $p$  without changes in direction, due to dynamic friction and an electric force component  $q_e E \cos \theta$ . The derivative  $\partial/\partial \mu$  describes changes in the direction of  $\mathbf{p}$ , due to an electric force component  $qE \sin \theta$ , which “bunches” electrons in the forward direction, and the angular diffusion which scatters electrons away from the forward direction. Let us assume that the equilibrium in angles is achieved much faster than it takes for  $p$  to change, due to the relatively high value of  $D$ . This condition must be true in particular near the boundary of the runaway region, where  $p$  changes relatively slowly (see below). The equation for the angular equilibrium is obtained by equating the  $\partial/\partial \mu$  term in (2.23) to zero:

$$\frac{\partial}{\partial \mu} \left\{ (1 - \mu^2) \left( -\frac{q_e E}{p} f + D \frac{\partial f}{\partial \mu} \right) \right\} = 0,$$

the solution of which is

$$f(p, \mu, t) = C(p, t) \exp\left(\frac{q_e E}{pD} \mu\right). \quad (2.25)$$

We now return to equation (2.23). After substituting a self-similar distribution function such that  $\partial f / \partial t = \gamma_R f$ , and averaging over angles, (2.23) can be rewritten as

$$\gamma_R f_p = \frac{1}{p^2} \frac{\partial}{\partial p} \{p^2 [F_D - q_e EM(p)] f_p\} + S_{ip}(p), \quad (2.26)$$

where

$$f_p(p, t) = \frac{1}{2} \int_{-1}^1 f(p, \mu, t) d\mu,$$

$$M(p) = \frac{1}{2f_p} \int_{-1}^1 \mu f(p, \mu, t) d\mu,$$

and

$$S_{ip}(p) = \frac{1}{2f_p} \int_{-1}^1 S_i(p, \mu) d\mu.$$

The function  $M(p)$ , which is just the average value of  $\mu$  at given  $p$ , can be found using equation (2.25).

The growth rate  $\gamma_R$  can be found from equation (2.26) using an analysis analogous to [Gurevich *et al.*, 1994]. First, we note that after we integrate equation (2.26) over  $p$  (with weight  $4\pi p^2$ ), by taking the lower limit at momentum  $p_s$  such that  $F_D(p_s) = q_e EM(p_s)$ , the  $\partial/\partial p$  term disappears. In other words, there is no electron flux through the sphere  $p = p_s$ . We should thus take  $p_s$  to be the boundary of the runaway region, defined in this case as the locus of points on which  $\partial/\partial p = 0$ . The equality  $F_D = q_e EM$  also intuitively means that the dynamic friction force is balanced by the electric force component  $q_e E \cos \theta$  parallel to  $\mathbf{p}$ . The value of  $p_s$  as calculated

for the case of Figure 2.6 is represented in Figure 2.6 by a black circle.

Following *Gurevich et al.* [1994], we assume that in the ionization integral  $S_{ip}$  the electrons are described by a monoenergetic beam:

$$f_p(p') = \frac{N_R}{4\pi p^2} \delta(p' - p_0)$$

where  $\delta(\cdot)$  is the Dirac delta function. The ionization integral reduces to

$$S_{ip} = \frac{1}{4\pi p^2} N_R N_m Z_m v_0 \frac{d\sigma_{\text{ion}}}{dp}.$$

We now integrate equation (2.26) from  $p_s$  to  $\infty$  (with weight  $4\pi p^2$ ) to obtain:

$$\gamma_R \int_{p_s}^{\infty} f_p 4\pi p^2 dp = N_R N_m Z_m v_0 \int_{p_s}^{\infty} \frac{d\sigma_{\text{ion}}}{dp} dp$$

Equating the total number of runaway electrons in the left-hand side to  $N$ , we find, after changing the integration variable to energy  $\mathcal{E}$ :

$$\gamma_R = N_m Z_m v_0 \int_{\mathcal{E}_s}^{\infty} \frac{d\sigma_{\text{ion}}}{d\mathcal{E}} d\mathcal{E},$$

where  $\mathcal{E}_s$  is the critical runaway energy, corresponding to  $p_s$ , and  $\mathcal{E}_0$  (corresponding to  $p_0$ ) is the typical energy of electrons in the beam. This expression for  $\gamma_R$  is similar to that obtained by *Gurevich et al.* [1992], although there is a significant conceptual difference. *Gurevich et al.* [1992] neglect angular diffusion and use instead of  $\mathcal{E}_s$  the minimum energy of an electron moving initially perpendicular to the electric field necessary for it to become runaway. The differential ionization cross section per

energy interval  $d\mathcal{E}$  (for small  $\mathcal{E}$ ) is

$$\frac{d\sigma_{\text{ion}}}{d\mathcal{E}} \simeq \frac{2\pi r_0^2 m c^4}{v_0^2 \mathcal{E}^2}$$

New electrons can be produced by a beam of energy  $\mathcal{E}_0$  only in the interval  $\mathcal{E}_s < \mathcal{E} < \mathcal{E}_0/2$ , therefore  $d\sigma_{\text{ion}}/d\mathcal{E} \equiv 0$  outside of this interval. We find

$$\gamma_R = \frac{1}{N_R} \frac{\partial N_R}{\partial t} = \frac{2\pi N_m Z_m r_0^2 m c^4}{v_0} \int_{\mathcal{E}_s}^{\mathcal{E}_0/2} \frac{d\mathcal{E}}{\mathcal{E}^2} = \frac{2\pi N_m Z_m r_0^2 m c^4}{v_0} \left( \frac{1}{\mathcal{E}_s} - \frac{2}{\mathcal{E}_0} \right),$$

or in dimensionless units

$$\bar{\gamma}_R = \gamma_R \tau = \frac{1}{\beta_0} \left( \frac{1}{\gamma_s - 1} - \frac{2}{\gamma_0 - 1} \right)$$

Using a more exact expression for the ionization cross section as given by (2.14), we find

$$\bar{\gamma}_R = \frac{1}{\beta_0} \left[ \frac{1}{\gamma_s - 1} - \frac{1}{\gamma_0 - \gamma_s} + \frac{\gamma_0 - 2\gamma_s + 1}{2\gamma_0^2} - \frac{2\gamma_0 - 1}{\gamma_0^2(\gamma_0 - 1)} \log \left( \frac{\gamma_0 - \gamma_s}{\gamma_s - 1} \right) \right] \quad (2.27)$$

For  $\gamma_0 \rightarrow \infty$ , we have

$$\bar{\gamma}_R = \frac{1}{\gamma_s - 1}. \quad (2.28)$$

The justification of the choice of a monoenergetic distribution function and  $\gamma_0 \rightarrow \infty$  is essentially simplicity of treatment and our estimates indicate that these choices lead to negligible error. The correct rate is obtained by a convolution of (2.27) with the electron distribution function. Using self-similar distributions obtained in our Monte Carlo model, we find that the result of this convolution is different from the expression given by simple formula (2.28) by a factor ranging from  $\sim 0.8$  at  $\mathcal{E}_s = 500$  keV to  $\sim 1.01$

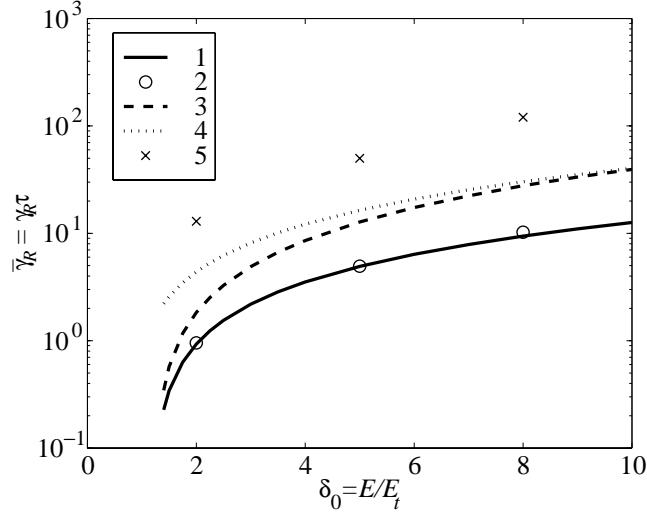


Figure 2.7: **Comparison of different runaway avalanche models.** Dimensionless runaway avalanche growth rate  $\bar{\gamma}_R = \gamma_R \tau$  in the absence of magnetic field, as a function of electric field, obtained by different models: (1) analytical expression (2.28), (2) Monte Carlo, (3) *Symbalisty et al.* [1998], (4) analytical expression (2.28) without elastic scattering, and (5) *Roussel-Dupré et al.* [1994].

at  $\mathcal{E}_s = 10$  keV.

The analytical result in (2.28) agrees well with our Monte Carlo calculations, as illustrated in Figure 2.7. The rate comparisons and values of  $\mathcal{E}_s$  are also presented in Table 2.2.

If we “turn off” elastic angular scattering by substituting  $M(p) \equiv 1$ , the avalanche rates are larger by a factor of  $\sim 4$ , as shown in Figure 2.7.

### 2.2.3 Discussion

The avalanche rates calculated by different authors and presented in Figure 2.7 are apparently quite different. While the results of *Roussel-Dupré et al.* [1994], as was shown by *Symbalisty et al.* [1997; 1998], were overestimated due to numerical error,

$\delta_0$	2	5	8	10	12
$\bar{\gamma}_R$ , model	$0.986 \pm 0.014$	$5.18 \pm 0.08$	$9.92 \pm 0.15$	$13.30 \pm 0.19$	$17.14 \pm 0.25$
$\mathcal{E}_s$ , keV	549	103	54	41	32
$\bar{\gamma}_R = mc^2/\mathcal{E}_s$	0.930	4.92	9.41	12.6	16.0

Table 2.2: **Comparison of Monte Carlo results with analytical estimates.** The Monte Carlo results and analytical estimates of the runaway electron avalanche rate calculations for  $B = 0$ . The Monte Carlo model results were derived for  $2 \times 10^4$  particles.

the rates calculated with a two dimensional kinetic model of *Symbalist et al.* [1998] still appear to be greater than both the predictions of our Monte Carlo model and our analytical computations by a factor ranging from  $\sim 1.5$  at  $\delta_0 = 2$  to  $\sim 3.5$  at  $\delta_0 = 10$ . The source of this discrepancy probably lies in the formulation of the ionization process. Assuming that the scattering occurs only at a right angle with respect to the primary electron momentum [Roussel-Dupré et al., 1994], the differential cross section for creation of electron with momentum  $\mathbf{p}$  and energy  $\mathcal{E}$  by an electron with momentum  $\mathbf{p}'$  and energy  $\mathcal{E}'$  can be written as

$$\frac{\partial \sigma_{\text{ion}}}{\partial \mathcal{E} \partial \Omega} = \frac{d\sigma_{\text{ion}}}{d\mathcal{E}} \frac{\delta(\cos \xi)}{2\pi},$$

where  $d\Omega$  is the element of solid angle,  $\xi$  is the angle between  $\mathbf{p}$  and  $\mathbf{p}'$  and  $\delta(\cdot)$  is the Dirac delta function. We can write

$$\cos \xi = \cos \theta' \cos \theta + \sin \theta' \sin \theta \cos(\phi' - \phi),$$

where  $(\theta', \phi')$  and  $(\theta, \phi)$  are the directions of incident and secondary electrons, respectively.

Neglecting the ionization energy, the ionization integral (2.24) can be transformed

into the form [Roussel-Dupré et al., 1994]:

$$S_i(\mathbf{p}) = N_m Z_m v \int d\Omega' \int_{2\mathcal{E}}^{\infty} \frac{\partial \sigma_{\text{ion}}}{\partial \mathcal{E} \partial \Omega} f(\mathbf{p}') \frac{p'^2}{p^2} d\mathcal{E}'.$$

Integrating over  $\phi'$  using the properties of the Dirac delta function, we find

$$S_i(\mathbf{p}) = N_m Z_m v \int_{-1}^1 d\mu' \int_{2\mathcal{E}}^{\infty} G_0(\mu', \mu) \frac{d\sigma_{\text{ion}}}{d\mathcal{E}} f(\mathbf{p}') \frac{p'^2}{p^2} d\mathcal{E}',$$

where  $\mu' = \cos \theta'$ ,  $\mu = \cos \theta$ , and

$$G_0(\mu', \mu) = \int_0^{2\pi} \frac{\delta(\cos \xi)}{2\pi} d\phi' = \begin{cases} \frac{1}{\pi \sqrt{1 - \mu'^2 - \mu^2}} & \text{if } \mu'^2 + \mu^2 < 1 \\ 0 & \text{if } \mu'^2 + \mu^2 \geq 1 \end{cases}$$

Instead of the above more complete expression, *Symbalisty et al.* [1998] have the following ionization integral:

$$S_i(\mathbf{p}) = N_m Z_m v \int_{2\mathcal{E}}^{\infty} \frac{d\sigma_{\text{ion}}}{d\mathcal{E}}(\mathcal{E}, \mathcal{E}') \frac{1}{2} [f(p', \mu'_+) + f(p', \mu'_-)] \frac{p'^2}{p^2} d\mathcal{E}',$$

where  $\mu'_{\pm} = \pm \sin \theta = \pm \sqrt{1 - \mu^2}$ . This corresponds to a substitution  $G_0(\mu', \mu) \rightarrow G_1(\mu', \mu)$ , where

$$G_1(\mu', \mu) = \frac{1}{2} \left[ \delta(\mu' - \sqrt{1 - \mu^2}) + \delta(\mu' + \sqrt{1 - \mu^2}) \right].$$

Physically, the usage of  $G_1$  instead of  $G_0$  means that only scattering in the plane of  $\mathbf{E}$  is allowed, i.e.,  $\mathbf{p}$ ,  $\mathbf{p}'$ ,  $\mathbf{E}$  are forced to lie in the same plane. To examine the numerical difference in the determination of the avalanche growth rate  $\gamma_R$  calculated using  $G_0$

and  $G_1$ , let us take a distribution with a spread angle  $\theta_b$  in the beam:

$$f(\mathbf{p}') = \frac{F(p')}{2\pi p'^2} \delta(\mu' - \mu_b),$$

where  $\mu_b = \cos \theta_b > 0$ . We then have

$$S_i(\mathbf{p}) = G_{0,1}(\mu_b, \mu) N_m Z_m v \int_{2\mathcal{E}}^{\infty} \frac{d\sigma_{\text{ion}}}{d\mathcal{E}} \frac{F(p')}{2\pi p'^2} d\mathcal{E}'.$$

The rate of change of the total number of particles is thus given by

$$\left( \frac{\partial N}{\partial t} \right)_{\text{ion}} = \int S_i(\mathbf{p}) d^3\mathbf{p} = K \int_{-1}^1 G_{0,1}(\mu_b, \mu) d\mu$$

where  $K$  is a proportionality constant. Therefore the rate  $[\gamma_R]_{G_1}$  calculated using *Roussel-Dupré et al.* [1994] and *Symbalist et al.* [1998] formulation of the ionization integral is greater than  $[\gamma_R]_{G_0}$  by a factor of

$$\frac{[\gamma_R]_{G_1}}{[\gamma_R]_{G_0}} = \frac{\int_{-1}^1 G_1(\mu_b, \mu) d\mu}{\int_{-1}^1 G_0(\mu_b, \mu) d\mu} = \frac{\mu_b}{\sqrt{1 - \mu_b^2}} = \cot \theta_b,$$

As the beam gets narrower at higher applied electric fields  $\delta_0 = E/E_t$ , the factor  $\cot \theta_b$  grows, and we have a growing discrepancy between two models.

In view of the key importance of the avalanche rate in the overall development of the runaway electron beam, it is important that the more accurate rates  $[\gamma_R]_{G_0}$  are used in any quantitative model of this highly nonlinear process.



### 2.2.4 Direction and Velocity of Avalanche

Of practical interest is the case when the breakdown does not start uniformly everywhere in space, but instead starts at some localized point and propagates in space. Such a case of non-uniform breakdown was previously studied analytically [Gurevich *et al.*, 1994]. Here we instead use the Monte Carlo technique, since it traces the spacial coordinates  $x$ ,  $y$ ,  $z$  of each particle. To calculate the  $e$ -folding distance, in addition to the temporal avalanche growth rate, we should also know the mean velocity of the beam. In previous works [Gurevich *et al.*, 1996; Lehtinen *et al.*, 1997], the mean beam velocity was calculated on the basis of the deterministic equation of motion of an “average electron,” neglecting stochastic scattering, an assumption which leads to inaccurate results. With our Monte Carlo method, the beam velocity  $\mathbf{v}_R$  is accurately determined by sampling the average coordinates of electrons that move away from the starting point. For example, we find that the average velocity of avalanche propagation in the absence of the magnetic field is  $|\mathbf{v}_R| \simeq 0.9$ , and with no dependence on the applied electric field within the calculation error. This value for  $|\mathbf{v}_R|$  is used in Section 4.3 when we study the runaway process in the middle atmosphere.

## Chapter 3

# Optical and $\gamma$ -Ray Emissions

Once we know the energetic electron distribution and number density, we can proceed to calculate the detectable electromagnetic emissions associated with them. In this dissertation, we consider emissions in the optical and  $\gamma$ -ray ranges. Other emissions, e.g., radio frequency emissions, which might also be produced [*Roussel-Dupré et al.*, 1998] are not considered here. The optical emissions are produced in the process of relaxation of electronic levels of atmospheric constituents. The cross-sections of optical level excitation by electrons have maxima at nonrelativistic electron energies (in the range of 10 to 100 eV), so that the relativistic electrons do not excite the molecules directly. Instead, they first produce nonrelativistic secondary electrons of required energies. There is another source of optical emissions which is relevant in a regular spark discharge when no relativistic electrons are present, i.e., when the thermal electrons are accelerated by the applied electric field to the energies required for optical excitations. This ambient heating process is also included in our calculations for optical emissions in the middle atmosphere (Chapter 4), and is well described elsewhere [*Pasko et al.*, 1997]. Unlike optical emissions,  $\gamma$ -ray emissions can

be produced only by relativistic electrons in the process of bremsstrahlung, which is due to electromagnetic emission by an accelerating electron scattered in the field of atomic nucleus (and, to a lesser degree, in the fields of individual electrons in an atom).

### 3.1 Optical Emissions

We calculate the optical emissions of molecular bands using a steady-state solution for excited state populations, similar to that utilized and described by *Bell et al.* [1995]. The steady-state solution can be used because the lifetimes of the levels (less than several  $\mu\text{s}$  [Jones, 1974, p. 119]) are small compared to the characteristic time scale of the change in the relativistic electron distribution  $\sim 1$  ms for our problem, as indicated by the terrestrial  $\gamma$ -ray flashes shown in Figure 1.3. We consider the following optical emission bands:

1. First Positive  $\text{N}_2$  group (1P), due to the transition between states  $B^3\Pi_g \rightarrow A^3\Sigma_u^+$  (denoted in this work  $B \rightarrow A$  for brevity).
2. Second Positive  $\text{N}_2$  group (2P), due to transition  $C^3\Pi_u \rightarrow B^3\Pi_g$  ( $C \rightarrow B$ ).
3. First Negative  $\text{N}_2^+$  group (1N), due to transition  $B^2\Sigma_u^+ \rightarrow X^2\Sigma_g^+$  ( $B \rightarrow X$ ).
4.  $\text{N}_2^+$  Meinel group (M), due to transition  $A^2\Pi_u \rightarrow X^2\Sigma_g^+$  ( $A \rightarrow X$ ).
5. First Negative  $\text{O}_2^+$  group (1N), due to transition  $b^4\Sigma_g^- \rightarrow a^4\Pi_u$  ( $b \rightarrow a$ ).

The emission intensities for the so-called *forbidden* “auroral” lines of atomic oxygen [Rees, 1989, p. 177], namely the red line (doublet) at 6300 Å and 6363 Å, due to the “forbidden” transition  $\text{O}(^1D_2) \rightarrow \text{O}(^3P_{2,1})$  and the green line at 5577 Å,

due to the “forbidden” transition  $O(^1S_0) \rightarrow O(^1D_2)$ , can be calculated by solving the time-evolution equations for excited state populations. However, due to the fact that the time scale of the atomic oxygen forbidden radiation transitions ( $\gtrsim 1$  s [Chamberlain, 1961, p. 580]) is much longer than the beam duration scale ( $\sim 1$  ms), the emissions due to these lines are in our case negligible compared to those of the molecular bands.

The electronic (optical) level excitation rates are calculated differently for neutral and ionized molecules, as described below, and also in a manner similar to the method used by *Bell et al.* [1995]. The excitation rate  $R_\alpha^k$ , defined as the number of molecules of species  $\alpha$  in excited state  $k$  produced in unit time per unit volume, is given by

$$R_\alpha^k = N_\alpha \int_0^\infty v f_\mathcal{E}(\mathcal{E}) \sigma_\alpha^k(\mathcal{E}) d\mathcal{E}. \quad (3.1)$$

In this equation,  $N_\alpha$  is the density of unexcited molecules,  $\sigma_\alpha^k(\mathcal{E})$  is the optical level excitation cross-section which depends on the energy of the colliding electron  $\mathcal{E}$ ,  $v$  is the colliding electron velocity, corresponding to energy  $\mathcal{E}$ , and  $f_\mathcal{E}(\mathcal{E})$  is the electron energy distribution function. The distribution function  $f_\mathcal{E}(\mathcal{E})$  is defined so that  $f_\mathcal{E}(\mathcal{E})\Delta\mathcal{E}$  gives the number of electrons in energy range  $[\mathcal{E}, \mathcal{E} + \Delta\mathcal{E}]$  in a unit volume.

For neutral molecules, it is known that the cross-sections  $\sigma_\alpha^k(\mathcal{E})$  have a maximum at low electron energy  $\mathcal{E}_\alpha^k$ , of the order of  $\sim 10$ – $100$  eV, and a shape width  $\Delta\mathcal{E}_\alpha^k$  of the same order. We therefore can write approximately

$$R_\alpha^k \simeq N_\alpha v(\mathcal{E}_\alpha^k) f_\mathcal{E}(\mathcal{E}_\alpha^k) [\sigma_\alpha^k]_{\max} \Delta\mathcal{E}_\alpha^k, \quad (3.2)$$

where  $[\sigma_\alpha^k]_{\max} \simeq \sigma_\alpha^k(\mathcal{E}_\alpha^k)$  is the maximum value of the cross-section, and the product  $f_\mathcal{E}(\mathcal{E}_\alpha^k)\Delta\mathcal{E}_\alpha^k$  can be interpreted as the number density of the relevant excitation-producing electrons.

The Monte Carlo model used in this work, designed specifically for energetic electrons, does not allow calculation of the electron distribution at energies less than the threshold  $\mathcal{E}_{\min} = 2$  keV. Therefore, we can estimate the value of  $f_\mathcal{E}(\mathcal{E}_\alpha^k)$  only indirectly by calculating the ionization produced by electrons with  $\mathcal{E} > \mathcal{E}_{\min}$  which have the known Monte Carlo distribution function  $f_\mathcal{E}^{\text{MC}}(\mathcal{E})$ . We have

$$f_\mathcal{E}(\mathcal{E})|_{\mathcal{E} < \mathcal{E}_{\min}} \simeq \frac{1}{T(\mathcal{E})} \sum_{\beta} N_{\beta} \int_{\mathcal{E}_{\min}}^{\infty} v' \sigma_{\beta}^{\text{ion}}(\mathcal{E}', \mathcal{E}) f_{\mathcal{E}}^{\text{MC}}(\mathcal{E}') d\mathcal{E}' \quad (3.3)$$

where  $T(\mathcal{E})$  is the average lifetime of electron of energy  $\mathcal{E}$  before thermalization,  $\sigma_{\beta}^{\text{ion}}(\mathcal{E}', \mathcal{E})$  is the differential ionization cross-section for species  $\beta$  as a function of the primary ( $\mathcal{E}'$ ) and secondary ( $\mathcal{E}$ ) electron energies,  $v'$  is the velocity of primary electrons, and the summation is over all atmospheric species  $\beta$ . In this estimate, we neglect the ionization process in which the electrons of energy  $\mathcal{E}$  are created by electrons with small energies  $\mathcal{E}' < \mathcal{E}_{\min}$ . In the middle atmosphere, with nitrogen and oxygen being the dominant species, we can use the average ionization cross-section  $\sigma_m^{\text{ion}} \simeq 0.2\sigma_{\text{O}_2}^{\text{ion}} + 0.8\sigma_{\text{N}_2}^{\text{ion}}$  and molecular density  $N_m = N_{\text{O}_2} + N_{\text{N}_2}$ , and avoid summation in equation (3.3).

The lifetime of electrons is given by

$$T(\mathcal{E}) = \frac{S(\mathcal{E})}{v} \quad (3.4)$$

where

$$[S(\mathcal{E})]_{\text{m}} = \frac{8.93 \times 10^{19} + 1.11 \times 10^{21}([\mathcal{E}]_{\text{keV}})^{1.67}}{[N_m]_{\text{m}^{-3}}}, \quad (3.5)$$

is the electron range, defined as the distance that an electron with initial energy  $\mathcal{E}$  traverses before it thermalizes, and  $v$  is the electron velocity. The electron range expression is taken from *Rees* [1989, p. 40]. For the values of  $\mathcal{E}$  which are relevant for optical excitations we can neglect the energy-dependent term.

The integration in equation (3.3) is performed over the distribution obtained in the course of the Monte Carlo calculation, given by

$$f_{\mathcal{E}}^{\text{MC}}(\mathcal{E}) = K \sum_{i=1}^{N_s} w_i \delta(\mathcal{E} - \mathcal{E}_i) \quad (3.6)$$

with the sum of Dirac  $\delta$ -functions taken over  $N_s$  quasi-particles with weights  $w_i$  and energies  $\mathcal{E}_i$ , and where  $K$  is the normalization coefficient determined by the fact that  $K \sum w_i$  must be equal to the number density of energetic electrons. The presence of the  $\delta$ -functions converts the integral of the form  $\int f_{\mathcal{E}}^{\text{MC}}(\mathcal{E}) G(\mathcal{E}) d\mathcal{E}$  with  $G(\mathcal{E})$  being an arbitrary function of  $\mathcal{E}$  to a sum over quasiparticles  $K \sum w_i G(\mathcal{E}_i)$ .

Using equations (3.2) through (3.6), we find the excitation rate for the optical level  $k$  to be

$$R_{\alpha}^k \simeq 8.93 \times 10^{19} \times K N_{\alpha} [\sigma_{\alpha}^k]_{\text{max}} \Delta \mathcal{E}_{\alpha}^k \sum_{i=1}^{N_s} w_i v_i \sigma_m^{\text{ion}}(\mathcal{E}_i, \mathcal{E}_{\alpha}^k). \quad (3.7)$$

In calculations of optical emissions in the stratified atmosphere, we also take into account the fact that the emissions come from different altitudes with different atmosphere densities.

The excitation rates of ionized states are calculated in a different, but somewhat analogous manner. Since the ambient ionization in the atmosphere is very small, the excitation of molecular ions is not an important process. Instead, the ionization by electron impact leads to the production of ions already in the excited states.

According to *Rees* [1989, p. 271], the creation of  $N_2^+$  has branching ratios  $p^A = 39\%$  and  $p^B = 11\%$ , for levels  $A$  and  $B$ , respectively, and the creation of  $O_2^+$  has  $p^b = 15\%$  for level  $b$ . Aside from the need to take into account the branching ratio  $p$ , excitation rate  $R_\alpha^k$  for the ionized states is given by an expression similar to (3.1), except for the fact that  $\sigma_\alpha^k(\mathcal{E})$  should be replaced by the total cross-section  $[\sigma_\alpha^{\text{ion}}]^{\text{tot}}(\mathcal{E})$  for ionization by an electron with initial energy  $\mathcal{E}$ :

$$[\sigma_\alpha^{\text{ion}}]^{\text{tot}}(\mathcal{E}) = \int_0^{\mathcal{E}-I_\alpha} \sigma_\alpha^{\text{ion}}(\mathcal{E}, \mathcal{E}') d\mathcal{E}', \quad (3.8)$$

where  $\mathcal{E}'$  is the energy of the secondary electron,  $I_\alpha$  is the ionization potential, and the integration is performed over the secondary electron energies  $\mathcal{E}'$ .

Following the analysis performed above and using the total ionization cross-section in place of the level excitation cross-section  $\sigma_\alpha^k(\mathcal{E})$ , we arrive at the expression for excitation rate for ions, somewhat similar to equation (3.7):

$$R_\alpha^k \simeq p_\alpha^k \times 8.93 \times 10^{19} \times K N_\alpha [\sigma_\alpha^{\text{ion}}]_{\text{max}}^{\text{tot}} \Delta \mathcal{E}_\alpha^{\text{ion}} \sum_{i=1}^{N_s} w_i v_i \sigma_m^{\text{ion}}(\mathcal{E}_i, \mathcal{E}_\alpha^{\text{ion}}) \quad (3.9)$$

where  $N_\alpha$  is the non-ionized species density,  $\sigma_{\alpha, \text{max}}^{\text{ion, tot}}$  is the maximum of the ionization cross-section, and  $\Delta \mathcal{E}_\alpha^{\text{ion}}$  is the width of the total ionization cross-section curve.

The ionization cross-section of species  $\alpha$  for the purposes of this work was fitted with expression analogous to *Rees* [1989, p. 43]:

$$\sigma_\alpha^{\text{ion}}(\mathcal{E}, \mathcal{E}') \simeq \frac{2\pi r_0^2 Z_\alpha}{v^2 (\mathcal{E}_{i\alpha} + \mathcal{E}')^2} \quad (3.10)$$

where  $r_0$  is the classical electron radius,  $Z_\alpha$  is the molecular nuclear charge,  $\mathcal{E}$ ,  $\mathcal{E}'$  are respectively the energies of primary and secondary electrons,  $v$  is the velocity of the

primary electron and  $\mathcal{E}_{i\alpha}$  is the typical ionization energy. For main molecular species we have  $\mathcal{E}_{iN_2} = 13.0$  eV,  $I_{N_2} = 15.6$  eV,  $Z_{N_2} = 14$ ,  $\mathcal{E}_{iO_2} = 17.4$  eV,  $I_{O_2} = 12.2$  eV,  $Z_{N_2} = 16$ . The values of  $\mathcal{E}_\alpha^k$ ,  $\sigma_{\alpha,\max}^k$ ,  $\Delta\mathcal{E}_\alpha^k$  for relevant species are given below:

1. The First Positive Group of  $N_2$  (level  $B$ ):  $[\sigma_{N_2}^B]_{\max} = 1.1 \times 10^{-20} \text{ m}^{-2}$ ,  $\Delta\mathcal{E}_{N_2}^B = 10$  eV,  $\mathcal{E}_{N_2}^B = 12$  eV.
2. The Second Positive Group of  $N_2$  (level  $C$ ):  $[\sigma_{N_2}^C]_{\max} = 3.8 \times 10^{-21} \text{ m}^{-2}$ ,  $\Delta\mathcal{E}_{N_2}^C = 10$  eV,  $\mathcal{E}_{N_2}^C = 16$  eV.
3. The First Negative  $N_2^+$  group (1N) (level  $B$ ):  $[\sigma_{N_2}^{\text{ion}}]_{\max}^{\text{tot}}$  is calculated from equations (3.8) and (3.10),  $\Delta\mathcal{E}_{N_2}^{\text{ion}} \simeq 38.5$  eV,  $[\mathcal{E}_{N_2}^{\text{ion}}]_{\max} \simeq 23.5$  eV.
4.  $N_2^+$  Meinel group (M) (level A): see item 3.
5. The First Negative  $O_2^+$  group (1N) (level  $b$ ):  $[\sigma_{O_2}^{\text{ion}}]_{\max}^{\text{tot}}$  is calculated from equations (3.8) and (3.10),  $\Delta\mathcal{E}_{O_2}^{\text{ion}} \simeq 41$  eV,  $[\mathcal{E}_{O_2}^{\text{ion}}]_{\max} \simeq 22$  eV.

The volume emission rates  $\varepsilon_\alpha^b$  of species  $\alpha$  in the band  $b$  are obtained from the excitation rates as a solution of a steady-state level population equation, because the level lifetimes are small compared to the characteristic time scale of 1 ms relevant for our problem. In the following equations,  $\varepsilon_\alpha^b$  is the volume emission rate of species  $\alpha$  in the band  $b$ ,  $\Lambda_\alpha^k$  is the inverse lifetime of level  $k$  in  $\text{s}^{-1}$ ,  $\Gamma_{\alpha,\beta}^k$  is the quenching rate due to collisions with species  $\beta$ , with the lifetimes and the quenching rates taken from Jones [1974], p. 119:

1. The First Positive Group of  $N_2$  (1P):

$$\varepsilon_{N_2}^{1P} = (R_{N_2}^B + \varepsilon_{N_2}^{2P}) \frac{\Lambda_{N_2}^B}{\Lambda_{N_2}^B + \Gamma_{N_2,N_2}^B N_{N_2}}$$



Here we take into account “cascading” from the higher level by the way of the emission of the Second Positive Group of  $N_2$ .

2. The Second Positive Group of  $N_2$  (2P):

$$\varepsilon_{N_2}^{2P} = R_{N_2}^C \frac{\Lambda_{N_2}^C}{\Lambda_{N_2}^C + \Gamma_{N_2, O_2}^C N_{O_2}}$$

3. The First Negative  $N_2^+$  group (1N):

$$\varepsilon_{N_2^+}^{1N} = R_{N_2^+}^B \frac{\Lambda_{N_2^+}^B}{\Lambda_{N_2^+}^B + \Gamma_{N_2^+, (N_2, O_2)}^B (N_{N_2} + N_{O_2})}$$

4.  $N_2^+$  Meinel group (M):

$$\varepsilon_{N_2^+}^M = R_{A, N_2^+} \frac{\Lambda_{N_2^+}^A}{\Lambda_{N_2^+}^A + \Gamma_{N_2^+, N_2}^A N_{N_2}}$$

5. The First Negative  $O_2^+$  group (1N):

$$\varepsilon_{O_2^+}^{1N} = R_{O_2^+}^b \frac{\Lambda_{O_2^+}^b}{\Lambda_{O_2^+}^b + \Gamma_{O_2^+, N_2}^b N_{N_2}}$$

The optical emission intensity in Rayleighs of a particular band is given as [*Chamberlain*, 1961, p. 569]:

$$I_\alpha^b = 10^{-10} \int \varepsilon_\alpha^b dl,$$

where  $\varepsilon$  is in  $m^{-3}\cdot s^{-1}$  and the integration is along the line of sight, measured in m.

## 3.2 Gamma-Ray Emissions

In this Section we consider the production of  $\gamma$  rays in the bremsstrahlung process and their propagation through the atmosphere.

### 3.2.1 Gamma Photon Production

If an electron with primary energy  $\mathcal{E}$  passes through the field of a nucleus (or atom) it is in general deflected. Since this deflection involves a certain acceleration, the electron must emit radiation, in a process called *bremsstrahlung* (braking radiation).

The bremsstrahlung process is characterized for our purposes by the *doubly differential cross-section* which is the differential cross-section of the bremsstrahlung photon production in a unit solid angle and a unit energy interval (we are not interested in the direction of the electron momentum after interaction).

We can approximately write the doubly differential cross-section as a product:

$$\frac{\partial^2 \chi}{\partial \mathcal{E}_{\text{ph}} \partial \Omega} = \Phi(\theta) \frac{d\chi}{d\mathcal{E}_{\text{ph}}} \quad (3.11)$$

Here  $\theta$  is the angle between the velocities of the incident electron and the emitted photon;  $d\Omega$  is an elementary solid angle in the photon momenta space;  $d\chi/d\mathcal{E}_{\text{ph}}$  is the differential cross-section for producing a photon of energy  $\mathcal{E}_{\text{ph}}$  in a unit interval of  $\mathcal{E}_{\text{ph}}$ , integrated over all directions of the produced photon momentum; and  $\Phi(\theta)$  characterizes the angular distribution of bremsstrahlung. The function  $\Phi(\theta)$  is normalized, so that  $\int_{4\pi} \Phi(\theta) d\Omega = 1$ , and is given by [Jackson, 1975, p. 705]:

$$\Phi(\theta) = \frac{3}{16\pi} \frac{1}{\gamma^2 (1 - \beta \cos \theta)^2} \left[ 1 + \frac{(\cos \theta - \beta)^2}{(1 - \beta \cos \theta)^2} \right], \quad (3.12)$$

where  $\gamma = 1 + \mathcal{E}/(mc^2)$  is the electron relativistic factor and  $\beta = v/c$  is the dimensionless velocity.

The expression for the cross-section  $d\chi/d\mathcal{E}_{\text{ph}}$  was obtained by *Heitler* [1954, p. 245] in the Born approximation:

$$\frac{d\chi}{d\mathcal{E}_{\text{ph}}} = \chi_0 \frac{1}{\mathcal{E}_{\text{ph}}} \frac{\bar{p}'}{\bar{p}} (\chi_1 + L\chi_2) \quad (3.13)$$

where the notations are:

$$\begin{aligned} L &= \log \left[ \frac{\bar{p}^2 + \bar{p}\bar{p}' - \gamma k}{\bar{p}^2 - \bar{p}\bar{p}' - \gamma k} \right] = 2 \log \left[ \frac{\gamma\gamma' + \bar{p}\bar{p}' - 1}{k} \right] \\ \chi_1 &= \frac{4}{3} - 2\gamma\gamma' \frac{\bar{p}^2 + \bar{p}'^2}{\bar{p}^2 \bar{p}'^2} + \frac{\zeta\gamma'}{\bar{p}^3} + \frac{\zeta'\gamma}{\bar{p}'^3} - \frac{\zeta\zeta'}{\bar{p}\bar{p}'} \\ \chi_2 &= \frac{8}{3} \frac{\gamma\gamma'}{\bar{p}\bar{p}'} + \frac{k^2}{\bar{p}^3 \bar{p}'^3} (\gamma^2 \gamma'^2 + \bar{p}^2 \bar{p}'^2) + \frac{k}{2\bar{p}\bar{p}'} \left[ \zeta \frac{\gamma\gamma' + \bar{p}^2}{\bar{p}^3} - \zeta' \frac{\gamma\gamma' + \bar{p}'^2}{\bar{p}'^3} + \frac{2k\gamma\gamma'}{\bar{p}^2 \bar{p}'^2} \right] \\ \zeta &= \log \left[ \frac{\gamma + \bar{p}}{\gamma - \bar{p}} \right] = 2 \log(\gamma + \bar{p}) \\ \zeta' &= \log \left[ \frac{\gamma' + \bar{p}'}{\gamma' - \bar{p}'} \right] = 2 \log(\gamma' + \bar{p}') \\ \chi_0 &= \frac{Z_a(Z_a + 1)r_0^2}{137} \end{aligned}$$

and  $r_0$  is the classical electron radius (see Chapter 2),  $Z_a$  is the atomic number,  $\gamma$  and  $\gamma'$  are respectively the relativistic factors of electron before and after collision,  $k = \mathcal{E}_{\text{ph}}/(mc^2)$  is the dimensionless photon energy,  $\bar{p} = p/(mc) = \gamma\beta$  and  $\bar{p}' = p'/(mc) = \gamma'\beta'$  are respectively dimensionless electron momenta before and after collision. In the expression for  $\chi_0$  we took into account the contribution from the atomic electrons [*Heitler*, 1954, p. 391]. Based on the law of conservation of energy, we have  $\mathcal{E}' = \mathcal{E} - \mathcal{E}_{\text{ph}}$ . The momentum is in general not conserved because some momentum is transferred to the nucleus.

For relativistic electrons  $\Phi(\theta)$  falls off fast for large  $\theta$ , so that the bremsstrahlung radiation is forward-directed. The angle  $\theta$  of bremsstrahlung radiation can be found if the directions of the photon  $(\theta_{\text{ph}}, \phi_{\text{ph}})$  and the initial electron momenta  $(\theta_e, \phi_e)$  are given, i.e.:

$$\cos \theta = \sin \theta_e \sin \theta_{\text{ph}} \cos(\phi_e - \phi_{\text{ph}}) + \cos \theta_e \cos \theta_{\text{ph}}.$$

In the above equation  $\theta_e$  is the angle between the velocity of an electron and the vertical,  $\theta_{\text{ph}}$  is the angle between the radiated photon and the vertical, and  $\phi_{\text{ph}}$  is the corresponding azimuthal angle.

The specific emissivity of  $\gamma$  rays (the number of photons radiated by a unit volume per unit solid angle of photon momenta per unit photon energy interval per second) is then given by:

$$\varepsilon_\gamma(\mathbf{r}, \mathcal{E}_{\text{ph}}, \theta_{\text{ph}}) = \int f(\mathbf{r}, \mathbf{p}) v \Phi(\theta) \left\{ 2N_{\text{N}_2} \frac{d\chi_{\text{N}}}{d\mathcal{E}_{\text{ph}}} + 2N_{\text{O}_2} \frac{d\chi_{\text{O}}}{d\mathcal{E}_{\text{ph}}} \right\} d^3\mathbf{p}, \quad (3.14)$$

where  $\mathbf{r}$  is the radius-vector of the source (the electron-nucleus system),  $f$  is the electron phase space distribution function,  $v$  is the initial electron velocity,  $N_{\text{N}_2}$  and  $N_{\text{O}_2}$  are atmospheric molecular densities of nitrogen and oxygen respectively (the density of other elements is negligible). The integration is taken over the electron momentum space.

In our calculations of the bremsstrahlung emissions we made the following approximations in determining the cross-sections:

1. **Born approximation.** The Born approximation conditions which were used in (3.13) are [Heitler, 1954, p. 242]:

$$\frac{Z_a}{137\beta} \ll 1; \quad \frac{Z_a}{137\beta'} \ll 1$$

where  $\beta = v/c$  and  $\beta' = v'/c$  are the initial and final velocities of the electron in units of  $c$ . When these conditions are not valid, the electron wave function cannot be approximated as a plane wave, and the Coulomb correction has to be made [Koch and Motz, 1959]. However, the contribution of nonrelativistic electrons to bremsstrahlung is small, and in our calculations we neglect the bremsstrahlung when the Born approximation conditions are not valid. For the atomic nucleus charges  $Z_a = 7$  (nitrogen) and  $Z_a = 8$  (oxygen) the electron energy at which  $Z_a \simeq 137\beta$  is  $\sim 1$  keV, so that for relativistic electron initial and final kinetic energies the Born approximation conditions are fulfilled.

2. **No screening.** The field of the nucleus is screened by the atomic electrons leading to the reduction of the bremsstrahlung intensity. This effect is particularly strong when [Koch and Motz, 1959]  $137k \ll \gamma\gamma'Z_a^{1/3}$ , i.e., for a high electron energy and low photon energies, as shown in Figure 3.1. The solid curve is plotted for the limit of complete screening, when the cross-section is [Heitler, 1954, p. 249]:

$$\frac{d\chi}{d\mathcal{E}_{\text{ph}}} = \chi_0 \frac{4}{k} \left\{ \left[ 1 + \left( \frac{\gamma'}{\gamma} \right)^2 - \frac{2\gamma'}{3\gamma} \right] \log(183Z_a^{-1/3}) + \frac{1}{9} \frac{\gamma'}{\gamma} \right\}.$$

For the electron and photon energies of interest here, this effect gives  $\lesssim 30\%$  reduction of bremsstrahlung emission and is neglected in our model calculations. This is an acceptable error, because, as we show in Chapter 4, the energetic runaway electron number density in the atmosphere at the altitudes of maximum  $\gamma$ -ray emissivity depends very strongly on the parameters of the thunderstorm above which they originate. Therefore, the determination of runaway electron density involves uncertainties substantially larger than  $\sim 30\%$ , so that the

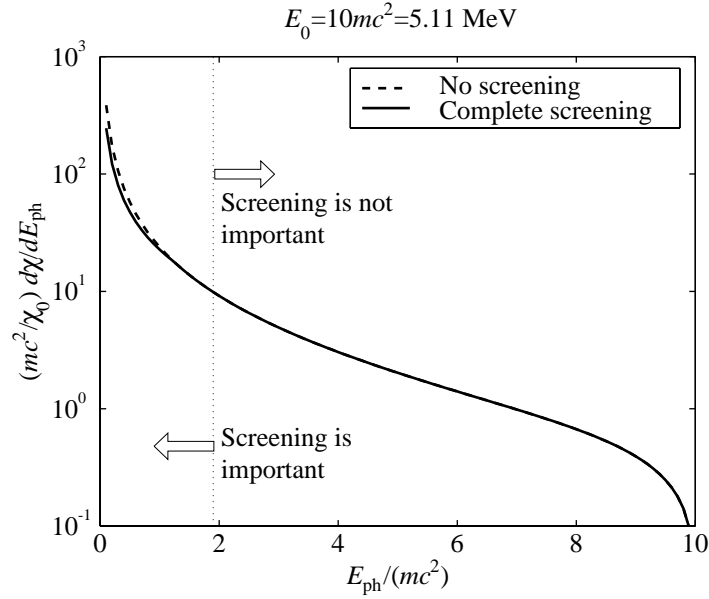


Figure 3.1: **Bremsstrahlung cross-sections.** Cross sections are shown with and without screening effect for  $\mathcal{E} = 5.11$  MeV.

screening correction would not significantly modify our conclusions regarding the properties of the  $\gamma$  emissions.

### 3.2.2 $\gamma$ -photon Propagation in the Atmosphere

The most important processes which attenuate the  $\gamma$  radiation produced by bremsstrahlung during its transport in the atmosphere are the Compton scattering and the photoelectric effect.

The *Compton scattering* describes the process in which a photon changes its direction and loses a part of its energy after a collision with an electron which is initially at rest or slowly moving. The cross section for this process is given by the Klein-Nishina

formula [Heitler, 1954, p. 219]:

$$\frac{d\sigma_C}{d\mathcal{E}'_{\text{ph}}} = \pi r_0^2 \frac{mc^2}{\mathcal{E}_{\text{ph}}^2} \left[ \frac{\mathcal{E}_{\text{ph}}}{\mathcal{E}'_{\text{ph}}} + \frac{\mathcal{E}'_{\text{ph}}}{\mathcal{E}_{\text{ph}}} + \left( \frac{mc^2}{\mathcal{E}'_{\text{ph}}} - \frac{mc^2}{\mathcal{E}_{\text{ph}}} \right)^2 - 2 \left( \frac{mc^2}{\mathcal{E}'_{\text{ph}}} - \frac{mc^2}{\mathcal{E}_{\text{ph}}} \right) \right], \quad (3.15)$$

where  $\mathcal{E}_{\text{ph}}$  and  $\mathcal{E}'_{\text{ph}}$  are initial and final photon energies,  $m$  is electron mass and  $r_0$  is the classical electron radius. The final photon energy  $\mathcal{E}'_{\text{ph}}$  can lie in an interval from  $[\mathcal{E}'_{\text{ph}}]_{\text{min}} = mc^2 \mathcal{E}_{\text{ph}} / (mc^2 + 2\mathcal{E}_{\text{ph}})$  to  $\mathcal{E}_{\text{ph}}$ .

The *photoelectric effect* describes a process in which the photon is absorbed when it removes an electron from an inner  $K$ -shell. The cross-section used in our calculations is given analytically [Price *et al.*, 1957; Heitler, 1954] and includes relativistic effects [Heitler, 1954, p. 209] as well as  $K$ -absorption edge effects [Heitler, 1954, p. 208]:

$$\begin{aligned} \sigma_P = & \sigma_0 F \frac{3}{2} \frac{Z_a^5}{137^4} \left( \frac{mc^2}{\mathcal{E}_{\text{ph}}} \right)^5 (\gamma^2 - 1)^{3/2} \\ & \left[ \frac{4}{3} + \frac{\gamma(\gamma - 2)}{\gamma + 1} \left( 1 - \frac{1}{2\gamma\sqrt{\gamma^2 - 1}} \log \frac{\gamma + \sqrt{\gamma^2 - 1}}{\gamma - \sqrt{\gamma^2 - 1}} \right) \right] \end{aligned}$$

where  $\sigma_0 = (8/3)\pi r_0^2$ , and  $\gamma = 1 + \mathcal{E}_{\text{ph}}/(mc^2)$  is the photoelectron relativistic factor.

The absorption edge factor is

$$F = 2\pi \sqrt{\frac{\mathcal{E}_{\text{ion}}}{\mathcal{E}}} \frac{e^{-4\xi \cot^{-1} \xi}}{1 - e^{-2\pi\xi}}, \quad \xi = \sqrt{\frac{\mathcal{E}_{\text{ion}}}{\mathcal{E}_{\text{ph}} - \mathcal{E}_{\text{ion}}}}$$

where

$$\mathcal{E}_{\text{ion}} = \frac{Z_a^2 mc^2}{2 \times 137^2}$$

is the  $K$ -electron ionization energy. The analytical formula for  $\sigma_P$  agrees with tabulated data [Storm and Israel, 1970; Hubbell, 1969] with  $\sim 10\%$  accuracy for photon energies  $\mathcal{E}_{\text{ph}} > 1$  keV.

Other physical processes, which are neglected in our calculations, include Rayleigh scattering and pair production. Rayleigh scattering is the coherent scattering of a photon by atomic electrons at small angles without energy loss. The ratio of the total Rayleigh cross-section to the Compton scattering cross section per atom for  $\mathcal{E}_{\text{ph}} > 10$  keV is [Price *et al.*, 1957, p. 31]

$$\frac{\sigma_R}{Z_a \sigma_C^{\text{tot}}} \simeq 1.1 \times 10^{-5} \frac{Z_a^{5/3}}{\mathcal{E}_{\text{ph}}} \ll 1 \quad (\mathcal{E}_{\text{ph}} \text{ in MeV})$$

indicating that the Rayleigh scattering effect can be safely neglected. At low photon energies  $\mathcal{E}_{\text{ph}} < 10$  keV the Rayleigh scattering cross-section is much smaller than the photoeffect cross-section [Storm and Israel, 1970]. Pair production does not play an important role for the photon energy ranges of interest ( $\mathcal{E}_{\text{ph}} \lesssim 1$  MeV) [Hubbell, 1969; Price *et al.*, 1957, p. 22].

The attenuation of a flux of photons with given energy can be expressed by the following relation between the photon flux at the detector in the absence of scattering and absorption  $I_{\gamma_0}$  and the flux in their presence  $I_\gamma$ :

$$I_\gamma = I_{\gamma_0} B e^{-\delta_{\text{opt}}}, \quad (3.16)$$

where  $\delta_{\text{opt}}$  is the optical depth, or shield thickness [Price *et al.*, 1957, p. 45], and  $B$  is the build-up factor ( $B \geq 1$ ), which takes into account the photons scattered into the detector.

The optical depth  $\delta_{\text{opt}}$  is obtained by integrating the linear “narrow beam” attenuation coefficient  $\mu$  over the radiation ray path from the point of origin  $\mathbf{r}$  to the detector location  $\mathbf{r}_{\text{det}}$ :

$$\delta_{\text{opt}} = \int_{\mathbf{r}}^{\mathbf{r}_{\text{det}}} \mu(\mathcal{E}_{\text{ph}}, \mathbf{r}') d\mathbf{r}'$$



In our case, the linear attenuation coefficient  $\mu$  has the value:

$$\mu(\mathcal{E}_{\text{ph}}, \mathbf{r}') = 2N_{\text{N}_2}(\mathbf{r}')\sigma_{\text{N}}^{\text{tot}}(\mathcal{E}_{\text{ph}}) + 2N_{\text{O}_2}(\mathbf{r}')\sigma_{\text{O}}^{\text{tot}}(\mathcal{E}_{\text{ph}})$$

where  $\sigma_{\text{N}}^{\text{tot}}$  and  $\sigma_{\text{O}}^{\text{tot}}$  are the total photon cross-sections for nitrogen and oxygen, respectively. The linear attenuation coefficient is a function of spatial coordinates [through  $N_{\text{N}_2}(\mathbf{r}')$  and  $N_{\text{O}_2}(\mathbf{r}')$ ] and the photon energy  $\mathcal{E}_{\text{ph}}$ . The total photon cross-section on the basis of the above discussion can be written as:

$$\sigma^{\text{tot}} = \sigma_P + \sigma_C^{\text{tot}},$$

where the Compton cross-section has been integrated over final photon energies  $\mathcal{E}'_{\text{ph}}$ :

$$\sigma_C^{\text{tot}} = \int_{[\mathcal{E}'_{\text{ph}}]_{\text{min}}}^{\mathcal{E}_{\text{ph}}} \frac{d\sigma_C}{d\mathcal{E}'_{\text{ph}}} d\mathcal{E}'_{\text{ph}}.$$

In the runaway electron avalanche above a thunderstorm, which is the subject of Chapter 4, most bremsstrahlung photons are produced at altitudes 60–70 km [Lehtinen *et al.*, 1997; 1999]. The optical depth for photon energies 20–500 keV in the vertically upward direction from these altitudes toward an orbiting satellite is less than  $10^{-2}$ . Therefore, the attenuation is  $\lesssim 1\%$  and can be neglected. The build-up factor can also be neglected because  $B \simeq 1$  for thin targets.

However, the Compton scattering of photons produced by precipitating electrons (Chapter 6) or of  $\gamma$  photons of extraterrestrial origin incident on the upper atmosphere [Inan *et al.*, 1999] changes their direction significantly. Equation (3.16) for this situation contains a complicated unknown build-up factor  $B$  and a numerical solution of the photon transport equation is required. In this work, we solve the photon

transport problem using a Monte Carlo model, as utilized by *Inan et al.* [1999]. The details of this model are given in Section A.6 in the Appendix.

## Chapter 4

# Runaway Electron Acceleration in the Middle Atmosphere

The relativistic runaway breakdown field  $E_t$  [Gurevich *et al.*, 1992] in air, described in Chapter 2 is smaller than the conventional breakdown field [Papadopoulos *et al.*, 1993] by a factor of  $\sim 10$ – $20$ . This fact indicates that the post-discharge quasi-electrostatic field in the middle atmosphere above a thunderstorm exceeds the runaway breakdown field over a larger altitude interval than the conventional breakdown field [Bell *et al.*, 1995]. Therefore avalanching runaway electrons may play a significant role in mesospheric processes (Figure 1.1). Runaway electrons are thought to be accelerated by quasi-electrostatic fields in the middle atmosphere following a positive cloud-to-ground (+CG) discharge [Bell *et al.*, 1995], the seed for the relativistic runaway electron avalanche being provided by MeV electrons from a cosmic ray shower [McCarthy and Parks, 1992]. In this Chapter, we study this process numerically

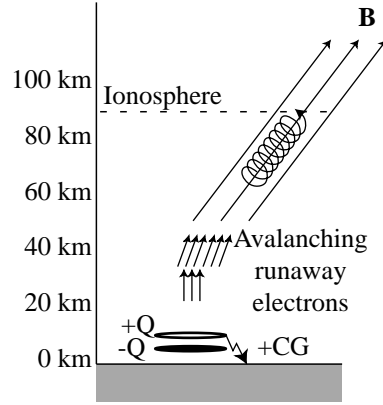


Figure 4.1: **Schematics of the runaway mechanism.** At low altitudes, where the collision rate is larger than the gyrofrequency, the electrons move along the electric field direction, while at higher altitudes they move along  $B$ .

for translationally-symmetric and axially-symmetric field configurations, using correspondingly models formulated in Cartesian and cylindrical coordinates. In Section 4.3, we provide a simple stationary analysis, to further demonstrate the highly nonlinear dependence of the runaway electron flux on the magnitude of the causative lightning discharge.

## 4.1 Cartesian Model

In our previous work [Lehtinen *et al.*, 1997], we studied the production of runaway electrons above thunderstorms using a cylindrically symmetric model with a vertical axis and a vertical geomagnetic field. Red sprites have been observed at magnetic latitudes ranging from  $10^\circ$  to  $50^\circ$ , and terrestrial gamma ray flashes have been observed throughout the equatorial region covered by CGRO, namely  $\pm 28.5^\circ$  geographic latitude. These low-latitude regions are characterized by a large angle between the

geomagnetic field and the vertical, which makes the cylindrically symmetric model inadequate to describe energetic electron discharges, since the magnetic field influences the electron motion to a large extent at high altitudes [Lehtinen *et al.*, 1997; Gurevich *et al.*, 1996].

In this Section we develop a two dimensional Cartesian model which allows an arbitrary direction for the geomagnetic field. The model is translationally symmetric in a horizontal direction and is applicable to the case of lightning draining positive charge from remote regions of a laterally extensive ( $>100$  km) storm front. The length of the cloud must be at least the size of the region modeled. The discharge in our model is characterized by the removal of charge which is distributed horizontally, and the magnitude of which is described by a line charge density (in units of C/km).

We apply the Monte Carlo model results (Chapter 2) to calculate the energetic runaway electron density and proceed to calculate optical and  $\gamma$ -ray emissions. We present results for optical emissions in the  $N_2$  first positive band system, which is dominant in red sprites. The flux of  $\gamma$ -ray emissions from energetic runaway electrons from bremsstrahlung [Lehtinen *et al.*, 1996] is also calculated and the  $\gamma$ -ray emission properties are compared to BATSE observations [Nemiroff *et al.*, 1997].

The two dimensional model presented here uses Cartesian coordinates and is translationally symmetric (invariant) in the horizontal  $y$  direction. For the results presented here we chose the geomagnetic field  $\mathbf{B} = B \sin \lambda_m \hat{\mathbf{x}} + B \cos \lambda_m \hat{\mathbf{z}}$ , with  $B = 5 \times 10^{-5}$  T,  $\lambda_m = 30^\circ$ , where  $z$  is a vertical axis. This field lies in  $(x, z)$  plane perpendicular to the linear charges. The results for the field in the  $(y, z)$  plane are similar to those presented here.

The initial thundercloud charge consists of two infinitely long line charges of density  $\pm\rho_l$  at altitudes of  $h_+ = 10$  km and  $h_- = 5$  km, respectively, which have a Gaussian spatial distribution (along  $x$  and  $z$  coordinates) with a scale of  $\sim 3$  km each. The separated dipole charges are assumed to be established over a relatively long time ( $>100$  s). We calculate the pre-discharge electrostatic field using the electrostatic heating model [Pasko *et al.*, 1998a]. Subsequently, the positive part of the dipole charge is discharged to ground in  $\tau_s = 1$  ms, as shown in Figure 4.1, thereby creating the quasi-electrostatic field due to uncompensated space charge [Pasko *et al.*, 1997]. We use an exponential ambient ion conductivity profile with  $\sim 6$  km scale height [Dejnakarintra and Park, 1974], as in previous work [Pasko *et al.*, 1997; Lehtinen *et al.*, 1997]. This conductivity profile does not include the effect of cloud aerosols, but otherwise provides a realistic representation of experimental data [Holzworth *et al.*, 1985].

The dynamics of the electric field and charge distribution is calculated by taking advantage of the relatively slow variation of the electric field and describe it using a time-varying potential as  $\mathbf{E} = -\nabla\Phi$  where  $\Phi = \Phi(\mathbf{r}, t)$ . The quasi-electrostatic approximation is based on an assumption that the ratio of the spatial scale in the model to the time scale is much less than the speed of light. The time scale is the relaxation time  $\tau_r = \epsilon_0/\sigma_0$ , which below 90 km indeed satisfies this condition. Here  $\sigma_0$  is the scalar conductivity while  $\epsilon_0 \simeq 8.54 \times 10^{-12}$  F-m<sup>-1</sup> is the permittivity of the free space. On the boundaries of the simulation box ( $x = 0, 100$  km,  $z = 0, 80$  km) we assume zero potential, i.e.,  $\Phi \equiv 0$ .

The quasi-electrostatic field equations, modified from previous work [Pasko *et al.*,

1997] to account for the presence of runaway electrons, are:

$$\frac{\partial \rho}{\partial t} + \nabla \cdot \mathbf{J} + \nabla \cdot \mathbf{J}_R = \frac{\rho_s \sigma_0}{\epsilon_0} \quad (4.1)$$

$$\nabla \cdot \mathbf{E} = \frac{\rho + \rho_s}{\epsilon_0}. \quad (4.2)$$

Here  $\rho_s = \rho_s(t)$  is the source thundercloud charge density;  $\rho$  is the induced charge density,  $\mathbf{J} = \vec{\sigma} \mathbf{E}$  is the conductivity current  $\mathbf{J}_R = q_e \mathbf{v}_R N_R$  is the current due to runaway electrons with mean velocity  $\mathbf{v}_R$  and number density  $N_R$ . The term on the right-hand side of the continuity equation (4.1) describes the external current  $\nabla \cdot \mathbf{J}_{\text{ext}} = -\rho_s \sigma_0 / \epsilon_0$ , supported by meteorological processes, with  $\sigma_0$  being the conductivity at the altitude of the charge, at which the conductivity does not appreciably depend on the geomagnetic field and can be considered a scalar.

In general, the conductivity is a tensor  $\vec{\sigma}$  due to the anisotropy introduced by the geomagnetic field. In a coordinate system in which the  $z'$  axis is along the geomagnetic field, the conductivity tensor is given by [Volland, 1984, p. 8]:

$$\vec{\sigma} = \begin{pmatrix} \sigma_p & \sigma_h & 0 \\ -\sigma_h & \sigma_p & 0 \\ 0 & 0 & \sigma_0 \end{pmatrix}$$

where  $\sigma_p$ ,  $\sigma_h$  and  $\sigma_0$  are the so-called *Pedersen*, *Hall* and *parallel* conductivities, respectively. In the case of non-vertical geomagnetic field we apply an orthogonal transformation to  $\vec{\sigma}$  by rotating the  $z'$  axis to  $z$ . The magnetic field starts to play a significant role, in which case  $\sigma_p \neq \sigma_0$  and  $\sigma_h \neq 0$ , only above 70 km [Volland, 1984,

p. 2]. The conductivity tensor elements consist of ion and electron parts

$$\sigma_0 = \sigma_i + \sigma_e \quad (4.3a)$$

$$\sigma_p = \sigma_i + \sigma_e \frac{1}{1 + \omega_H^2/\nu_{\text{eff}}^2} \quad (4.3b)$$

$$\sigma_h = \sigma_e \frac{\omega_H/\nu_{\text{eff}}}{1 + \omega_H^2/\nu_{\text{eff}}^2} \quad (4.3c)$$

The ion conductivity is given by [Dejnakarintra and Park, 1974]  $\sigma_i = \sigma_{i0}e^{z/H}$ , where  $\sigma_{i0} = 5 \times 10^{-14}$  S-m<sup>-2</sup> and  $H = 6$  km. The electron conductivity is  $\sigma_e = q_e N_e \mu_e$ , where  $N_e$  is the electron number density,  $\omega_H = q_e B/m$  is the electron gyrofrequency, and  $\nu_{\text{eff}} = q_e/(m\mu_e)$  is the effective electron collision rate. The electron mobility  $\mu_e$  is a nonlinear function of the electric field  $E$  due to heating of electrons by the quasi-static electric field  $E$ . This dependence also leads to the nonlinear dependence of the conductivity on  $E$  and is taken into account in the calculations. The energetic runaway electrons do not contribute much to the conductivity, because their density is much less than the density of ambient free electrons.

The runaway electron density  $N_R$  is calculated using the fluid equation [Lehtinen *et al.*, 1997], with the source  $S_0$  of MeV electrons provided by cosmic rays:

$$\frac{\partial N_R}{\partial t} + \nabla \cdot (\mathbf{v}_R N_R) = \gamma_R N_R + S_0(z) \quad (4.4)$$

where  $\gamma_R$  is proportional to  $\bar{\gamma}_R N_m$  as explained in Chapter 2. The local normalized avalanche rate  $\bar{\gamma}_R$  and velocity  $\mathbf{v}_R$  are functions of dimensionless parameters  $\delta_0$ ,  $\eta_0$ ,  $\mu_0$  as defined in (2.22), and are interpolated from values calculated as discussed in Chapter 2 and stored in a lookup table. No avalanche occurs for  $\delta_0$  less than a certain value, which can be  $>1$  in the presence of magnetic field. In such cases, values of



$\gamma_R \leq 0$  is obtained by extrapolation from the calculated  $\gamma_R > 0$  at higher values of  $\delta_0$ . The crudeness of this approximation can be justified by the fact that in the middle atmosphere the regions where the avalanche is quenched do not have many energetic electrons and therefore do not play any role in the development of the avalanche. The source  $S_0(z)$  is due to cosmic rays and is proportional to the air density, with  $S_0 \simeq 10 \text{ m}^{-3}\text{s}^{-1}$  at 10 km [Bell *et al.*, 1995].

The runaway electrons produce electron density enhancements through the ionization process. The change in electron density due to runaway electrons is given by

$$\frac{\partial N_e}{\partial t} = 2v_R N_R N_m \sigma^{\text{ion}}$$

where  $\sigma^{\text{ion}} \simeq 2.3 \times 10^{-22} \text{ m}^{-2}$  is the typical total cross-section for ionization by energetic runaway electrons for oxygen or nitrogen [Bell *et al.*, 1995].

For computational simplicity, we do not account for the change of conductivity associated with ionization by the quasistatic electric field. This effect leads to conventional breakdown and development of streamer channels, requiring the grid size in our model to be smaller than the streamer size, which is  $\lesssim 10 \text{ m}$  at 70 km altitude [Pasko *et al.*, 1998b]. The formation of the streamers do not influence the large scale configuration of the quasi-electrostatic field, and can be neglected for the time periods of interest here, which is  $\sim 1\text{--}3 \text{ ms}$  since the beginning of the discharge. This approximation is valid because the streamers, moving with the speed of  $< 2 \times 10^6 \text{ m}\cdot\text{s}^{-1}$ , propagate only by  $\lesssim 6 \text{ km}$  distance. Ionization effects were considered in detail in [Lehtinen *et al.*, 1997].

We solve (4.4) in two dimensions using the modified upwind differencing scheme [Press *et al.*, 1992, p. 832]. We calculate  $N_R$  at the current time step using its value at the point in space where the particle was located at time  $(t - \Delta t)$ . The values

between the grid points are obtained by bilinear interpolation. The von Neumann stability analysis [Press *et al.*, 1992, p. 827] shows that this method is unconditionally stable. Note that the error is unacceptably high for a mesh size  $\gtrsim c/\gamma_R$ , if one solves (4.4) directly for  $N_R$ . This condition can be avoided and the error can be reduced by solving (4.4) for  $\log(N_R)$ , which is analogous to an analytical solution with constant  $\gamma_R$  and  $S_0$ .

Gurevich *et al.* [1994] showed that transverse diffusion of the runaway electron beam occurs due to ionizing collisions. Using equations (26) and (31) and Figure 6 from Gurevich *et al.* [1994], we find that the beam broadening due to this kind of diffusion is  $\lesssim 1$  km, small compared to the broadening due to the fact that the avalanche is started not by a single electron, but by many electrons at different horizontal distances from the axis. The latter effect gives  $\sim 10$ – $15$  km horizontal size of the beam at the 80 km altitude, defined at the level of  $e^{-1}$  of the value on the axis. The fact that the transverse diffusion is negligible justifies our use of the fluid equation (4.4) rather than a kinetic solution.

The optical emissions are produced as a result of the excitation of neutral species through impacts by thermal electrons driven by the electric field [Pasko *et al.*, 1997] and suprathermal electrons ( $\gtrsim 10$  eV), created in the runaway avalanche. The former process is described in Chapter 3. A simplified form of the method (such as used by Bell *et al.* [1995]) is applied in this Chapter to find the optical emissions by runaway electrons. Calculation of optical emissions due to thermal electrons driven by the electric field is described elsewhere [Pasko *et al.*, 1997].

Gamma ray production is also calculated as in the paper by Lehtinen *et al.* [1997] using the method described in Chapter 3, except that we use the new electron distribution in momentum space, obtained by Monte Carlo simulation for parameters  $\delta_0$ ,

$\eta_0$ , and  $\mu_0$  corresponding to the point at which the volume emission rate proportional to  $N_m N_R$  has a maximum, which occurs at  $\sim 65$  km altitude. The emission patterns of each particle in the set are summed, as in equation (3.14). Because the atmosphere is optically thin ( $\delta_{\text{opt}} \lesssim 0.01$ ) at the altitude of maximum volume emission rate, we do not take Compton scattering or the photoelectric attenuation effects into account in our calculations of the gamma ray flux at the satellite altitudes.

The results of the Cartesian model of the middle atmosphere are presented in Figures 4.2 and 4.3 for a discharge which removes a linear charge density  $\rho_l = 12$  C/km. For calculations of values integrated over the total volume including the axis of symmetry we assume the size of the region over which charge is removed to be  $L = 100$  km, so that the total charge removed in the discharge is  $Q = \rho_l L = 1200$  C. The cloud length of 100 km is the minimum possible length for which the assumption of approximate translational symmetry (invariance) is still valid, because it is of the order of other dimensions of the system (e.g. the distance between the Earth surface and the ionosphere). The discharge can have a significant effect on the electric field at altitudes where the typical time of field relaxation ( $\tau_r = \epsilon_0/\sigma_0$ ) is greater than the time of discharge. To get the maximum observed currents of  $\sim 200$  kA, the total charge of 1200 C has to be removed in  $\sim 6$  ms, which in our model would have the same effect as instantaneous removal at altitudes below 80 km. The geomagnetic field dip angle for these results is  $60^\circ$ , corresponding to midlatitudes, where sprites are usually observed. We can use the fluid model of the runaway avalanche when the spatial diffusion of runaway electrons due to the different effect of magnetic field on electrons with different energy is not too large. Such is the case for a  $60^\circ$  dip angle, when the geomagnetic field  $\mathbf{B}$  is sufficiently close to the vertical. The spatial diffusion

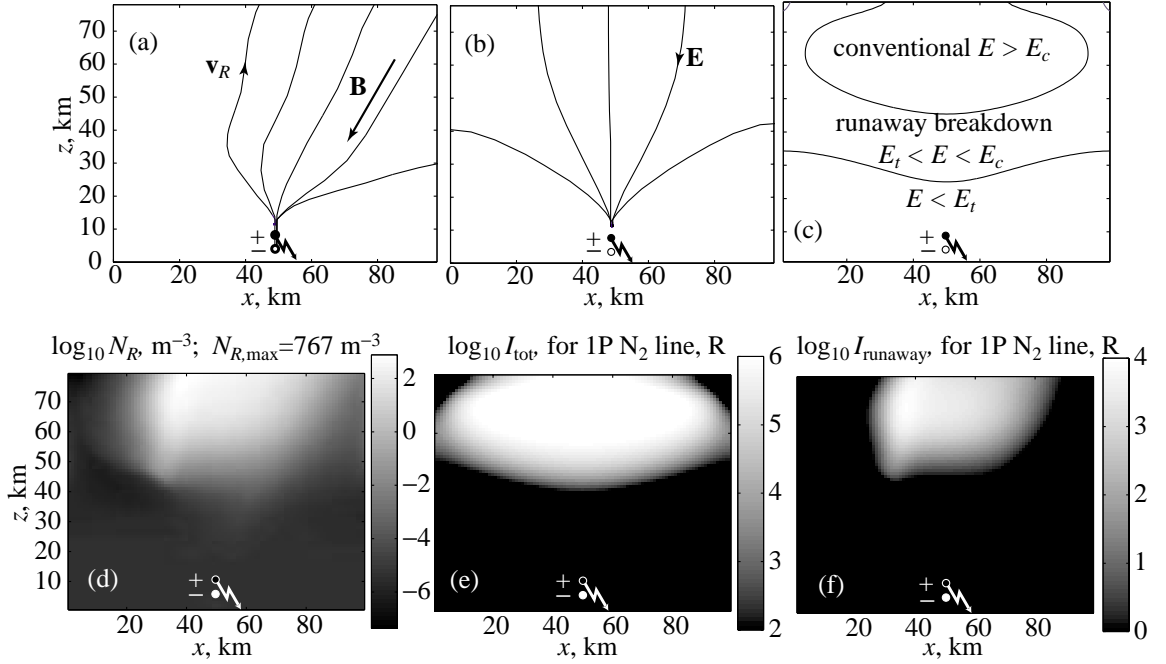


Figure 4.2: **Cartesian model results.** The runaway electron avalanche in the atmosphere for a charge moment of  $\rho_l = 12 \text{ C}\cdot\text{km}^{-1}$  at  $t = 3 \text{ ms}$  after the start of the discharge.  $\mathbf{B}$  lies in the plane of the picture. (a) Velocity field lines, (b) electric field lines, (c) electric field thresholds, (d) runaway electron density, (e) optical emissions in N<sub>2</sub> first positive band system (total), maximum is  $\sim 6.4 \text{ MR}$ . (f) Runaway electron contribution to the total luminosity shown in (e), maximum is  $\sim 8.8 \text{ kR}$ .

of electrons becomes important when  $\mathbf{B}$  is close to a horizontal, e.g., at the geomagnetic equator. The orbit of the CGRO satellite on which the gamma ray flashes were measured is confined to  $\pm 28.5^\circ$  geographic latitudes, so that some terrestrial gamma ray flashes may have originated at the geomagnetic equator, where the fluid model is insufficient for their accurate description.

Figure 4.2a shows the trajectories of runaway electrons calculated on the basis of our Monte Carlo model and the fluid model. We see that electrons move along electric field lines at lower altitudes and along geomagnetic field lines at higher altitudes. The altitude at which the regime of motion changes is around 35 km. At this altitude,

the electron elastic collision rate is roughly equal to gyrofrequency, indicating that elastic collisions play a more important role than inelastic ones [*Roussel-Dupré and Gurevich*, 1996; *Taranenko and Roussel-Dupré*, 1997]. For comparison, the inelastic collision rate is equal to the gyrofrequency at altitudes  $\sim 20$  km [*Gurevich et al.*, 1996]. There is also a drift velocity component perpendicular to the plane of the picture at higher altitudes, where the influence of magnetic field on electron motion is important.

The regions of runaway and conventional air breakdown, which occurs at  $\delta_0 \gtrsim 10$  are shown in Figure 4.2c. Figure 4.2d shows the two dimensional structure of the runaway beam. The basic difference with our previous work [*Lehtinen et al.*, 1997] is that the runaway density grows slower, since the avalanche rates are smaller by a factor of  $\sim 10$  than those used in [*Lehtinen et al.*, 1997].

Figure 4.2e shows total optical emissions in the 1st positive band system of  $N_2$ . The intensity in Rayleighs is obtained by integrating the emission rate along the line of sight, which is taken parallel to the linearly extended charge distribution and is thus  $\sim 100$  km long. Figure 4.2f shows the relatively weak optical emissions produced by the electrons in the runaway beam, indicating that the emission rate is dominated by the conventional breakdown. Note that Figure 4.2e shows emissions before conventional breakdown, because our model does not take into account the change of conductivity associated with ionization. Therefore, averaged over the frame rate ( $\sim 17$  ms) the total emission intensities will be smaller. Nevertheless, comparison of Figures 4.2e and 4.2f illustrates that the contribution of the runaway process to the total optical intensities produced at high altitudes after positive lightning discharges is negligible, unlike our previous result reported by *Lehtinen et al.* [1997] and unlike suggestions of other workers [*Taranenko and Roussel-Dupré*, 1996; *Roussel-Dupré et al.*, 1998; *Yukhimuk*

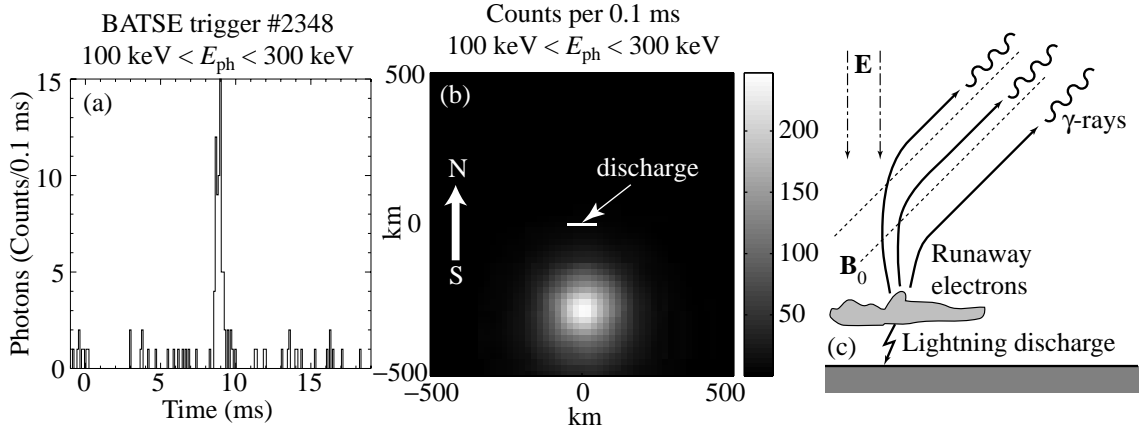


Figure 4.3: **Calculated terrestrial gamma ray flashes.** (a) Sample of BATSE observation, (b) simulated terrestrial gamma ray flashes as seen by BATSE, at  $\sim 45^\circ$  northern latitude in the photon energy interval 100–300 keV, and (c) schematics of gamma ray emission.

*et al.*, 1998].

Based on Figure 2.2 and the fact that  $N_R$  has reached  $\sim 767 \text{ m}^{-3}$  in  $\sim 1 \text{ ms}$ , the growth rate of  $N_R$  is very high at  $\sim 80 \text{ km}$ . However, this rapid increase in the runaway current  $J_R$  does not produce any significant electromagnetic radiation. Estimates indicate  $E_{\text{rad}} \lesssim 0.1 \text{ V}\cdot\text{m}^{-1}$  at  $\sim 80 \text{ km}$ , much smaller than the quasi-electrostatic field, confirming the validity of the quasi-electrostatic approximation. Note that this value is also substantially smaller than the peak intensity of the electromagnetic pulses produced by the parent lightning discharges, which are of the order  $\sim 10 \text{ V}\cdot\text{m}^{-1}$  at  $\sim 80 \text{ km}$  altitude and which produce brief optical flashes known as “elves” [Inan *et al.*, 1996a; Inan *et al.*, 1997].

Figure 4.3 shows bremsstrahlung  $\gamma$ -ray emissions. A sample of observational data is given for comparison in Figure 4.3a. Figure 4.3b shows the calculated emissions at 500 km altitude of an observing satellite. The angular distribution of the emission is forward directed for relativistic electrons, which produces the “spot.” As seen in

Figure 4.3b, the angular distribution of emitted gamma rays has a width of  $\sim 15^\circ$ . Figure 4.3c is a cartoon demonstrating the production of this spot, predicting that at midlatitudes the  $\gamma$ -ray emissions are aligned with the geomagnetic field. Unfortunately, the direction of origin of terrestrial  $\gamma$ -ray flashes requires a special analysis of BATSE data and is not in the public domain, so we cannot draw a conclusion about a correlation between it and the geomagnetic field. The calculated gamma ray flux is of the same order of magnitude as the CGRO observation [*Fishman et al.*, 1994].

A significant fraction (4 out of 12 presented by *Fishman et al.* [1994]) of TGF have a duration of 3–5 ms, which agrees with the typical timescale of our calculations. Our model predicts that the  $\gamma$ -ray spectrum decreases towards higher photon energies  $\mathcal{E}_{\text{ph}}$ . The photon fluxes integrated over BATSE energy intervals (20–50, 50–100, 100–300 and  $>300$  keV) were presented in [*Lehtinen et al.*, 1996]. The spectral analysis of BATSE data [*Nemiroff et al.*, 1997] gives a photon flux dependence proportional to  $(\mathcal{E}_{\text{ph}})^\alpha$  with  $\alpha = -1.5$  to  $-0.6$ , which includes the typical bremsstrahlung value  $\alpha = -1$ . The prediction of the model described in this work is that the  $\gamma$ -ray spectrum should be a bremsstrahlung spectrum since the upward moving  $\gamma$  rays are not significantly modified by Compton scattering in the atmosphere.

## 4.2 Cylindrical Model

The axially symmetric model of runaway electrons was presented in [*Lehtinen et al.*, 1997]. However, the avalanche rates used in that paper were proven to be overestimated, as discussed above and in Chapter 2. In this section we present recalculation of some results using new and more accurate avalanche rates, obtained in Chapter 2

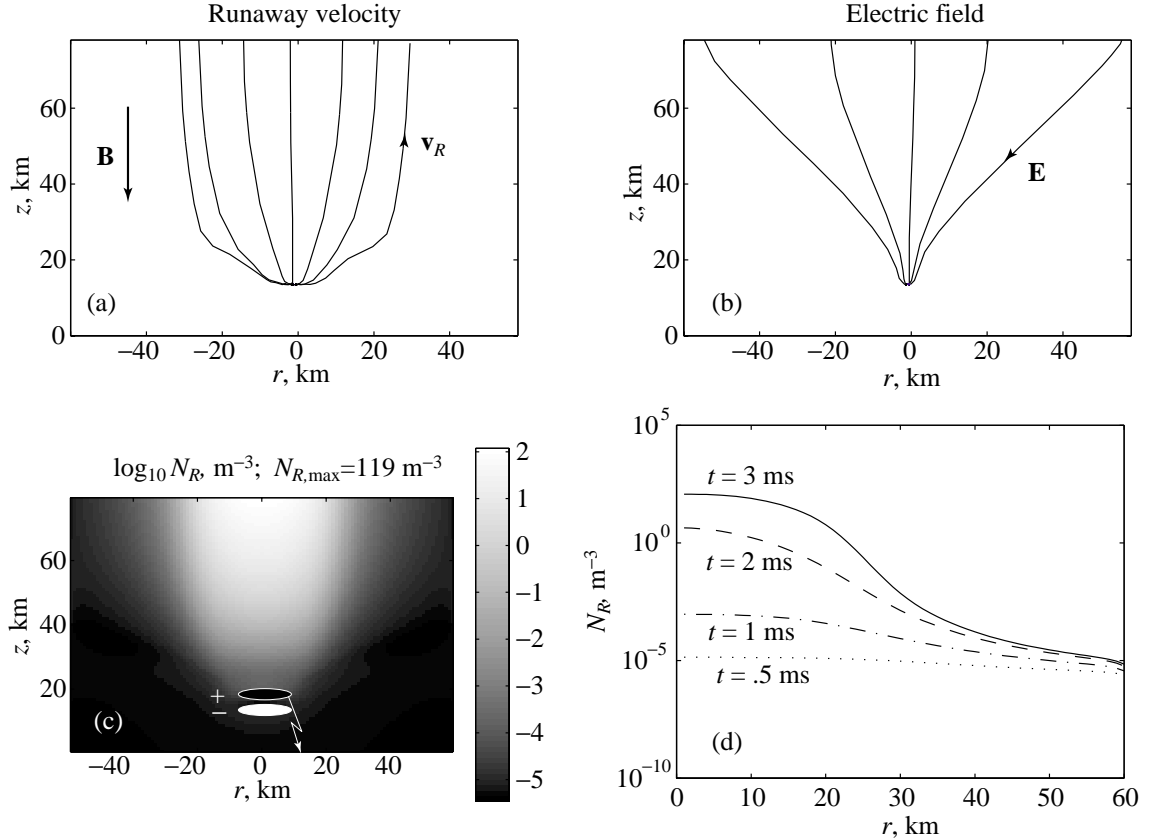


Figure 4.4: **Cylindrical model results.** The runaway electron avalanche in the atmosphere for a discharge of  $Q = 420$  C from the altitude of  $h_+ = 20$  km in time of 1 ms, at  $t = 3$  ms after the start of the discharge, in the cylindrically-symmetric model. The geomagnetic field  $\mathbf{B}$  is vertical. (a) Velocity field lines, (b) electric field lines, (c) two-dimensional spatial distribution of runaway electrons, (d) distribution of runaway electron density at the altitude of 70 km at different moments in time.



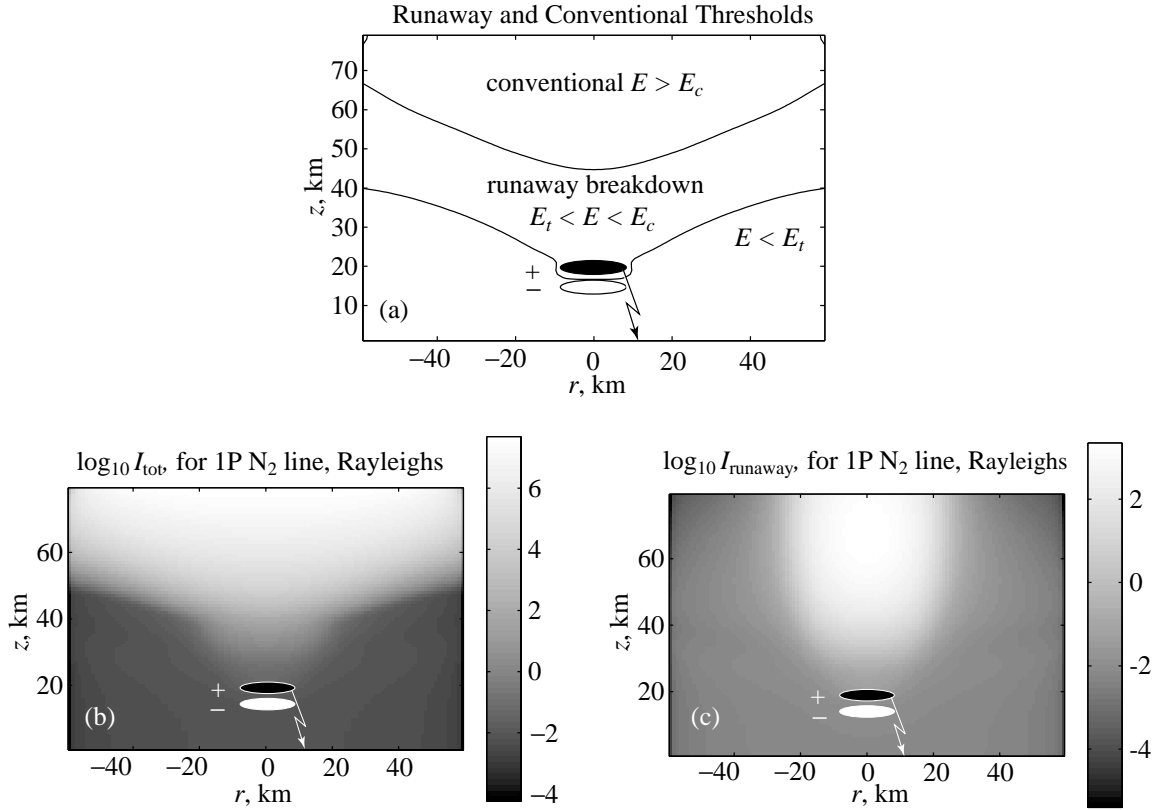


Figure 4.5: **Optical emissions in the cylindrical model.** The 2D structure of the intensity of the N<sub>2</sub> first positive band at  $t = 3$  ms after the beginning of the discharge, in Rayleighs, in the axially symmetric model. (a) Electric field thresholds, (b) optical emissions in N<sub>2</sub> first positive band system (total), (c) runaway electron contribution to it.

[Lehtinen *et al.*, 1999]. We solve equations (4.1–4.4), but now utilize cylindrical coordinates  $(r, \phi, z)$  with a vertical  $z$ -axis (axis of symmetry) and  $\mathbf{B} \parallel \hat{\mathbf{z}}$ . It should be noted that if  $\mathbf{B}$  is tilted with respect to the vertical, then the runaway electron beam is also tilted, following the magnetic field lines at high altitude.

For the results presented in Figures 4.4 and 4.5, we used a positive cloud-to-ground discharge of  $Q = 420$  C from the altitude of  $h_+ = 20$  km in time of 1 ms. The equal in magnitude stationary negative charge is located at  $h_- = 15$  km. The charge density in the cloud is assumed to be proportional to  $\exp\{-(r/a_r)^2 - ([z - h_{\pm}]/a_z)^2\}$ , with  $a_r = 10$  km and  $a_z = 3$  km. The field was calculated in the computation domain in the form of cylinder of dimensions  $r_{\max} = 60$  km and  $z_{\max} = 80$  km, with ground potential,  $\Phi = 0$ , at the boundary.

Figure 4.4a shows the trajectories of runaway electrons calculated on the basis of the fluid model using a lookup table generated via a Monte Carlo calculations as described in Section 4.1. We see that again electrons move along  $\mathbf{E}$  (shown in Figure 4.4b) at lower altitudes and along vertical  $\mathbf{B}$  at higher altitudes, and the altitude at which the regime of motion changes is around 35 km. Figure 4.4c shows the two dimensional structure of the runaway beam.

The regions of runaway and conventional air breakdown, which occurs at  $\delta_0 \gtrsim 10$  are shown in Figure 4.5a. Figure 4.5b shows total optical emissions in the 1st positive band system of  $\text{N}_2$ . The intensity in Rayleighs is obtained by integrating the emission rate along the horizontal line of sight, in the cylindrically symmetric system, perpendicular to the vertical axis. Figure 4.5c shows the relatively weak optical emissions produced by the electrons in the runaway beam, indicating that the emission rate is dominated by the conventional breakdown. Note once again that Figure 4.5c shows emissions before conventional breakdown, because our model does

not take into account the change of conductivity associated with ionization.

### 4.3 Runaway Electron Beam Density

In this Section, we estimate the runaway electron flux entering the ionosphere as a function of the thundercloud charge configuration parameters. In particular, we show that the runaway electron flux depends on the value of the cloud charge in a highly nonlinear manner.

The initial positive charge  $Q$  is taken in this Section to be either concentrated at a point or distributed on a horizontal disk located at altitude  $h_+$ . It is accompanied by an equal negative charge  $-Q$  at altitude  $h_-$ . In this Section, we consider two cases with  $h_+ = 10$  km and  $h_+ = 20$  km, while the negative charge  $-Q$  is assumed to be at  $h_- = 5$  km.

The quasi-electrostatic field after a positive cloud-to-ground discharge exists for several milliseconds, substantially longer than the few hundred microseconds required for relativistic electrons to traverse the distance from their origin to the ionosphere. We therefore use a stationary continuity equation instead of the more general (4.4) for calculation of the number density of the runaway electron beam:

$$v_R \frac{dN_R}{dz} = \gamma_R N_R + S_0(z) \quad (4.5)$$

The growth rate  $\gamma_R > 0$  only when the electric field  $E$  exceeds the runaway threshold field  $E_t$ , which is proportional to the neutral air molecule density  $N_m$ . We use the velocity  $v_R \simeq 0.9c$  and avalanche rate  $\gamma_R$  calculated using the Monte Carlo model of Chapter 2 [Lehtinen *et al.*, 1999].

In this Section, for calculation of the quasi-electrostatic field we assume an exponential air conductivity profile  $\sigma = \sigma_0 e^{z/H}$ , with scale height  $H = 10$  km, as an approximation of the experimental data [Holzworth *et al.*, 1985]. For the sake of simplicity, we neglect the changes in the conductivity described in Section 4.1 and use a substantially simple conductivity model. Based on the results of Sections 4.1 and 4.2, the effect of the changes in conductivity due to heating are negligible. The rather simple conductivity profile used here allows an analytical description of resultant electric field (see below), for the stationary case considered here and is sufficient for ballpark estimation of the number density of runaway electrons.

The removal of a positive charge is equivalent to instantaneous placement of a negative charge of equal magnitude at the same location. Since the electric field relaxation time ( $\tau_r = \epsilon_0/\sigma_0$ ) at the altitudes of avalanche is relatively long, the electrostatic field of the just-placed negative charge can be assumed to be the same as in vacuum. The driving quasi-electrostatic field is therefore the sum of the initial stationary field of the thundercloud in the conducting atmosphere and the vacuum field of the equivalent just-placed negative charge, and can be calculated analytically for both the point and disk charge configurations. In this way, the post-discharge electric field is determined predominantly by the negative screening space charge, which is formed in the pre-discharge stage, and the altitude distribution of which depends in form on the magnitude and altitude of  $Q$  and the atmospheric conductivity profile.

For point charges, we note that the Coulomb electrostatic potential of a unit charge in cylindrical coordinates located at  $r_0 = 0$ ,  $z_0 = 0$  in the stratified atmosphere with exponential conductivity profile is [Volland, 1984, p. 34]  $\Phi_{\text{exp}}^{\text{point}}(r, z) = \Phi_{\text{vac}}^{\text{point}}(r, z)e^{-(R+z)/2H}$ , where  $R = \sqrt{r^2 + z^2}$  is the distance between the observation point and the charge and  $\Phi_{\text{vac}}^{\text{point}}(r, z) = (4\pi\epsilon_0 R)^{-1}$  is the potential of a point unit

charge in vacuum.

For the case of two separated thundercloud point charges  $\pm Q$  at altitudes  $h_{\pm}$ , we have to take into account the image charges at  $-h_{\pm}$  of values  $Q_{\text{image}\pm} = \pm Q e^{h_{\pm}/H}$ . The electrostatic potential before the discharge is then given by

$$\begin{aligned} \Phi_{\text{before}}^{\text{point}}(r, z) = Q \bigg[ & \Phi_{\text{exp}}^{\text{point}}(r, z - h_+) - \Phi_{\text{exp}}^{\text{point}}(r, z - h_-) \\ & - e^{h_+/H} \Phi_{\text{exp}}^{\text{point}}(r, z + h_+) + e^{h_-/H} \Phi_{\text{exp}}^{\text{point}}(r, z + h_-) \bigg] \end{aligned} \quad (4.6)$$

The potential immediately after the discharge can be determined from (4.6) by adding a negative point charge at the location of the removed positive charge and its image:

$$\Phi_{\text{after}}^{\text{point}}(r, z) = \Phi_{\text{before}}^{\text{point}}(r, z) + Q \left[ -\Phi_{\text{vac}}^{\text{point}}(r, z - h_+) + \Phi_{\text{vac}}^{\text{point}}(r, z + h_+) \right] \quad (4.7)$$

The electrostatic field  $\mathbf{E}$  before and after discharge can then be directly found from  $\mathbf{E} = -\nabla\Phi$ . In the solution of equation (4.5) we are interested primarily in the vertical electric field  $E_z = -\partial\Phi/\partial z$  along the cylindrical axis  $r = 0$ .

For solution of equation (4.5), we assume the initial condition of  $N_{R0} = 0$  at some initial altitude  $z_{\text{ini}}$ . For calculations with  $h_+ = 10$  km, we take  $z_{\text{ini}} = 18$  km. At this altitude the ratio  $E/E_t$  after the discharge, derived from (4.7), is minimal. For  $h_+ = 20$  km, this minimum is at the cloud altitude, but we take  $z_{\text{ini}} = h_+ + 2 = 22$  km, to allow for a finite cloud thickness. We take the upper limit to be the lower ionosphere boundary at 80 km.

The point charge configuration has the disadvantage of having an arbitrarily large electrostatic potential as  $r \rightarrow 0$ . A somewhat more realistic thundercloud charge configuration is a disk of charge. The electrostatic potential of a horizontal disk charge system can be calculated by integrating the potential for the point charge.

For a unit disk charge of radius  $a$ , having a uniform charge density  $(\pi a^2)^{-1}$ , the electrostatic potential along the axis of the system in vacuum is given by

$$\Phi_{\text{vac}}^{\text{disk}}(z) = \frac{1}{\pi a^2} \int_0^a \frac{2\pi r \, dr}{4\pi\epsilon_0\sqrt{r^2 + z^2}} = \frac{1}{2\pi\epsilon_0 a^2} \left( \sqrt{a^2 + z^2} - |z| \right)$$

while the potential in the stratified atmosphere with exponential conductivity profile is given as

$$\begin{aligned} \Phi_{\text{exp}}^{\text{disk}}(z) &= \frac{1}{\pi a^2} \int_0^a \frac{e^{-(\sqrt{a^2+z^2}+z)/(2H)} 2\pi r \, dr}{4\pi\epsilon_0\sqrt{r^2 + z^2}} \\ &= \frac{H}{\pi\epsilon_0 a^2} e^{-z/(2H)} \left[ e^{-|z|/(2H)} - e^{-\sqrt{a^2+z^2}/(2H)} \right] \end{aligned}$$

The pre-discharge potential for a system of two separated disk charges is a linear combination analogous to equation (4.6), while the postdischarge potential is given by an expression similar to (4.7). The vertical component of the quasistatic electric field is once again found from  $E_z = -\partial\Phi/\partial z$ .

For a given amount  $Q$  of total removed charge, the minimum radius of a disk of charge is determined by the requirement that the field in its immediate vicinity before the discharge is lower than the runaway breakdown field  $E_t$ . The minimum radii  $a_{\text{min}}(Q)$  so determined for  $h_+ = 10$  and 20 km, are plotted in Figure 4.6.

Based on past work [Lehtinen *et al.*, 1999], the runaway electron flux  $N_R$  escaping upward from the ionosphere is insignificantly changed by the geomagnetic field for latitudes  $\gtrsim 45^\circ$ . The results of calculations of the density of the electron beam entering the magnetosphere based on a numerical solution of equation (4.5) are shown in Figure 4.7, for point and disk charges at two different altitudes. We see that the density depends strongly on the discharge value  $Q$ . The first two curves (labeled 1 and 2) are for  $h_+ = 10$  km. The first curve represents the density calculated for the

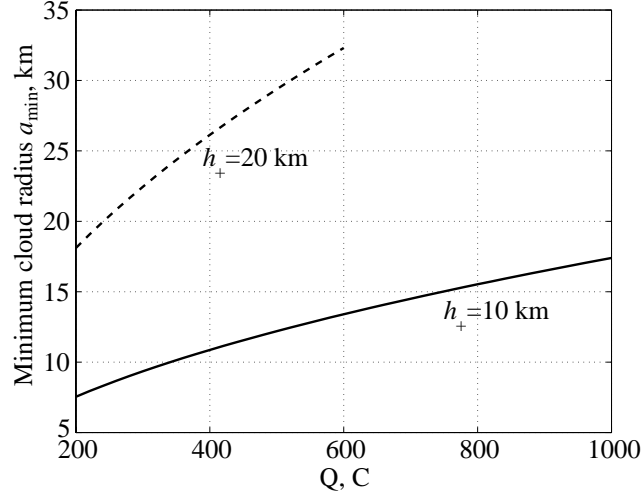


Figure 4.6: **The minimum radius of a disk charge.** The solid curve is for  $h_+ = 10$  km and the dashed curve is for  $h_+ = 20$  km.

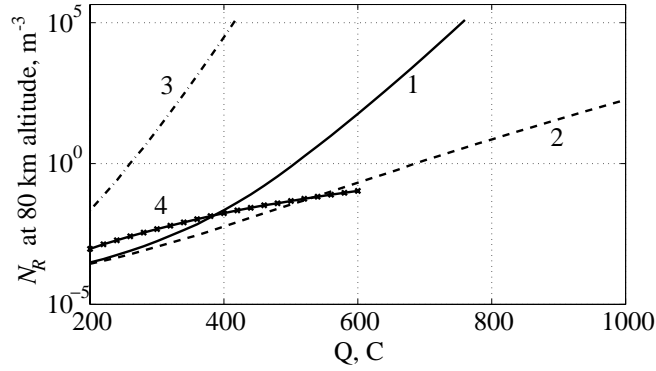


Figure 4.7: **Electron flux entering the ionosphere.** Results are shown for point and disk charges. (1)  $h_+ = 10$  km, point charge; (2)  $h_+ = 10$  km, disk charge; (3)  $h_+ = 20$  km, point charge; (4)  $h_+ = 20$  km, disk charge.

point discharge. The second curve represents results for a disk discharge, the disk radius being limited by the condition that the field never exceeds  $E_t$  either before or after the discharge. The last two curves (labeled 3 and 4) represent analogous results for  $h_+ = 20$  km. We see that the runaway electron production depends strongly not only on the value of the charge lowered to the ground, but also on its altitude. For a higher location of the initial positive charge, the runaway electron flux escaping from the lower ionosphere is much higher.



## Chapter 5

# Interhemispheric Transport and Trapped Electron Curtains

In this chapter, we consider the fate of the runaway electrons escaping the lower ionosphere, as depicted in Figure 5.1. In particular, we consider the pitch angle and energy scattering of the relativistic beam electrons due to beam-plasma interactions in the radiation belts, leading to the formation of trapped electron “curtains”.

Relativistic runaway electron beams driven upward by intense lightning-generated quasi-electrostatic fields undergo intense interactions with the background magnetospheric plasma, leading to rapid nonlinear growth of Langmuir waves. The beam electrons are strongly scattered by the waves in both pitch angle and energy, leading to the formation of an isotropic thermal distribution with a typical energy of  $\sim 1$  MeV within one interhemispheric traverse along the Earth’s magnetic field lines. While those electrons within the loss cone precipitate out, most of the electrons are trapped and continue to execute bounce and drift motions, forming detectable trapped curtains of energetic electrons.

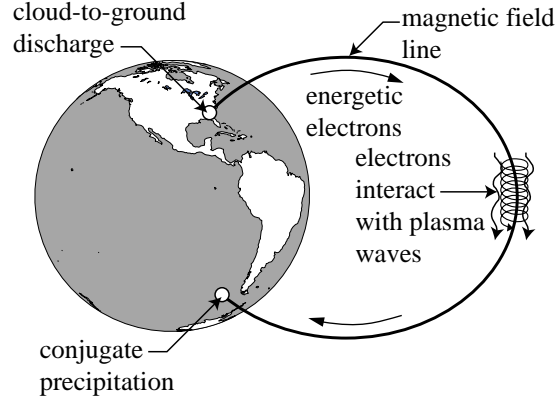


Figure 5.1: **Schematics of interhemispheric transport.** The electrons escaping from the ionosphere above a thunderstorm are going from one hemisphere to another and precipitate at the conjugate point.

The problem of a cold monoenergetic relativistic beam travelling between geomagnetically conjugate points was considered by *Khazanov et al.* [1999]. In our case, the runaway electron beam exhibits a wide range of electron energies [*Lehtinen et al.*, 1999], so that we must consider the growth rate of beam-plasma instability for the case of a beam with a significant energy spread.

We set out to determine whether the growth rate is high enough to lead to significant growth of Langmuir waves during a single interhemispheric traverse. If such growth does occur, the beam loses energy to waves and is also scattered in pitch angle. If, on the other hand, the growth rate is small, then we can conclude that the beam remains largely intact during its traverse, with most of the particles arriving into the conjugate hemisphere with pitch angles well below the loss cone and thus precipitating into the lower ionosphere.

To determine the growth rate of the beam-plasma instability, we adopt the usual procedure of using the dispersion relation describing the complex permittivity  $\epsilon(\omega, k)$  of the system to evaluate the imaginary part of frequency  $\omega$ .

## 5.1 Growth Rate of the Beam-Plasma Instability

The beam-plasma permittivity for a set of beams  $\alpha$  (all having velocities parallel to the same axis) is given by [e.g., *Stix*, 1962, p. 111]:

$$\epsilon = 1 - \sum_{\alpha} \frac{q_{\alpha}^2 N_{\alpha}}{\epsilon_0 m_{\alpha\parallel}} \frac{1}{(\omega - kV_{\alpha})^2}$$

where  $N_{\alpha}$  are the densities of the beams,  $m_{\alpha}$  and  $q_{\alpha}$  are the masses and the charges of the particles constituting the beams. For relativistic beams, we must use the mass  $m_{\parallel} = m/(1 - \beta^2)^{3/2}$ , where  $\beta = v/c$ . An individual relativistic “hot” beam having a range of parallel momenta  $p$  can be represented as a superposition of beams each with density  $N_{\alpha} = N_R f(p) dp$ , with  $f(p)$  being the momentum distribution function normalized to 1, so that the permittivity of a “hot beam - cold background plasma” system is given by

$$\epsilon(\omega, k) = 1 - \frac{\omega_0^2}{\omega^2} - \omega_0^2 \frac{N_R}{N_0} \int \frac{(1 - \beta^2)^{3/2} f(p) dp}{(\omega - kc\beta)^2}, \quad (5.1)$$

where  $N_0$  is the magnetospheric ambient plasma density and  $\omega_0 = \sqrt{e^2 N_0 / (\epsilon_0 m)}$  is the corresponding plasma frequency.

The momentum distribution of runaway electrons escaping upward from the lower ionosphere has been evaluated using a Monte Carlo method, described in Chapter 2 [also see *Lehtinen et al.*, 1999] and can be approximated with a log-normal analytical fit:

$$f(p) = \frac{1}{p} \frac{1}{\sqrt{2\pi}\sigma} \exp \left\{ -\frac{1}{2\sigma^2} \left[ \log \left( \frac{p}{p_0} \right) \right]^2 \right\}, \quad (5.2)$$

where  $p_0 = 8.9mc$  and  $\sigma = 0.94mc$  give the best fit to electron distribution for a discharge with  $Q = 500$  C at altitude of 400 km, above which Coulomb collisions can

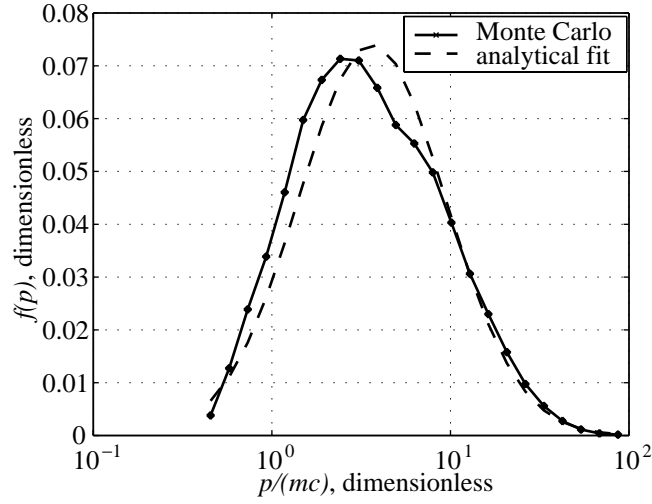


Figure 5.2: **Momentum distribution of the escaping runaway electrons.** The Monte Carlo calculation results and an analytical (log-normal) fit.

be neglected for our calculations. The distribution is shown in Figure 5.2. Monte Carlo calculations further indicate that we can neglect the perpendicular momentum component compared to the parallel momentum.

We now calculate the instability growth rate under the assumption that  $N_R \ll N_0$ . To utilize published beam-plasma system growth rate formulas for non-relativistic beams, we denote

$$F(\beta) \equiv (1 - \beta^2)^{3/2} f(p) \frac{dp}{d\beta} = mc f[p(\beta)].$$

The instability growth rate  $\text{Im } \omega$ , which is positive for time dependences  $e^{-i\omega t}$ , is found from the formula [e.g., *Krall and Trivelpiece*, 1986, p. 389]:

$$\text{Im } \omega = -\frac{\text{Im } \epsilon}{\partial \text{Re } \epsilon / \partial \omega} \quad (5.3)$$

where the values are taken at the point  $(\omega, k)$  where  $\text{Re } \epsilon = 0$ . Substituting for  $\epsilon$  from equation (5.1) we find  $\partial \text{Re } \epsilon / \partial \omega \simeq 2/\omega_0$  for small  $N_R/N_0$  and

$$\text{Im } \omega = \frac{N_R}{N_0} \frac{\pi \omega_0}{2} \left( \frac{\omega_0}{ck} \right)^2 \frac{dF}{d\beta} \Big|_{\beta=\omega_0/(ck)}$$

with a maximal value of

$$\text{Im } \omega \simeq 25 \frac{N_R}{N_0} \omega_0 \simeq 0.05 N_R \text{ sec}^{-1}, \quad N_R \text{ in m}^{-3} \quad (5.4)$$

for an assumed value  $N_0 \simeq 10^9 \text{ m}^{-3}$  and the beam distribution (5.2).

Interaction of the beam with the background plasma becomes significant if the bounce time  $t_B \simeq 0.2 \text{ sec}$  for the electron beam to traverse the geomagnetic field line is large compared to the characteristic growth time  $(\text{Im } \omega)^{-1}$ . For  $N_0 \simeq 10^9 \text{ m}^{-3}$ ,  $t_B(\text{Im } \omega) \simeq 1$  for  $N_R \simeq 100 \text{ m}^{-3}$ , so that significant pitch angle scattering and energy degradation of the beam occurs for  $N_R \gtrsim 100 \text{ m}^{-3}$ . Note that  $\text{Im } \omega$  is proportional to  $N_0^{-1/2}$ , so that the maximum interaction occurs near the equatorial plane, where  $N_0$  is a minimum.

It is instructive to compare the growth rate  $\text{Im } \omega$  calculated above for a hot relativistic beam to that of a cold monoenergetic beam. The growth rate of the beam-plasma instability for a cold monoenergetic relativistic beam in a comparatively dense cold plasma can be determined in a manner completely analogous to that of a non-relativistic beam, except for the fact that the mass of the particles in the beam must now be the relativistic parallel mass  $m_{\parallel}$ . If we use the crude monoenergetic approximation for the runaway beam and take the beam momentum  $p_0$  to be the mean momentum obtained from Monte Carlo calculations, for assumed value of  $N_0 \simeq$

$10^9 \text{ m}^{-3}$  we find a growth rate of [e.g., *Tsytoich*, 1995, p. 224]:

$$(\text{Im } \omega)_{\text{cold}} = \frac{\sqrt{3}}{2^{4/3}} \frac{\omega_0}{\gamma} \left( \frac{N_R}{N_0} \right)^{1/3} \simeq 150 N_R^{1/3} \text{ s}^{-1}, \quad (5.5)$$

where  $N_R$  is in  $\text{m}^{-3}$ , and  $\gamma = (1 - v^2/c^2)^{-1/2} \simeq 10$  is the typical relativistic coefficient of particles in the beam. The last expression was obtained by a substitution  $m \rightarrow m_{\parallel} \equiv m\gamma^3$  for the beam in the nonrelativistic expression. Comparison of value of  $(\text{Im } \omega)_{\text{cold}}$  with  $\text{Im } \omega$  from (5.4) for typical parameters indicate that the assumption of a cold monoenergetic beam results in a much higher growth rate.

## 5.2 Nonlinear Growth

The number density of the energetic electrons in the beam is estimated from comparison with experimental data on the terrestrial gamma ray flashes [*Fishman et al.*, 1994]. The gamma photon emission rate as a result of bremsstrahlung is proportional to the product of the atmosphere molecule density  $N_m$  and energetic electron density  $N_R$  (Section 3.2). According to numerical solutions of equation (4.5) and computer simulations described in Chapter 4 [*Lehtinen et al.* 1997; 1999], most  $\gamma$ -ray emissions come from altitudes of 60–75 km. The observed levels of  $\gamma$ -ray flux in this case is obtained for energetic electron densities of  $N_R \simeq 10^4$  to  $10^5 \text{ m}^{-3}$ . Other models predict maximum  $\gamma$ -photon emissivity at heights  $\sim 40$  km [*Milikh and Valdivia*, 1999] and a different maximum value of  $N_R$ .

For such high values of  $N_R$ , it is clear from (5.4) that the linear growth rate is very high, so that the instability rapidly grows into the nonlinear regime even during a single traverse of the beam between hemispheres. In such a case, the evolution of the momentum space distribution of the beam electrons can only be determined

via detailed computer simulations. While an extensive simulation of the nonlinear relativistic beam-plasma interaction is beyond the scope of this work, we nevertheless estimate the electron distribution subject to certain assumptions and with reference to published simulation results.

Based on qualitative estimates confirmed by computer simulation work [*Birdsall and Langdon*, 1991, p. 117], in the advanced non-linear stage of interaction of a one-dimensional cold and nonrelativistic electron beam with longitudinal Langmuir waves, the maximum time-average energy density of the wave field has the value:

$$W_E = \frac{1}{4}\epsilon_0 E^2 = \left(\frac{N_R}{2N_0}\right)^{1/3} W_R, \quad (5.6)$$

where  $W_R$  is the energy density in the beam. Assuming that the results do not change qualitatively for the case of a relativistic beam, and that the initial beam density is  $N_R = 10^5 \text{ m}^{-3}$ , we obtain the relative energy loss of  $W_E/W_R \simeq (N_R/2N_0)^{1/3} \lesssim 10\%$ . Note that based on the comparison of (5.4) and (5.5), the growth rate and thus the energy degradation of the beam should be even smaller for a hot initial distribution, so that the relative energy loss of  $\sim 10\%$  is an upper bound for our case.

Interaction of a monodirectional beam with oblique Langmuir waves leads to isotropization of the distribution [*Tsytoich*, 1995, p. 70]. With the beam density being so high as to lead to very large growth rate and indeed nonlinear growth, we can expect very significant pitch angle and energy scattering. As a first approximation, we assume that the electrons acquire an isotropic thermal distribution (over pitch angles and energies) during one traverse along the field line. The resultant phase space distribution can thus be taken to be the Maxwellian distribution generalized to relativistic temperatures. It is given by the canonical Gibbs distribution for an ideal gas with  $f^{\text{th}}(p)$  proportional to  $e^{-H(p)/(k_B T)}$ , where  $H(p) = \sqrt{m^2 c^4 + p^2 c^2}$  is the

Hamiltonian of a single electron. The distribution over kinetic energy is given by

$$f_{\mathcal{E}}^{\text{th}}(\mathcal{E}) = N_e C e^{-\mathcal{E}/(k_B T)} \gamma \sqrt{\gamma^2 - 1}, \quad (5.7)$$

where

$$C = \frac{e^{-mc^2/(k_B T)}}{k_B T} \left[ K_2 \left( \frac{mc^2}{k_B T} \right) \right]^{-1}$$

is the normalization factor,  $\mathcal{E}$  is the kinetic energy,  $\gamma \equiv 1 + \mathcal{E}/(mc^2)$  is the relativistic factor,  $K$  denotes the modified Bessel function, and  $N_e$  is the electron number density after the nonlinear interaction. The temperature for our parameters is found to be  $k_B T \simeq 2$  MeV, corresponding to  $C \simeq 1.3 \times 10^{-5} \text{ keV}^{-1}$ .

On the other hand, the resonance interaction of beam electrons with plasma waves with an increment given by (5.3) occurs only for electrons with energies  $\mathcal{E} < 2.3$  MeV, with the maximum growth at  $\mathcal{E} = 1.45$  MeV. This, and the mechanism of nonlinear stabilization [Tsytovich, 1995, p. 184] would tend to prevent the thermalization of the distribution at higher energies. Thus, it is difficult to predict the resultant electron distribution function without a nonlinear computer simulation analysis, a task well beyond the scope of this work.

### 5.3 Formation of Trapped Electron Curtains

For the sake of discussion, and with the above caveats in mind, we proceed by assuming that the intense beam-plasma interaction transforms the relativistic runaway beam consisting of electrons with pitch angles near zero and with an initial momentum distribution as given in (5.2) to an isotropic thermal distribution with typical energy  $\gtrsim 1$  MeV. Assuming an initial beam density of up to  $10^5 \text{ m}^{-3}$ , a beam radius of  $\sim 10$  km,



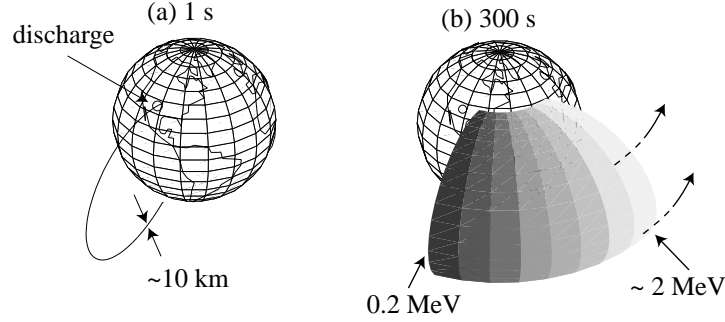


Figure 5.3: **Runaway electron curtains.** (a) Upward driven runaway electrons fill a geomagnetic tube within  $\sim 1$  s; (b) at  $\sim 300$  s, a drifting curtain is formed, due to the energy-dependent drift velocity.

and a process duration of  $\sim 1$  ms [Lehtinen *et al.*, 1997], a total of  $N_e^{\text{tot}} \simeq 3 \times 10^{18}$  electrons are initially injected into the radiation belts. After isotropization, only a small fraction ( $\sim 2$ – $10\%$ ) of these electrons are in the loss cone and precipitate in the conjugate hemisphere. The remaining electrons are trapped, and bounce back and forth between hemispheres, while at the same time drifting eastward in longitude. After a few bounces, the electrons that are not precipitated fill up the geomagnetic field tube. For  $\sim 45^\circ$  geomagnetic latitude, the length of the geomagnetic field line of  $\sim 2 \times 10^7$  m, with the geomagnetic field at the equator being smaller by a factor of  $\sim 10$ , resulting in an electron energy distribution given by (5.7) with electron density  $N_e \simeq 150 \text{ m}^{-3}$  at the equator, corresponding to a differential energy flux of electrons at  $\sim 1$  MeV of  $\Phi_{\mathcal{E}} \simeq 3 \times 10^2 \text{ el-cm}^{-2}\text{-s}^{-1}\text{-keV}^{-1}$ , with the energy dependence of the flux  $\Phi_{\mathcal{E}}$  for  $\mathcal{E} \gg mc^2$  being proportional to  $\mathcal{E}^2 e^{-\mathcal{E}/(2 \text{ MeV})}$ .

The trapped electrons drift eastward due to curvature and gradient of the geomagnetic field, with a period of [Walt, 1994, p. 49]:

$$\tau_d = 1.557 \times 10^4 \frac{1}{L\gamma\beta^2} [1 - 0.3333(\sin \alpha_{\text{eq}})^{0.62}],$$

where  $L = 2$  for  $45^\circ$  invariant magnetic latitude,  $\beta = v/c$ ,  $\gamma = (1 - \beta^2)^{-1/2}$ , and  $\alpha_{\text{eq}}$  is the equatorial pitch angle. For 1 MeV electrons at  $L = 2$ , and for  $\alpha_{\text{eq}} \simeq 90^\circ$ , we have  $\tau_d \simeq 10^3$  s. Due to the fact that electrons with higher energies drift in longitude at a greater rate, the trapped electrons eventually form electron curtains as shown in Figure 5.3. After several drift periods, when the curtain wraps around the Earth and electrons of different energies mix together, the omnidirectional flux of electrons can be estimated by comparing the 10 km longitudinal beam radius with the distance around the globe at the equator at the  $L$ -value corresponding to  $45^\circ$  invariant latitude ( $L \simeq 2$ ). Based on these considerations, we find the flux of electrons at energy  $\sim 1$  MeV at the geomagnetic equator to be  $\Phi_{\mathcal{E}} \simeq 7 \times 10^{-2}$  el-cm $^{-2}$ -s $^{-1}$ -keV $^{-1}$ .

Preliminary calculations indicate that such fluxes should be detectable on satellites with high time resolution and sensitive detectors. Noting that the latitudinal extent of the original beam is  $\sim 10$ – $20$  km, the curtains would be traversed by a polar orbiting satellite within a few seconds. A detector with a geometric factor of  $\sim 1$  cm $^2$ -sr would measure a total number of  $\sim 100$  electrons of  $> 1$  MeV energy while traversing the curtain.

# Chapter 6

## Conjugate Hemisphere Effects

In the previous Chapter, we analyzed the transport of energetic electrons along the geomagnetic field line and concluded that the initially monodirectional electron beam thermalizes and isotropizes. The energetic electrons which after scattering have pitch angles below the loss cone angle precipitate at the conjugate hemisphere. The thermal relativistic electron distribution is given by equation (5.7) with a typical temperature of  $k_B T \simeq 2$  MeV.

In this Chapter, we consider the physical effects of the precipitating particles in the conjugate ionosphere, in terms of production of light, secondary ionization and gamma ray emission. We use a Monte Carlo method to quantify these effects. Our results indicate that the effects of the beam in the conjugate mesosphere are significant and detectable.

It is important to note that the physical effects in the conjugate hemisphere that are studied in this Chapter are necessary consequences of the runaway electron acceleration process studied in Chapter 4, regardless of the manner with which the beam

interacts with the background plasma during its interhemispheric traverse (Chapter 5). If the beam is not significantly scattered during its traverse, all of the beam electrons must necessarily precipitate because they entered the magnetosphere from altitudes below the mirror altitude. If the beam is scattered in pitch angle and energy as described in Chapter 5, then the fraction of the beam electrons that end up in the loss cone is precipitated leading to the effects studied in this Chapter.

## 6.1 Energetic Electron Precipitation

With an isotropic distribution of downcoming particles impinging on the conjugate hemisphere, the fraction of the particles which are precipitated can be determined as the portion of the solid angle which lies within the loss cone. The remaining electrons mirror in the conjugate hemisphere and contribute to the population of the radiation belts, eventually forming trapped electron curtains as described in the previous chapter and in [Lehtinen *et al.*, 2000a].

The local pitch angle  $\alpha$  at the precipitation point is related to the equatorial pitch angle  $\alpha_{\text{eq}}$  as

$$\frac{\sin \alpha}{\sin \alpha_{\text{eq}}} = \sqrt{\frac{B}{B_{\text{eq}}}} \quad (6.1)$$

where  $B_{\text{eq}}$  and  $B$  are respectively the Earth's magnetic field at the geomagnetic equator, and at the precipitation point. For a simple dipole model of the Earth's geomagnetic field we have

$$\frac{B}{B_{\text{eq}}} = \frac{\sqrt{1 + 3 \sin^2 \lambda}}{\cos^6 \lambda}$$

where  $\lambda$  is the geomagnetic latitude.

The equatorial loss-cone angle is  $\alpha_{\text{eq}}^{\text{lc}} = \sin^{-1} \left[ \sqrt{B_{\text{eq}}/B} \right]$ , and assuming an isotropic

distribution of electrons at the equator, the fraction of electrons that precipitate in the conjugate region is thus given by

$$\frac{N_{lc}^{tot}}{N^{tot}} = \frac{1}{4\pi} \int_{\alpha_{eq}=0}^{\alpha_{eq}=\alpha_{lc}^{eq}} d\Omega_{eq} = \frac{1 - \cos \alpha_{lc}^{eq}}{2} = \frac{1}{2} \left( 1 - \sqrt{1 - \frac{B_{eq}}{B}} \right), \quad (6.2)$$

where  $N_{lc}^{tot}$  and  $N^{tot}$  are correspondingly the number of electrons in the loss cone and the total number of electrons. For a geomagnetic latitude of  $\sim 30^\circ$  we find from equation (6.2) that  $\sim 10\%$  of the total number of electrons in the beam are precipitated.

Let us assume that as observed at the geomagnetic equator, the total number of electrons in the beam (integrated over volume) with velocity per unit solid angle is  $F_{eq}(\alpha_{eq})$ . When the beam travels along the field line to the precipitation point, its angular distribution changes to another function  $F(\alpha)$ , which is determined from the conservation of the number of particles:

$$F(\alpha) = F_{eq}(\alpha_{eq}) \frac{\sin \alpha_{eq} d\alpha_{eq}}{\sin \alpha d\alpha}$$

and the pitch angles are related by (6.1). From this equation, we find

$$F(\alpha) = \frac{N^{tot}}{4\pi} \frac{B_{eq}}{B} \frac{\cos \alpha}{\sqrt{1 - \frac{B_{eq}}{B} \sin^2 \alpha}}, \quad (6.3)$$

where  $\alpha$  lies in the range  $[0, \pi/2]$  because we only consider downgoing electrons.

With the energy spectrum of the downgoing electrons assumed to be a thermal distribution with typical energy  $\gtrsim 1$  MeV and the pitch angle distribution given by (6.3), we now proceed to calculate the resultant effects (optical emissions, secondary

ionization and  $\gamma$ -rays) in the conjugate hemisphere by assuming an initial beam density of  $10^5 \text{ m}^{-3}$ , a beam radius of  $\sim 10 \text{ km}$ , and a process duration of  $\sim 1 \text{ ms}$  [Lehtinen *et al.*, 1997]. Note that the beam duration is of the same order as that in the source hemisphere, since the velocity dispersion of the relativistic particles during a single interhemispheric traverse is negligible. The beam density of  $10^5 \text{ m}^{-3}$  and duration of  $\sim 1 \text{ ms}$  represent the highest values consistent with observed terrestrial gamma ray flux intensities [Fishman *et al.*, 1994], with  $\sim 1 \text{ ms}$  also determined by the kinematics of the beam formation process [Lehtinen *et al.*, 1997; 1999]. The beam radius of  $\sim 10 \text{ km}$  is largely defined by the spatial configuration of the quasi-static field that drives the beam and is consistent with two-dimensional simulations of this process [Lehtinen *et al.*, 1997; 1999]. In our calculations below and based on the above discussion, we assume that 10% of the beam electrons are precipitated, i.e. the density of the precipitating beam is  $N_{\text{precip}} = 10^4 \text{ m}^{-3}$  and the total number of precipitating electrons is  $N_{\text{precip}}^{\text{tot}} = 3 \times 10^{17}$ . For reference purposes, the value  $N_{\text{precip}} = 10^4 \text{ m}^{-3}$  and the assumed thermal energy distribution correspond to a precipitation flux for  $>1 \text{ MeV}$  electrons of  $\sim 3 \times 10^8 \text{ cm}^{-2}\text{-s}^{-1}$ .

We now proceed to use the Monte Carlo method to simulate the interaction of the precipitating energetic electrons with the neutral atmosphere and determine the resultant optical emissions, secondary ionization and  $\gamma$ -rays. In addition to the processes described in Chapter 2, we also include the magnetic mirroring effect (see Appendix A).

We start our Monte Carlo calculations at an altitude of  $200 \text{ km}$ , with random initial electron momenta satisfying a thermal energy distribution and (6.3). We specify

the initial energy  $\mathcal{E}$  for a precipitating particle by the use of the cumulative distribution function  $X_{\mathcal{E}}(\mathcal{E})$  defined as

$$X_{\mathcal{E}}(\mathcal{E}) \equiv \frac{\int_0^{\mathcal{E}} f_{\mathcal{E}}^{\text{th}}(\mathcal{E}) d\mathcal{E}}{\int_0^{\infty} f_{\mathcal{E}}^{\text{th}}(\mathcal{E}) d\mathcal{E}}$$

and the fact that the random variable  $X_{\mathcal{E}}$  is uniformly distributed in the interval  $[0, 1]$ . The equation  $X_{\mathcal{E}}(\mathcal{E}) = X_{\mathcal{E}}$  is solved numerically for a randomly chosen  $X_{\mathcal{E}}$  to find the energy  $\mathcal{E}$ .

The random pitch angle of a downcoming particle is specified by inverting the cumulative distribution function  $X_{\alpha}(\alpha)$  defined as:

$$X_{\alpha}(\alpha) \equiv \int_0^{\alpha} \frac{F(\alpha')}{N_{\text{lc}}^{\text{tot}}} 2\pi \sin \alpha' d\alpha' = \frac{1 - \cos \alpha_{\text{eq}}}{1 - \cos \alpha_{\text{eq}}^{\text{lc}}}$$

The random variable  $X_{\alpha}$  is uniformly distributed in the interval  $[0, 1]$ . The random pitch angle is obtained in terms of  $X_{\alpha}$  as

$$\alpha = \sin^{-1} \left[ \sqrt{\frac{B}{B_{\text{eq}}} \left\{ 1 - \left[ 1 - X_{\alpha} \left( 1 - \sqrt{1 - \frac{B_{\text{eq}}}{B}} \right) \right]^2 \right\}} \right]$$

The Monte Carlo method allows us to accurately estimate the evolution of the electron distribution function which in turn is used to estimate the optical emissions, ionization and  $\gamma$ -rays. Most of the downcoming electrons are deposited, although a small fraction ( $\sim 12\%$ ) are found to be backscattered. The backscattered electrons are in the loss cone and by the very fact that they are already near or below the mirror altitude also precipitate after several bounces.

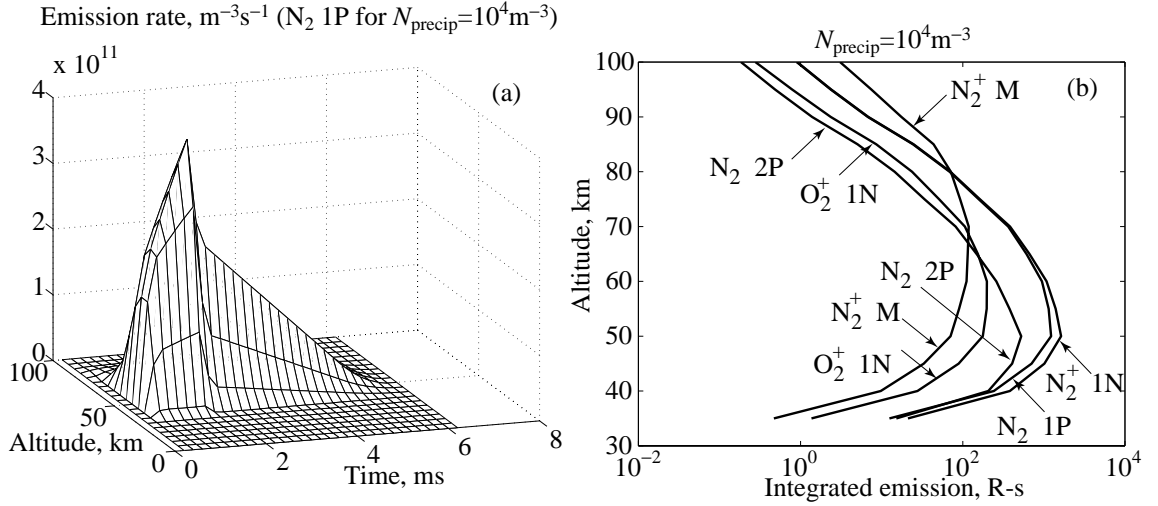


Figure 6.1: **Optical emissions in the conjugate region.** The optical emissions due to precipitation of runaway electrons in the conjugate hemisphere: (a) the emission rate of First Positive  $N_2$  band, (b) time-integrated emissions in molecular bands. The precipitating electron flux was taken to have a density of  $N_{precip} \simeq 10^4 m^{-3}$ , lasting for 1 ms, corresponding to the initial runaway electron density of  $N_R = 10^5 m^{-3}$

## 6.2 Optical Emissions

The calculated altitude profiles for the five molecular bands enumerated in Section 3.1 are presented in Figure 6.1. Figure 6.1a shows the altitude and time dependence of the photon production rate in the first positive band of  $N_2$ . Figure 6.1b shows the time-integrated optical emission intensities in the five molecular bands, converted to Rayleigh-seconds. The optical emission intensity in Rayleighs is given as

$$I = 10^{-10} \int \varepsilon dl \simeq \varepsilon d,$$

where the integration is along the line of sight,  $\varepsilon$  is the volume emission rate in  $m^{-3}s^{-1}$ , and  $d \simeq 2 \times 10^4 m$  is the transverse size of the beam.



The optical emission intensities shown in Figure 6.1 are easily detectable by standard imaging and photometric instruments in terms of brightness levels. However, the emissions last only for a few ms, so that high frame rate photometric imaging would be needed. Also, the transverse extent of the beam is only  $\sim 20$  km, so that accurate pointing or very wide aperture (e.g., all-sky cameras) instruments would need to be used.

The optical emissions produced by the precipitating component of the relativistic electron beam which is caused by a lightning flash in the conjugate hemisphere may be loosely termed to be “conjugate sprites”, to be distinguished from sprites produced in the hemisphere of the causative flash by quasi-electrostatic heating of ambient electrons. It is interesting to note that the excitation intensities of the two primary emissions in Figure 6.1b  $N_2$  1P (red) and  $N_2^+$  1N (blue) are similar, so that these “conjugate sprites” are not predominantly red as their counterparts produced overhead thunderstorms [Mende *et al.*, 1995]. The combination of the red and blue colors would lead to a sprite which exhibits purple color. For ground-based observations of the the optical emissions one should also take into account the relatively greater attenuation of blue than red in the atmosphere due to Rayleigh scattering.

### 6.3 Secondary Ionization

The secondary electron production rate is calculated directly from the energy deposition rate by assuming that every deposited 35 eV energy creates an electron-ion pair [Rees, 1963]. The time dependence of electron density  $N_e$  due to chemical reactions in the atmosphere is calculated using the model of Glukhov *et al.* [1992]. This model accounts for the dynamics of three other charged atmospheric constituents, namely the

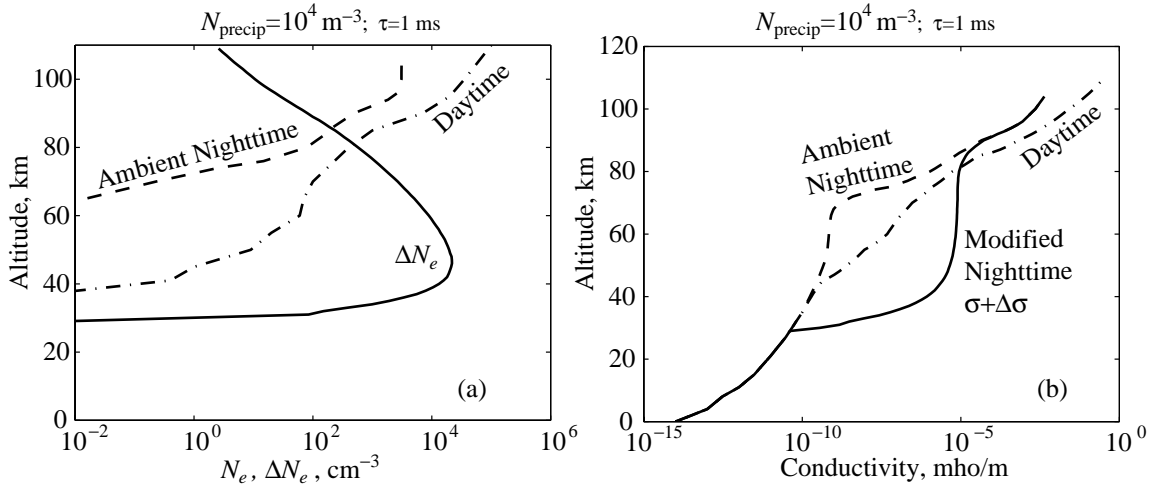


Figure 6.2: **Conjugate ionization and conductivity enhancement.** The precipitating runaway electrons in the conjugate hemisphere produce ionization and conductivity shown here in the initial time moment as a function of altitude.

density of positive and negative ions and positive cluster ions. We make the following corrections to the coefficients of equations (1) through (4) of *Glukhov et al.* [1992]. The effective coefficient of dissociative recombination (denoted  $\alpha_d$  by *Glukhov et al.* [1992]) is taken to be equal to  $6 \times 10^{-7} \text{ cm}^3 \text{ s}^{-1}$ , according to the value in [*Rodriguez and Inan, 1994*], and the effective electron detachment rate (denoted  $\gamma$  by *Glukhov et al.* [1992]) is  $3 \times 10^{-18} N_m \text{ s}^{-1}$ , where  $N_m$  is the total density of neutrals, according to *Pasko and Inan* [1994]. The value of the effective electron detachment rate is estimated by *Glukhov et al.* [1992] using the ratio  $N_0^-/N_{e0}$  of the ambient negative ion and electron densities. The experimentally measured value, quoted by *Glukhov et al.* [1992] is  $N_0^-/N_{e0} \sim 1$  at the altitude of  $\sim 80 \text{ km}$ , which gives the effective electron detachment rate of  $3 \times 10^{-17} N_m \text{ s}^{-1}$ . Neglecting this coefficient altogether would give  $N_0^-/N_{e0} \simeq 10^2$  at altitude  $\sim 80 \text{ km}$ , which is greater by two orders of magnitude. The value  $N_0^-/N_{e0} = 1$  in the case of no electron detachment is attained at  $\sim 92 \text{ km}$ .

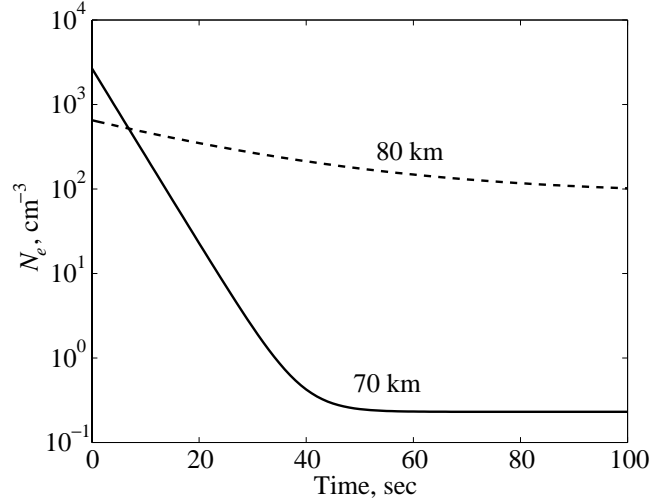


Figure 6.3: **Time evolution of ionization.** The ionization produced by precipitating electrons is shown as a function of time at altitudes 70 and 80 km.

Knowing the change of electron density level, we can estimate the change of ionosphere conductivity at different altitudes. The total parallel conductivity [see equation(4.3)] is  $\sigma_0 = \sigma_i + \sigma_e$ , where  $\sigma_i$  is the ambient ion conductivity and  $\sigma_e$  is the electron conductivity which is changed by the precipitation. The ion conductivity is derived from total ambient conductivity in [Hale, 1994] by subtracting the electron part. For electrons, we have  $\sigma_e = q_e N_e \mu$ , where  $\mu = 3.66 \times 10^{25}/N_m$  is the electron mobility [Davies, 1983], with  $N_m$  in  $\text{m}^{-3}$  and  $\mu$  in  $\text{m}^2\text{-V}^{-1}\text{-s}^{-1}$ .

The initial ionization enhancement and conductivity are plotted in Figure 6.2, and the calculated time dependence of the electron density at altitudes of 70 and 80 km is plotted in Figure 6.3. The electron density and associated conductivity changes shown in Figure 6.2 are detectable by means of subionospheric VLF remote sensing, in spite of the relatively small  $\sim 20$  km lateral extent of the ionospheric disturbance. As a crude assessment of this detectability, we consider equation (1) of Inan *et al.* [1985], according to which the phase change  $\Delta\phi$  of a 20 kHz subionospheric signal

due to a reflection height change  $\Delta h$  over a length  $D$  of a long ( $>2000$  km) VLF propagation path is given by

$$[\Delta\phi]_{\text{deg}} \simeq -0.0034 [d]_{\text{km}} [\Delta h]_{\text{km}}, \quad (6.4)$$

where we have assumed an ambient (unperturbed) VLF reflection height of  $\sim 85$  km. To determine  $\Delta h$  corresponding to the modified electron density profile given in Figure 6.2a, we can consider the fact that VLF reflection typically occurs when  $(\omega^2/\nu) \simeq 2.5 \times 10^5 \text{ s}^{-1}$ , where  $\omega_p$  and  $\nu$  are respectively the local plasma and effective electron collision frequency. Applying this criterion on the ambient and disturbed profiles of Figure 6.2a, we find the ambient reflection height to be  $\sim 85$  km, and  $\Delta h \simeq -2.5$  km. Using this value and  $d \simeq 20$  km in (6.4) we find  $\Delta\phi \simeq 0.17^\circ$ , which is detectable [Wolf and Inan, 1990].

Equation (6.4) is in fact only valid for relatively small perturbations near the VLF nighttime reflection height of  $\sim 85$  km [Inan *et al.*, 1985]. It is clear from Figure 6.2 that the conductivity changes produced by the precipitating energetic electrons are large (i.e.,  $\Delta N \gg N_{e0}$ ) and occur over a very broad range of altitudes. The range of VLF amplitude and phase changes that would be produced by such a disturbance was estimated using the Long Wave Propagation Capability (LWPC) code which is available at Stanford and which has in the past been used to quantify VLF signatures of lightning-induced electron precipitation bursts [Lev-Tov *et al.*, 1996, and references therein]. Calculations indicate that the sudden appearance of a disturbance of lateral extent  $\sim 20$  km and with a disturbed conductivity profile as given in Figure 6.2b on a relatively long (a few thousand km) subionospheric path leads to amplitude changes of several dB and phase changes of several degrees, depending on the location of the receiver.

## 6.4 $\gamma$ -ray Emissions

Energetic precipitating electrons produce  $\gamma$ -rays through the process of bremsstrahlung described in Chapter 3. The bremsstrahlung photons are emitted by the downward going relativistic electrons predominantly in the forward direction, as given by the angular distribution (3.12). The downward photons cannot penetrate the atmosphere, and are not detectable on the ground, but are strongly scattered by the increasing dense atmosphere which constitutes an optically ‘thick’ target. The scattered photons which move upward can be detected by a satellite. In Chapter 4, in which we considered the case of  $\gamma$ -rays emitted at  $\sim 60$ – $70$  km altitude and in the upward direction toward an increasingly tenuous (i.e., ‘thin’ target) atmosphere so that the photon transport to satellite altitudes was straightforward. For the case in hand, we need to consider multiple scattering of the  $\gamma$ -ray photons and use a Monte Carlo model [Seltzer and Berger, 1974] to quantify this process. The Monte Carlo model uses processes described in Section 3.2 and the implementation details are given in Appendix A.

The processes which determine the photon propagation are the Compton scattering and photoeffect. These processes and their cross-sections are given in Chapter 3. The results of the Monte Carlo simulation are presented in Figure 6.4. The predicted spectrum is hard for  $\mathcal{E}_{\text{ph}} < 100$  keV and soft for  $\mathcal{E}_{\text{ph}} > 100$  keV, as a result of low-energy photons being attenuated due to photoeffect. The maximum photon flux (in the range  $\mathcal{E}_{\text{ph}} > 5$  keV) at the satellite altitude for our value of precipitating electron flux ( $N_{\text{precip}} = 10^4 \text{ m}^{-3}$ , which corresponds to energy flux of  $\sim 10^3 \text{ erg-cm}^{-2}\text{-s}^{-1}$ , precipitating over area of  $100 \text{ km}^2$ ) is  $\sim 10^7 \text{ ph-m}^{-2}\text{-s}^{-1}$ . For comparison, the minimum flux detectable by the BATSE satellite on CGRO is  $\sim 10^4 \text{ ph-m}^{-2}\text{-s}^{-1}$ . As shown in Figure 6.4c, the upgoing photon beam produced by the precipitating electrons in the

conjugate hemisphere is also broader than the one produced by the upgoing runaway beam in the hemisphere of the causative lightning (Figure 4.3). The more effective emission of photons is due to the fact that downgoing electrons deposit all of their energy in the atmosphere which essentially constitutes a thick target while the upgoing ones interact with atmosphere at high altitudes, where it is a thin target.

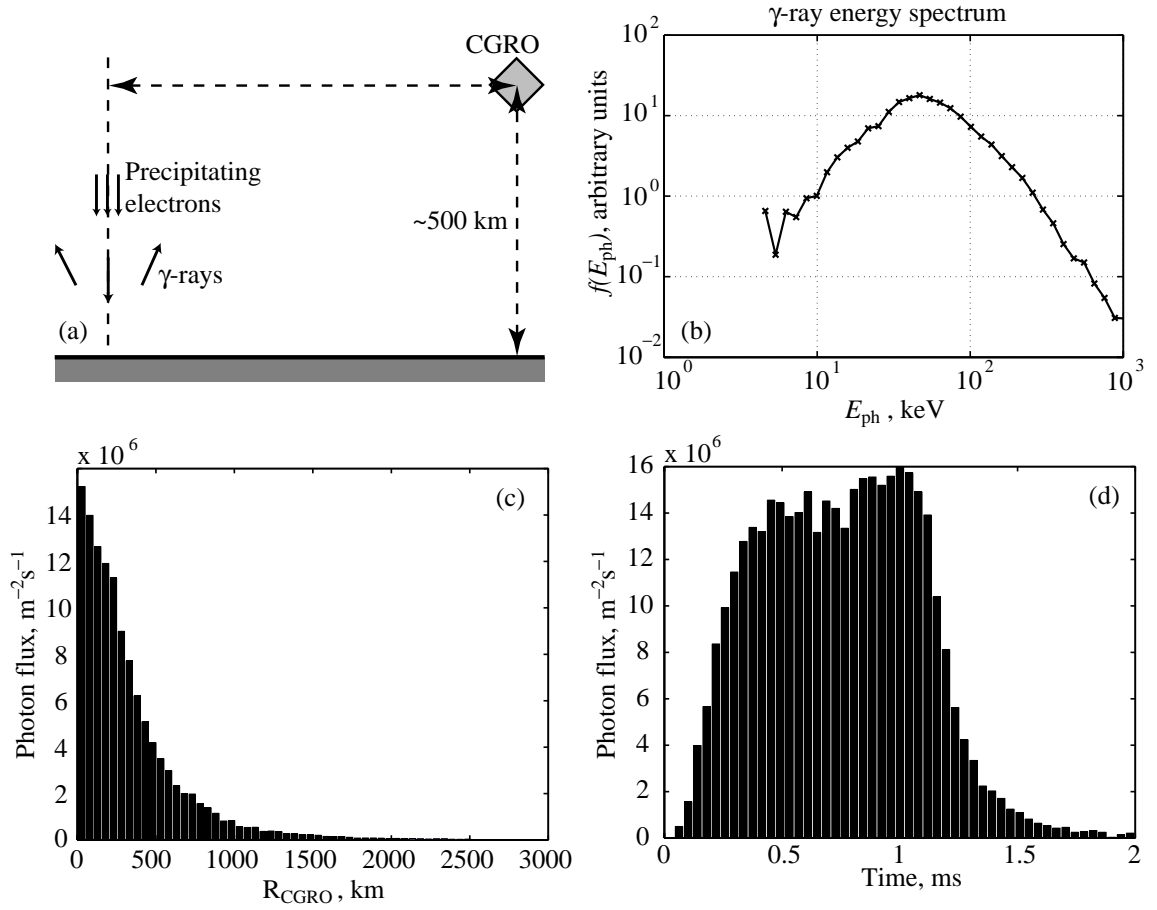


Figure 6.4: **Gamma rays emitted by precipitating electrons.** (a) cartoon depicting the detection of photons by the satellite; (b)  $\gamma$ -photon energy spectrum; (c) the radial distribution of gamma rays; (d) the temporal structure directly above the precipitation point, assuming the a square pulse of precipitating electrons with duration of 1 ms.

# Chapter 7

## Conclusions and Future Work

### 7.1 Conclusions

We have developed a Monte Carlo model of the highly nonlinear fundamental physical process of relativistic runaway avalanche breakdown in collisional air. This model allowed the first quantitative determination of the avalanche rate and the time evolution of the momentum space distribution for this process in the presence of an arbitrarily directed magnetic field.

The Monte Carlo runaway avalanche model results were applied to simulate the runaway breakdown caused by a positive lightning discharge in a mesoscale convective thunderstorm system. We considered a fluid model of the avalanche in two different cases. The first case described a laterally extensive thundercloud using a Cartesian (translationally symmetric) model. The second case dealt with a cylindrically symmetric model with a vertical axis of symmetry, constrained to have a vertical geomagnetic field. In both cases, the transport equation for the electrons was integrated using a lookup table of avalanche velocities and rates calculated with the Monte Carlo



model. Based on our results, we concluded that the geomagnetic field must be accounted for in describing the motion of runaway electrons at midlatitudes, where most sprites have been observed. The geomagnetic field significantly deflects the runaway beam from the vertical, so that the frequently observed vertical columnar structure of sprite is an indication that the observed luminosity is not produced by the runaway electrons as has been previously suggested [*Taranenko and Roussel-Dupré, 1996*]. At latitudes close to the geomagnetic equatorial region, where terrestrial  $\gamma$ -ray flashes have been detected, the  $\gamma$ -ray beam, which is emitted parallel to the electron beam, is thus also emitted not along the vertical but along the geomagnetic field. At the geomagnetic equator, the horizontal geomagnetic field is perpendicular to the vertical thunderstorm electric field and can prevent the development of relativistic electron avalanche at altitudes  $\gtrsim 40$  km.

The optical emissions associated with relativistic electrons are found to be not of significant intensity compared to emissions caused by conventional type of ionization breakdown. For discharges involving the removal of sufficiently large values of total charge, the  $\gamma$ -ray fluxes, which are produced by bremsstrahlung from the runaway electron beam, are found to be consistent with experimental data [*Fishman et al., 1994; Nemiroff et al., 1997*].

In general, the observable physical effects of runaway electrons in the upper atmosphere are found to be less intense than in [*Lehtinen et al., 1997*], due to lower calculated avalanche rates than in [*Roussel-Dupré et al., 1994*], although the electric field configuration is determined by the same conductivity profile. *Yukhimuk et al., [1999]* use new avalanche rates calculated by *Symbalisty et al. [1998]*, which nevertheless are still larger than those obtained in our Monte Carlo model, as discussed in Chapter 2, as well as use an electric field model which assumes no conductivity

below 20 km. The electric field in these models has much higher values at altitudes at which the runaway electron avalanche occurs. All of these factors combine to lead to lower runaway electron effects in our model than those obtained by *Yukhimuk et al.* [1999].

We considered the fate of energetic runaway beams driven upward by intense thundercloud fields produced by large positive cloud-to-ground discharges. Based on the velocity space distribution function of such beams as determined by Monte Carlo methods [*Lehtinen et al.*, 1999], we have determined that the runaway electron beam intensely interacts with the background magnetospheric plasma, leading to rapid nonlinear growth of Langmuir waves and pitch angle and energy scattering of the beam electrons. The end result of this interaction is the isotropization and thermalization of the electron distribution function, leading to the trapping of most of the beam electrons in the radiation belts, and the formation of detectable trapped electron curtains.

Although the beam may be largely thermalized and isotropized [*Lehtinen et al.*, 2000a] during its traverse between hemispheres, the particle flux which arrives in the conjugate hemisphere below the loss cone precipitates into the atmosphere, producing optical emissions and secondary ionization.

Monte Carlo modeling of the interaction of the downcoming beam with the atmosphere indicates that for typical beam current densities (calibrated by measured intensities of bremsstrahlung gamma rays) emissions in different optical bands, including the first and second positive bands of molecular nitrogen, and the first negative band of  $N_2^+$  are excited at levels detectable with properly pointed instruments having sufficient time resolution. In this context, it is important to note that the temporal duration of the emissions is  $\sim 1$  ms, and that the lateral extent of the beam is  $\sim 20$  km.

Monte Carlo modeling further indicates that the secondary ionization produced by the precipitating energetic beam electrons is significant, leading to electron density enhancements up to  $\sim 100 \text{ cm}^{-3}$  over the range of altitudes of 35 to 85 km. The resultant conductivity changes are sufficiently large to produce detectable amplitude and phase changes of subionospheric VLF signals propagating underneath, in spite of the relatively small lateral extent of the secondary ionization disturbance. The  $\gamma$ -ray emissions from the precipitating energetic electrons can also be detectable by the BATSE detectors on the CGRO satellite [Fishman *et al.*, 1994].

Future experiments aimed at detection of the effects of the runaway electron beams in the conjugate region may provide definitive experimental evidence of the runaway acceleration mechanism, but need to be carefully conducted in view of the short duration of the optical emissions and small lateral extent of the ionization disturbances.

## 7.2 Suggestions for Future Work

The Monte Carlo modelling of atomic processes has several advantages over numerical solution of a kinetic equation: (1) it is easily implemented in three dimensions without the considerable increase in computer memory use which occurs when the kinetic equation is generalized from two to three dimensions; (2) one does not have to worry about numerical stability; (3) complicated collision processes are easier to implement. Therefore, the Monte Carlo model can be generalized to include electrons with low energies and low-energy processes of electron interaction with the background material, such as excitation of particular rotational, vibrational and electronic levels of air molecules. This can be applied to model non-relativistic discharges in gases. The possibility to generalize to many dimensions gives an opportunity to model a discharge

not only in the momentum space, but also in the configuration space, thereby taking into account nonhomogeneity of the electric field and of the background medium.

The modelling of the nonlinear interaction of the relativistic runaway electron beam with the ambient plasma in the magnetosphere was beyond the scope of this work. It is, however, an interesting problem by itself. The solution of it can include complicated multidimensional plasma simulations [*Birdsall and Langdon, 1991*], which properly include the nonhomogeneity of the beam.

The source of the seed runaway electrons is assumed to be a uniform constant flux of cosmic rays. The variability of the cosmic ray flux due to solar cycles and statistical variations was not taken into account. This variability should be studied as it may indicate a variability of production of runaway beams and terrestrial  $\gamma$  flashes by otherwise identical thundercloud discharges. The other possible source of relativistic electrons could be the streamers, as indicated by the presence of x-rays in experimental studies of spark discharges [*Tarasova et al., 1974, Babich, 1982, and references therein*]. This source should also be studied, because there is an evidence of the presence of streamers above thunderclouds [*Pasko et al., 1998b*].

# Appendix A

## Monte Carlo Model Details

The general principles of Monte Carlo modelling can be found in [Berger, 1963]. In this Appendix we describe computational methods and procedures used in our Monte Carlo model of electron avalanche and (in the last Section) the  $\gamma$ -photon propagation. Other similar modern programs exist and are referenced in literature [Nelson *et al.*, 1985; Atwood *et al.*, 1992].

### A.1 Dimensionless Units

Instead of usual molecular air density  $N_m$  the program uses dimensionless  $N_{m,d}$  which is normalized to conversion factor  $N_m^{\text{conv}}$  defined so that  $2\pi N_m^{\text{conv}} Z_m r_0^2 c = 1 \text{ s}^{-1}$ . The electric field is measured in inverse seconds. At  $N_m^{\text{conv}}$  the runaway threshold field  $E_t$  is equal to  $21.7321 \text{ s}^{-1}$ . To convert SI units to inverse seconds is to multiply the field in  $\text{V}\cdot\text{m}^{-1}$  by  $q_e/(mc) = 586.679 \text{ V}^{-1}\cdot\text{m}\cdot\text{s}^{-1}$ . The magnetic field is also measured in inverse seconds. The physical meaning of  $B$  in inverse seconds is the gyrofrequency. To convert from Teslas to inverse seconds we multiply by  $q_e/m = 1.75882 \times 10^{11} \text{ T}^{-1}\cdot\text{s}^{-1}$ .

## A.2 Diffusion: Choice of Angle

The probability distribution function  $f(\mu, t)$  of the angular deflection  $\Delta\Theta$  (where  $\cos \Delta\Theta = \mu$ ) after multiple collisions satisfies the diffusion equation which involves the diffusion coefficient  $D(p)$ :

$$\frac{\partial f}{\partial t} = D \frac{\partial}{\partial \mu} \left\{ (1 - \mu^2) \frac{\partial f}{\partial \mu} \right\}.$$

The diffusion coefficient is connected with the time rate of change of the mean square angle:

$$D(p) = \frac{1}{4} \frac{d\langle \Theta^2 \rangle}{dt}$$

The solution to the diffusion equation is given by equation (2.9):

$$f(\mu, \tau) = \sum_{n=0}^{\infty} \left( n + \frac{1}{2} \right) P_n(\mu) e^{-n(n+1)\tau},$$

where  $P_n$  are Legendre polynomials, and  $\tau \equiv Dt$  is dimensionless time.

This series is convergent, and for given  $\tau$  we can neglect the terms with  $n(n+1)\tau \gg 1$ , which translates into  $n \gg 2/\Delta\Theta$ . For  $\tau \ll 1$  we see that  $n$  has to be large, making this solution ineffective. But if we assume small angles  $\Delta\Theta \ll 1$ , we have  $\mu = 1 - \xi$ , where  $\xi \ll 1$ , and  $1 - \mu^2 \simeq 2\xi$ . We can rewrite the diffusion equation in form:

$$\frac{\partial f}{\partial \tau} = 2 \frac{\partial}{\partial \xi} \left\{ \xi \frac{\partial f}{\partial \xi} \right\}$$

Noting that the solution of this equation is  $f(\xi, \tau) = e^{\xi/(2\tau)}/(2\tau)$ , we use a solution

which is properly normalized:

$$f_1(\mu, \tau) \simeq \frac{e^{-(1-\mu)/(2\tau)}}{2\tau(1 - e^{-1/\tau})}$$

The random number  $\mu$  can be found from the cumulative distribution  $X = \int_{-1}^{\mu} f(\mu') d\mu' \in [0, 1]$ , which is a uniformly distributed random variable:

$$\mu_1(X) = 2\tau \ln[(e^{1/(2\tau)} - e^{-1/(2\tau)})X + e^{-1/(2\tau)}] \quad (\text{A.1})$$

For  $\tau \sim 1$  or greater in the series solution (2.9) we take into account only the terms  $n = 0, 1$ :

$$f_2(\mu, \tau) = \frac{1}{2} + \frac{3}{2}\mu e^{-2\tau}.$$

which is normalized to unity in the same manner as  $f_1(\mu, \tau)$ . Once again, from the cumulative distribution  $X \in [0, 1]$  we find

$$\mu_2(X) = \frac{1}{3} \left[ -e^{2\tau} + \sqrt{9 - 6e^{2\tau} + e^{4\tau} + 12Xe^{2\tau}} \right]$$

For large  $\tau$ , subtracting two near-equal numbers in the last formula can lead to loss of precision or even to an error. In this case, we expand the square root in series

$$\sqrt{1 + \epsilon} \approx 1 + \frac{1}{2}\epsilon - \frac{1}{8}\epsilon^2; \quad \epsilon \ll 1$$

and get approximately (neglecting terms  $\sim e^{-4\tau}$ )

$$\mu_2(X) = 2X - 1 + 6X(1 - X)e^{-2\tau}$$

To minimize the error, we use solution  $\mu_1$  for  $\tau < 0.5$  and  $\mu_2$  for  $\tau > 0.5$ .

For extremely small scattering angle  $\Delta\Theta$ , solution  $\mu_1$  is not well suited for computation because in (A.1) we have  $1/(2\tau) \gg 1$  and an exponential of a large number is taken. In such cases we take a fixed  $\Delta\Theta$  [Risken, 1989, p. 60]:

$$\Delta\Theta \equiv \sqrt{\langle\Theta^2\rangle} = \sqrt{\frac{d\langle\Theta^2\rangle}{dt}} \Delta t.$$

### A.3 Choice of $\Delta t$

First, the time interval  $\Delta t_0$  is chosen to be appropriate for the numerical solution of the differential equation describing the electron motion. We then let

$$\Delta t = \alpha \min(\Delta t_0, \tau_{\text{ion}})$$

where  $0 < \alpha < 1$  and  $\tau_{\text{ion}}$  is average time until the next ionizing collision. Smaller  $\alpha$  leads to greater numerical accuracy, but increases the computer time. Trial calculations showed that  $\alpha$  has to be  $\sim 0.05$  or less. The ionization probability at the end of a given time step is then  $\Delta t/\tau_{\text{ion}}$  (assured by the method of its computation to be  $< 1$ ).

Another way to quantify the process of ionizing collisions was implemented to insure a greater accuracy for larger  $\Delta t$ , so that the factor  $\alpha$  does not have to be too small to be adequate, thus reducing computation time. In this method, we compare  $\alpha\Delta t$  with the ‘dynamic’ value of the time step

$$\Delta t_d = -\tau_{\text{ion}} \log X$$



where  $X \in [0, 1]$  is a uniformly distributed random number [Fano *et al.*, 1959]. We choose  $\min(\Delta t, \Delta t_d)$  for the correct time step. If  $\Delta t < \Delta t_d$ , ionization does not occur. If  $\Delta t > \Delta t_d$ , there is no ionization.

## A.4 Magnetic Mirror Effect

The magnetic mirror effect must be taken into consideration in the Monte Carlo code, since some of the electrons interacting with the atmosphere are incident at grazing angles, with local pitch angles near  $90^\circ$ . The change in the electron momentum due to a nonuniform magnetic field is described by the following equations:

$$\frac{dp_{\parallel}}{dt} = -v_{\perp} \frac{p_{\perp} \nabla_{\parallel} B}{2B} \quad (\text{A.2a})$$

$$\frac{dp_{\perp}}{dt} = v_{\parallel} \frac{p_{\perp} \nabla_{\parallel} B}{2B} \quad (\text{A.2b})$$

We therefore need to determine an expression for the quantity  $\nabla_{\parallel} B/(2B)$  in order to advance the particle momentum components in time. For the dipole approximation of the Earth's magnetic field the components are given by

$$\begin{aligned} B_r &= -2B_0 \sin \lambda \left( \frac{R_0}{R} \right)^3 \\ B_{\theta} &= B_0 \cos \lambda \left( \frac{R_0}{R} \right)^3 \end{aligned}$$

where  $\lambda$  is the geomagnetic latitude,  $B_0$  is the magnetic field at the geomagnetic equator at the Earth's surface,  $R_0$  is the Earth's radius. We have the magnetic line equation

$$R(\lambda) = LR_0 \cos^2 \lambda$$

where  $L$  is the  $L$ -shell number, related to the latitude  $\lambda_0$  at which the magnetic field line intersects the Earth's surface by  $L \cos^2 \lambda_0 = 1$ . The magnetic field on the field line is

$$B(\lambda) = B_0 \left( \frac{R_0}{R} \right)^3 \sqrt{1 + 3 \sin^2 \lambda} = B_{\text{eq}} \frac{\sqrt{1 + 3 \sin^2 \lambda}}{\cos^6 \lambda}$$

where  $B_{\text{eq}} = B_0/L^3$  is the field at the geomagnetic equator. Using the magnetic field line element

$$dl = \sqrt{(dR/d\lambda)^2 + R^2} d\lambda = LR_0 \cos \lambda \sqrt{1 + 3 \sin^2 \lambda} d\lambda$$

and

$$\frac{dB}{d\lambda} = \frac{B_0}{L^3} \frac{3 \sin \lambda (3 + 5 \sin^2 \lambda)}{\cos^7 \lambda \sqrt{1 + 3 \sin^2 \lambda}}$$

we find

$$\nabla_{\parallel} B = \frac{dB}{dl} = \frac{dB}{d\lambda} \frac{d\lambda}{dl} = \frac{B_0}{R_0} \left( \frac{R_0}{R} \right)^4 \frac{3 \sin \lambda (3 + 5 \sin^2 \lambda)}{1 + 3 \sin^2 \lambda}$$

At the surface of the Earth,  $R = R_0$ ,  $\lambda = \lambda_0$ , we have

$$\begin{aligned} \nabla_{\parallel} B &= \frac{B_0}{R_0} \frac{3 \sin \lambda_0 (3 + 5 \sin^2 \lambda_0)}{1 + 3 \sin^2 \lambda_0} \\ \frac{\nabla_{\parallel} B}{2B} &= \frac{1}{R_0} \frac{3 \sin \lambda_0 (3 + 5 \sin^2 \lambda_0)}{2(1 + 3 \sin^2 \lambda_0)^{3/2}} \end{aligned}$$

Substituting  $R_0 \simeq 6378$  km,  $\lambda = 45^\circ$ , we find

$$\frac{\nabla_{\parallel} B}{2B} \simeq 2.31 \times 10^{-4} \text{ km}^{-1}$$

With the normalized parallel gradient of  $B$  determined as above, the electron momentum changes at each step are determined from (A.2).

## A.5 Implementation of the Particle Set

The changing set of particles in the Monte Carlo simulation is implemented in three different ways:

### A.5.1 Null-Collision Method

This method was used in the previous studies of the runaway process [*Lehtinen et al.*, 1999]. In this method, all particles in the set under consideration have the same time step  $\Delta t$ , which is chosen to be much smaller than minimum time between collisions of the particles [*Lin and Bardsley*, 1977; *Tzeng and Kunhardt*, 1986]. The advantage of this method is that it can be generalized to include the self-consistent field of the particles themselves (‘particle-in-cell’ methods, see [*Birdsall and Langdon*, 1991]). The disadvantage is that due to smallness of  $\Delta t$  it can be computationally inefficient. During most of the steps the particle do not experience ionizing collisions (null-collision steps). This method is implemented by the way of an abstract storage data type, which allows for easy addition of particles to it, iterate over stored particles, and remove a particle to which the iterator is pointing at the given moment. All newly added particles are not iterated over in the same cycle in which they were created. In this way, each iteration is associated with a time step. Thus, the iteration is done in a time cycle, with ‘global’ time increased by  $\Delta t$  at the end of each iteration. The addition of particles is associated with ionization, while the removal is associated with thermalization.

### A.5.2 Stacked-Particle Method

This method is widely used in high-energy physics, for example in EGS4 model and its successors [Nelson *et al.*, 1985; Atwood *et al.*, 1992]. In this method, the particles are stored in a stack, and only the particle at the top of the stack is considered at a given time. If a particle is created, it is pushed onto the stack and becomes a new current particle. If the particle is removed from consideration, it gets popped off the stack, and the particle beneath it becomes the new current particle. Each particle in the stack has its own ‘proper’ time. In this method, the null-collision steps can be eliminated, and the method can become more computationally effective. Since each particle is considered separately, it is difficult to incorporate the self-consistent fields. However, according to previous modelling [Lehtinen *et al.*, 1999] the space charge of runaway electrons is small and does not influence their motion, so that this problem does not arise in the context of physical processes considered in this dissertation. Another problem is that if the particle avalanche rate is not known, and an incorrect (too large) estimate of the final time is made, the computation might overflow the computer memory allocated to store the particle information at the final time, due to the huge number of particles (which was underestimated). With the null-collision method, such problems can be caught when the particle number is greater than some initially given value. In the stacked-particle method, it is not easy to notice such a build-up of the number of particles, because the ‘proper’ times of the particles in the stack are widely different.

### A.5.3 Optimized Null-Collision Method

In this algorithm, the particles are still iterated over the storage in a cycle, but unlike the null-collision method, this is not a time cycle. Each particle has its individual ‘proper’ time, and the cycle continues until the time for all particles is expired (the particles whose ‘proper’ time is greater than the final time of computation are removed from the storage). This method requires the same computer time as the stacked-particle method, and has almost no additional advantages compared to it. The quasi-simultaneity of particles in the storage might be more advantageous in tackling problems such as unexpected build-up of the number of particles.

## A.6 Photon Monte Carlo Calculations

The photon Monte Carlo modelling is simpler than the electron modelling because there are no frequent small-angle or small-energy-loss photon collisions. The model utilizes expressions for the Compton scattering and photoeffect cross sections given in Chapter 3.

### A.6.1 Calculation of the Time of the Next Collision

Initial and final locations of the particle are denoted as  $\mathbf{r}_0$ , and  $\mathbf{r}_1$ . The time of the next collision is calculated as follows. We first calculate the thickness  $d = \int_0^{\Delta r} N_m dr$  along the photon path between collisions, using the cumulative probability method [Fano *et al.*, 1959], where

$$d = -\frac{1}{\sigma_C^{\text{tot}} + \sigma_P} \log X$$

and where  $X \in [0, 1]$  is a uniformly distributed random variable.

We then define the atmospheric content above altitude  $z$ :

$$D(z) = \int_z^\infty N_m(z) dz$$

For the final particle location, we find  $D(z_1) = D(z_0) - d \cos \theta$ , from where we can find  $z_1$ . Other coordinates are found from the fact that  $\Delta \mathbf{r}$  is along photon velocity and are calculated using known  $\Delta z = z_1 - z_0$ . The time step is then found from  $\Delta t = \Delta r / c$ .

The type of the next collision (Compton scattering or photoelectric absorption) is determined by considering another uniformly distributed random variable  $X' \in [0, 1]$ . If  $X' < \sigma_P / (\sigma_C^{\text{tot}} + \sigma_P)$ , then the next collision is the photoelectric absorption, otherwise, it is Compton scattering.

### A.6.2 Compton Scattering

The Compton scattering is described by the Klein-Nishina cross section (3.15), from which the resultant energy of the scattered photon can be found to be given approximately by

$$\gamma' = \frac{\gamma}{1 + sX + (2\gamma - s)X^3}; \quad s = \frac{\gamma}{1 + 0.5625\gamma}$$

where  $X \in [0, 1]$  is a uniformly distributed random variable, with  $\gamma = \mathcal{E} / mc^2 = p / mc$  normalized to the electron rest energy. This is a corrected formula from [Pilkington and Anger, 1971], so that the new energy  $\gamma'$  lies in the correct interval  $[\gamma / (1 + 2\gamma), \gamma]$ . The error compared to Klein-Nishina formula is  $< 17\%$  in all cases.

The direction of scattering is uniformly random in azimuthal angle. The scattering angle is determined from the energy-momentum conservation condition [Heitler, 1954,

p. 211]:

$$\theta = \arccos \left( 1 + \frac{1}{\gamma} - \frac{1}{\gamma'} \right)$$

### A.6.3 Photon Energy Deposition

The energy deposition for  $\gamma$ -rays is important when they are the only source of ionization, such as the case when they originate from an astrophysical source [*Inan et al.*, 1999]. In the calculations for this work, the photons are a result of bremsstrahlung by electrons, which produce much more ionization so that the small additional ionization produced by the bremsstrahlung photons can be neglected. However, for the sake of completeness, we present here the algorithm used for the calculation of the energy deposition by photons, which was employed by *Inan et al.* [1999]. According to [*Brown*, 1973], all energy lost by a photon to a Compton or photo-electron is deposited within 1 km from the point of its collision, and we assume that all of this energy goes to ionization. According to [*Rees*, 1963], the average energy portion that goes into creation of an ion-electron pair in atmosphere is 35 eV. When the photon is Compton-scattered, part of its energy which is taken by the electron is assumed to be deposited at the point of collision. In the photoeffect, all photon energy is deposited. Also, when the photon energy becomes smaller than the minimum photon energy considered, then all its energy is assumed to be deposited at the end point of the last step.

# Appendix B

## Kinetic Equation

Most previous models of runaway avalanche [*Roussel-Dupré et al.*, 1994; *Bulanov et al.*, 1997; *Symbalist et al.*, 1998] are based on the equation for the electron momentum distribution function  $f(\mathbf{p})$ , i.e., the kinetic (Boltzmann) equation for a uniform avalanche ( $\nabla_{\mathbf{r}} \equiv 0$ ). Since most collisions change the runaway electron momenta stochastically by a small value, the Boltzmann collision integral is in fact of the Fokker-Planck type.

The Fokker-Planck equation [e.g., *Risken*, 1989] of a species that are subject to an external force  $\mathbf{F}_{\text{ext}}$ , which experience random change of momentum, and which have a source creating (or destroying) particles  $S(\mathbf{p})$ , is written as

$$\frac{\partial f(\mathbf{p})}{\partial t} = -\nabla_{\mathbf{p}}[(\mathbf{F}_{\text{ext}} + \mathbf{F}_D)f(\mathbf{p})] + \nabla_{\mathbf{p}}[\vec{D}\nabla_{\mathbf{p}}f(\mathbf{p})] + S(\mathbf{p}) \quad (\text{B.1})$$

where  $\mathbf{F}_D$  is the dynamic friction coefficient, or stopping power, whose components are *defined* as:

$$(\mathbf{F}_D)_i \equiv \lim_{\Delta t \rightarrow 0} \left( -\frac{\langle \Delta p_i \rangle}{\Delta t} \right)$$



where  $i = x, y$ , or  $z$ .

The limit  $\Delta t \rightarrow '0'$  means that we let  $\Delta t$  become small compared to any macroscopic time scale, while it still remains large compared with time intervals between collisions. The angular brackets  $\langle \cdot \rangle$  denote the statistical (or ensemble) average.

The components of the tensor of angular diffusion are defined by

$$(\vec{D})_{ij} \equiv \lim_{\Delta t \rightarrow '0'} \frac{1}{2} \frac{\langle \Delta p_i \Delta p_j \rangle}{\Delta t}$$

Both  $\mathbf{F}_D$  and  $\vec{D}$  describe elastic and inelastic collisions such that the change of total momentum is small.

The dynamic friction function for runaway electrons quantifies the average energy loss and is given by  $\mathbf{F}_D = -\hat{\mathbf{p}} F_D(\mathcal{E})$ , where  $F_D(\mathcal{E})$  is found from the Bethe expression (2.2).

The diffusion tensor is easily found for the case  $\mathbf{p} \parallel \hat{\mathbf{z}}$ , in which case we have

$$\begin{aligned} \frac{\langle \Delta p_z^2 \rangle}{\Delta t} &= 0 \\ \frac{\langle \Delta p_x^2 \rangle}{\Delta t} &= \frac{\langle \Delta p_y^2 \rangle}{\Delta t} = \frac{1}{2} \frac{\langle \Delta p_{\perp}^2 \rangle}{\Delta t} = \frac{1}{2} \frac{\langle \Theta^2 \rangle}{\Delta t} p^2 \end{aligned}$$

where  $\Theta$  is the angle by which the particle is deflected from its initial direction. Introducing a derivative  $d\langle \Theta^2 \rangle / dt \equiv \langle \Theta^2 \rangle / \Delta t$  [Jackson, 1975, p. 649], for  $\mathbf{p} \parallel \hat{\mathbf{z}}$  we have

$$\vec{D} = \frac{1}{4} \frac{d\langle \Theta^2 \rangle}{dt} p^2 \begin{pmatrix} 1 & 0 & 0 \\ 0 & 1 & 0 \\ 0 & 0 & 0 \end{pmatrix}$$

After we introduce the diffusion coefficient

$$D(p) = \frac{1}{4} \frac{d\langle \Theta^2 \rangle}{dt}$$

we can write  $\overleftrightarrow{\mathbf{D}}$  in a more compact form which also does not depend on the direction of  $\mathbf{p}$ :

$$\overleftrightarrow{\mathbf{D}} = D(p) \left( p^2 \overleftrightarrow{\mathbf{I}} - \mathbf{p} \mathbf{p}^T \right)$$

where  $\overleftrightarrow{\mathbf{I}}$  is a unit tensor and  $\mathbf{p} \mathbf{p}^T$  is a dyadic product of vector  $\mathbf{p}$  with itself.

For runaway electrons, the angular diffusion is due to elastic scattering from nuclei and  $d\langle \Theta^2 \rangle / dt$  is given in (2.13).

In cylindrical coordinates  $(p, \theta, \phi)$  and in the axially symmetric case ( $\partial / \partial \phi \equiv 0$ ) we have

$$\nabla_{\mathbf{p}} f(\mathbf{p}) = \hat{\mathbf{p}} \frac{\partial f}{\partial p} + \frac{\hat{\boldsymbol{\theta}}}{p} \frac{\partial f}{\partial \theta}$$

Using

$$\overleftrightarrow{\mathbf{D}} \hat{\mathbf{p}} = 0; \quad \overleftrightarrow{\mathbf{D}} \hat{\boldsymbol{\theta}} = D(p) p^2 \hat{\boldsymbol{\theta}}$$

we find

$$\nabla_{\mathbf{p}} [\overleftrightarrow{\mathbf{D}} \nabla_{\mathbf{p}} f(\mathbf{p})] = D(p) \frac{1}{\sin \theta} \frac{\partial}{\partial \theta} \left[ \frac{\partial f}{\partial \theta} \sin \theta \right] = D(p) \frac{\partial}{\partial \mu} \left[ (1 - \mu^2) \frac{\partial f}{\partial \mu} \right]$$

where  $\mu = \cos \theta$ .

# Bibliography

- Atwood, W. B., T. Burnett, R. Cailliau, D. R. Meyers, and K. M. Storr, Gismo: an object-oriented program for high-energy physics event simulation and reconstruction, *Int. J. Modern Phys. C*, *3*, 459, 1992.
- Babich, L. P., A new type of ionization wave and the mechanism of polarization self-acceleration of electrons in gas discharges at high overvoltages, *Sov. Phys. Dokl.*, *27*, 215, 1982.
- Babich, L. P. and I. M. Kutsyk, Numerical simulation of a nanosecond discharge in helium at atmospheric pressure, developing in the regime of runaway of electrons, *High Temperature*, *33*, 190, 1995.
- Babich, L. P., I. M. Kutsyk, E. N. Donskoy, and A. Yu. Kudryavtsev, New data on space and time scales of relativistic runaway electron avalanche for thunderstorm development, *Phys. Lett. A*, *245*, 460, 1998.
- Barrington-Leigh, C. P., U. S. Inan, M. Stanley, and S. A. Cummer, Sprites triggered by negative lightning discharges, *Geophys. Res. Lett.*, *26*, 3605, 1999.
- Bell, T. F., V. P. Pasko, and U. S. Inan, Runaway electrons as a source of red sprites in the mesosphere, *Geophys. Res. Lett.*, *22*, 2127, 1995.

- Berger, M., Monte Carlo Calculation of the Penetration and Diffusion of Fast Charged Particles, *Meth. Comp. Phys.*, 1, 135, 1963.
- Bethe, H. A. and J. Ashkin. Passage of Radiation through Matter. In Segrè, E., editor, *Experimental Nuclear Physics*, volume 1, p. 166. John Wiley, New York, 1953.
- Birdsall, C. K. and A. B. Langdon. *Plasma Physics via Computer Simulation*. Adam Hilger, New York, 1991.
- Brown, R. T., Ionospheric Effects of Cosmic  $\gamma$ -ray Bursts, *Nature*, 246, 83, 1973.
- Bulanov, S. V., M. Lontano, and P. V. Sasorov, Ionization rate in the presence of runaway electrons, *Phys. Plasmas*, 4, 931, 1997.
- Burke, W. J., T. L. Aggson, N. C. Maynard, W. R. Hoegy, R. A. Hoffman, R. M. Candy, C. Liebrecht, and E. Rodgers, Effects of lightning discharge detected by the DE 2 satellite over hurricane Debbie, *J. Geophys. Res.*, 97, 6359, 1992.
- Chamberlain, J. W., *Physics of Aurora and Airglow*. Academic Press, New York, 1961.
- Davies, D. K. Measurements of swarm parameters in dry air. Technical report, Westinghouse R&D center, Pittsburg, 1983. Theoretical notes, Note 346.
- Dejnakarintra, M. and C. G. Park, Lightning-induced electrical fields in the ionosphere, *J. Geophys. Res.*, 79, 1903, 1974.
- Eack, K. B., W. H. Beasley, W. D. Rust, T. C. Marshall, and M. Stoltzenburg, X-ray pulses observed above a mesoscale convective system, *Geophys. Res. Lett.*, 23, 2815, 1996a.

- Eack, K. B., W. H. Beasley, W. D. Rust, T. C. Marshall, and M. Stoltzenburg, Initial results from simultaneous observation of X rays and electric fields in a thunderstorm, *J. Geophys. Res.*, *101*, 29637, 1996b.
- Fano, U., L. V. Spencer, and M. J. Berger. Penetration and diffusion of x-rays. In Flugge, S., editor, *Encyclopedia of Physics*, volume XXXVIII/2, p. 660. Springer-Verlag, New York, 1959.
- Fishman, G. J., P. N. Bhat, R. Malozzi, J. M. Horack, T. Koshut, C. Kouveliotou, G. N. Pendleton, C. A. Meegan, R. B. Wilson, W. S. Paciesas, S. J. Goodman, and H. J. Christian, Discovery of intense gamma-ray flashes of atmospheric origin, *Science*, *264*, 1313, 1994.
- Glukhov, V. S., V. P. Pasko, and U. S. Inan, Relaxation or Transient Lower Ionospheric Disturbances Caused by Lightning-Whistler-Induced Electron Precipitation Bursts, *J. Geophys. Res.*, *97*, 16971, 1992.
- Gurevich, A. V., G. M. Milikh, and R. A. Roussel-Dupré, Runaway mechanism of air breakdown and preconditioning during a thunderstorm, *Phys. Lett. A*, *165*, 463, 1992.
- Gurevich, A. V., G. M. Milikh, and R. A. Roussel-Dupré, Nonuniform runaway air-breakdown, *Phys. Lett. A*, *187*, 197, 1994.
- Gurevich, A. V., J. A. Valdivia, G. M. Milikh, and K. Papadopoulos, Runaway electrons in the atmosphere in the presence of a magnetic field, *Radio Sci.*, *31*, 1541, 1996.
- Gurevich, A. V., G. M. Milikh, and J. A. Valdivia, Model of x-ray emission and fast preconditioning during a thunderstorm, *Phys. Lett. A*, *231*, 402, 1997.

- Gurevich, A. V., K. F. Sergeichev, I. A. Sychov, R. Roussel-Dupré, and K. P. Zybin, First observations of runaway breakdown phenomenon in laboratory experiments, *Phys. Lett. A*, 260, 269, 1999a.
- Gurevich, A. V. and G. M. Milikh, Generation of x-rays due to multiple runaway breakdown inside thunderclouds, *Phys. Lett. A*, 262, 457, 1999b.
- Hale, L. C., Coupling of ELF/ULF energy from lightning and MeV particles to the middle atmosphere, ionosphere, and global circuit, *J. Geophys. Res.*, 99, 21089, 1994.
- Heitler, W., *The Quantum Theory of Radiation*. Clarendon, Oxford, 3 edition, 1954.
- Holzworth, R. H., M. C. Kelley, C. L. Siefring, L. C. Hale, and J. T. Mitchell, Electrical measurements in the atmosphere and the ionosphere over an active thunderstorm. 2. Direct current electric fields and conductivity, *J. Geophys. Res.*, 90, 9824, 1985.
- Hubbell, J. Photon cross-sections, attenuation coefficients from 10 keV to 100 GeV. Technical Report 29, US Dept. of Commerce, 1969. Publ. NSRDS-NBS.
- Inan, U. S., C. Barrington-Leigh, S. Hansen, V. S. Glukhov, T. F. Bell, and R. Rairden, Rapid lateral expansion of optical luminosity in lightning-induced ionospheric flashes referred to as ‘elves’, *Geophys. Res. Lett.*, 24, 583, 1997.
- Inan, U. S., D. L. Carpenter, R. A. Helliwell, and J. P. Katsufakis, Subionospheric VLF/LF phase perturbations produced by lightning-whistler induced particle precipitation, *J. Geophys. Res.*, 90, 7457, 1985.

- Inan, U. S., N. G. Lehtinen, S. J. Lev-Tov, M. P. Johnson, T. F. Bell, and K. Hurley, Ionization of the lower ionosphere by  $\gamma$ -rays from a magnetar: detection of a low-energy (3–10 keV) component, *Geophys. Res. Lett.*, *26*, 3357, 1999.
- Inan, U. S., S. C. Reising, G. J. Fishman, and J. M. Horack, On the association of terrestrial gamma-ray bursts with lightning and implication for sprites, *Geophys. Res. Lett.*, *23*, 1017, 1996b.
- Inan, U. S., W. A. Sampson, and Y. N. Taranenko, Space-time structure of optical flashes and ionization changes produced by lightning-EMP, *Geophys. Res. Lett.*, *23*, 133, 1996a.
- Jackson, J. D., *Classical Electrodynamics*. John Wiley, New York, 2 edition, 1975.
- Jones, V. A. *Aurora*. D. Reidel Publishing Co., Dordrecht, 1974.
- Khazanov, G. V., M. W. Liemohn, E. N. Krivorutsky, J. U. Kozyra, and B. E. Gilchrist, Interhemispheric transport of relativistic electron beams, *Geophys. Res. Lett.*, *26*, 581, 1999.
- Koch, H. W. and J. W. Motz, Bremsstrahlung cross-section formulas and related data, *Rev. Modern Phys.*, *31*, 920, 1959.
- Krall, N. A. and A. W. Trivelpiece, *Principles of Plasma Physics*. San Francisco Press, San Francisco, 1986.
- Kunhardt, E. E., Y. Tzeng, and J. P. Boeuf, Stochastic development of an electron avalanche, *Phys. Rev. A*, *34*, 440, 1986.
- Kurzan, B., K.-H. Steuer, and G. Fussman, Dynamics of runaway electrons in the magnetic field of a tokamak, *Phys. Rev. Lett.*, *75*, 4626, 1995.

- Kutsyk, I. M. and L. P. Babich, Spatial structure of optical emissions in the model of gigantic upward atmospheric discharges with participation of runaway electrons, *Phys. Lett. A*, 253, 75, 1999.
- Kuznetsov, Yu. K., I. El Chamaa Neto, I. C. Nascimento, and R. M. O. Galvão, Runaway discharge in the small Brazilian Tokamak TBR-1, *Phys. Plasmas*, 6, 4002, 1999.
- LaBelle, J., Are fast atmospheric pulsations optical signatures of lightning-induced electron precipitation?, *Geophys. Res. Lett.*, 15, 279, 1988.
- Lehtinen, N. G., M. Walt, U. S. Inan, T. F. Bell, and V. P. Pasko,  $\gamma$ -ray emission produced by a relativistic beam of runaway electrons accelerated by quasi-electrostatic thundercloud fields, *Geophys. Res. Lett.*, 23, 2645, 1996.
- Lehtinen, N. G., T. F. Bell, V. P. Pasko, and U. S. Inan, A two-dimensional model of runaway electron beams driven by quasi-electrostatic thundercloud fields, *Geophys. Res. Lett.*, 24, 2639, 1997.
- Lehtinen, N. G., T. F. Bell, and U. S. Inan, Monte Carlo simulation of runaway MeV electron breakdown with application to red sprites and terrestrial gamma ray flashes, *J. Geophys. Res.*, 104, 24699, 1999.
- Lehtinen, N. G., U. S. Inan, and T. F. Bell, Trapped energetic electron curtains produced by thunderstorm driven relativistic runaway electrons. *Geophys. Res. Lett.*, in press, 2000a.
- Lehtinen, N. G., U. S. Inan, and T. F. Bell, Effects of Thunderstorm Driven Runaway Electrons in the Conjugate Hemisphere: Purple Sprites and Ionization Enhancements. *J. Geophys. Res.*, in preparation, 2000b.



- Lev-Tov, S. J., U. S. Inan, A. J. Smith, and M. A. Clilverd, Characteristics of localized ionospheric disturbances inferred from VLF measurements at two closely spaced receivers, *J. Geophys. Res.*, *101*, 15737, 1996.
- Lin, S. L. and J. N. Bardsley, Monte Carlo simulation of ion motion in drift tubes, *J. Chem. Phys.*, *66*, 435, 1977.
- McCarthy, M. P. and G. K. Parks, Further observations of x-rays inside thunderstorms, *Geophys. Res. Lett.*, *12*, 393, 1985.
- McCarthy, M. P. and G. K. Parks, On the modulation of X ray fluxes in thunderstorms, *J. Geophys. Res.*, *97*, 5857, 1992.
- Mende, S. B., R. L. Rairden, G. R. Swenson, and W. A. Lyons, Sprite spectra; N<sub>2</sub> 1 PG band identification, *Geophys. Res. Lett.*, *22*, 2633, 1995.
- Milikh, G. and J. A. Valdivia, Model of gamma ray flashes due to fractal lightning, *Geophys. Res. Lett.*, *26*, 525, 1999.
- Mott, N. F. and H. S. W. Massey, *The Theory of Atomic Collisions*. Clarendon, Oxford, 3 edition, 1965.
- Nelson, W. R., D. W. O. Rogers, and H. Hirayama, The EGS4 Code System. Technical report, Stanford Linear Accelerator, Stanford, 1985. Report SLAC-265.
- Nemiroff, R. J., J. T. Bonnell, and J. P. Norris, Temporal and spectral characteristics of terrestrial gamma flashes, *J. Geophys. Res.*, *102*, 9659, 1997.
- Nemzek, R. J. and J. R. Winckler, Observation and interpretation of fast sub-visual light pulses from the night sky, *Geophys. Res. Lett.*, *16*, 1015, 1989.

- Ögelman, H., Millisecond time scale atmospheric light pulses associated with solar and magnetospheric activity, *J. Geophys. Res.*, *78*, 3033, 1973.
- Papadopoulos, K., G. Milikh, A. Gurevich, A. Drobot, and R. Shanny, Ionization Rates for Atmospheric and Ionospheric Breakdown, *J. Geophys. Res.*, *98*, 17593, 1993.
- Pasko, V. P. and U. S. Inan, Recovery signatures of lightning-associated VLF perturbations as a measure of the lower ionosphere, *J. Geophys. Res.*, *99*, 17523, 1994.
- Pasko, V. P., U. S. Inan, and T. F. Bell, Blue jets produced by quasi-electrostatic pre-discharge thundercloud fields, *Geophys. Res. Lett.*, *23*, 301, 1996.
- Pasko, V. P., U. S. Inan, T. F. Bell, and Y. N. Taranenko, Sprites produced by quasi-electrostatic heating and ionization in the lower atmosphere, *J. Geophys. Res.*, *102*, 4529, 1997.
- Pasko, V. P., U. S. Inan, and T. F. Bell, Ionospheric effects due to electrostatic thundercloud fields, *J. Atmos. Solar-Terr. Phys.*, *60*, 863, 1998.
- Pasko, V. P., U. S. Inan, and T. F. Bell, Spatial structure of sprites, *Geophys. Res. Lett.*, *25*, 2123, 1998.
- Pilkington, G. R. and C. D. Anger, A Monte Carlo Analysis of the Passage of Auroral X-Rays through the Atmosphere, *Planet. Space Sci.*, *19*, 1069, 1971.
- Press, W. H., S. A. Teukolsky, W. T. Vetterling, and B. P. Flannery, *Numerical Recipes in FORTRAN*. Cambridge Univ. Press, 2 edition, 1992.

- Price, B. T., C. C. Horton, and K. T. Spinney, *Radiation shielding*. Pergamon Press, 1957.
- Rees, M. H., Auroral ionization and excitation by incident energetic electrons, *Planet. Space Sci.*, *11*, 1209, 1963.
- Rees, M. H., *Physics and chemistry of the upper atmosphere*. Cambridge Univ. Press, 2 edition, 1989.
- Risken, H., *The Fokker-Planck Equation*. Springer-Verlag, New York, 2 edition, 1989.
- Rodriguez, J. V. and U. S. Inan, Electron density changes in the nighttime *D* region due to heating by very-low-frequency transmitters, *Geophys. Res. Lett.*, *21*, 93, 1994.
- Roussel-Dupré, R. A., A. V. Gurevich, T. Tunnel, and G. M. Milikh, Kinetic theory of runaway breakdown, *Phys. Rev. E*, *49*, 2257, 1994.
- Roussel-Dupré, R. A. and A. V. Gurevich, On runaway breakdown and upward propagating discharges, *J. Geophys. Res.*, *101*, 2297, 1996.
- Roussel-Dupré, R., E. Symbalisty, Y. Taranenko, and V. Yukhimuk, Simulations of high-altitude discharges initiated by runaway breakdown, *J. Atmos. Sol. Terr. Phys.*, *60*, 917, 1998.
- Seltzer, S. M. and M. J. Berger, Bremsstrahlung in the atmosphere at satellite altitudes, *J. Atmos. Terr. Phys.*, *36*, 1283, 1974.

- Sentman, D. D., E. M. Wescott, D. L. Osborne, D. L. Hampton, and M. J. Heavner, Preliminary results from the Sprites94 campaign: Red sprites, *Geophys. Res. Lett.*, *22*, 1205, 1995.
- Shveigert, V. A., Development of electron avalanche in strong electric fields, *Sov. J. Plasma Phys.*, *14*, 373, 1988.
- Sizykh, S. V., Runaway electron production rate in gaseous discharges, *High Temperature*, *31*, 1, 1993.
- Stix, T. H., *The Theory of Plasma Waves*. McGraw-Hill, New York, 1962.
- Storm, E. and H. I. Israel, Photon Cross Sections From 1 keV to 100 MeV for Elements  $Z = 1$  to  $Z = 100$ , *Nuclear Data Tables*, *A7*, 565, 1970.
- Symbalisty, E., R. Roussel-Dupré, L. P. Babich, I. M. Kutsyk, E. N. Donskoy, and A. Y. Kudryavtsev, Re-evaluation of electron avalanche rates for runaway and upper atmospheric discharge phenomena (abstract), *Eos Trans. AGU, Fall Meet. Suppl.*, *78 (46)*, F70, 1997.
- Symbalisty, E. M. D., R. A. Roussel-Dupré, and V. A. Yukhimuk, Finite volume solution of the relativistic Boltzmann equation for electron avalanche rates, *IEEE Trans. Plasma Sci.*, *26*, 1575, 1998.
- Taranenko, Y. and R. Roussel-Dupré, High altitude discharges and gamma-ray flashes: A manifestation of runaway air breakdown, *Geophys. Res. Lett.*, *23*, 571, 1996.
- Taranenko, Y. and R. Roussel-Dupré, Reply, *Geophys. Res. Lett.*, *24*, 2645, 1997.

- Tarasova, L. V., L. N. Khudyakova, T. V. Loiko, and V. A. Tsukerman, Fast electrons and x rays from nanosecond gas discharges at 0.1–760 torr, *Sov. Phys. Tech. Phys.*, *19*, 351, 1974.
- Tsyтович, V. N., *Lectures on Non-linear Plasma Kinetics*. Springer-Verlag, New York, 1995.
- Tzeng, Y. and E. E. Kunhardt, Effect of energy partition in ionizing collisions on the electron-velocity distribution, *Phys. Rev. A*, *34*, 2148, 1986.
- Vampola, A. L., Comment on ‘Are fast atmospheric pulsations optical signatures of lightning-induced electron precipitation?’ by J. LaBelle, *Geophys. Res. Lett.*, *15*, 633, 1988.
- Volland, H., *Atmospheric Electrodynamics*. Springer-Verlag, New York, 1984.
- Walt, M., *Introduction to Geomagnetically Trapped Radiation*. Cambridge Univ. Press, New York, 1994.
- Wescott, E. M., D. D. Sentman, M. J. Heavner, D. L. Hampton, and O. H. Vaughan Jr, Blue jets: their relationship to lightning and very large hailfall, and their physical mechanisms for their production, *J. Atmos. Solar-Terr. Phys.*, *60*, 713, 1998a.
- Wescott, E. M., D. D. Sentman, M. J. Heavner, D. L. Hampton, W. A. Lyons, and T. Nelson, Observations of ‘columniform’ sprites, *J. Atmos. Solar-Terr. Phys.*, *60*, 733, 1998b.
- Wilson, C. T. R., The electric field of a thundercloud and some of its effects, *Phys. Soc. London Proc.*, *37*, 32D, 1925.

- Winckler, J. R., R. C. Franz, and R. J. Nemzek, Fast low-level light pulses from the night sky observed with the SKYFLASH program, *J. Geophys. Res.*, *98*, 8775, 1993.
- Wolf, T. G. and U. S. Inan, Path-dependent properties of subionospheric VLF amplitude and phase perturbations associated with lightning, *J. Geophys. Res.*, *95*, 20997, 1990.
- Yukhimuk, V., R. Roussel-Dupré, E. M. D. Symbalisty, and Y. Taranenko, Optical characteristics of Red Sprites produced by runaway air breakdown, *J. Geophys. Res.*, *103*, 11473, 1998.
- Yukhimuk, V., R. Roussel-Dupré, and E. M. D. Symbalisty, On the temporal evolution of red sprites: Runaway theory versus data, *Geophys. Res. Lett.*, *26*, 679, 1999.